

# A Novel Probabilistic Method for Life Cycle Management of Fatigue Critical Aircraft Components using In Situ Nondestructive Inspection

Michael Shiao<sup>1</sup>, Tzikang (John) Chen<sup>2</sup>, Y-T. (Justin) Wu<sup>3</sup>, and Anindya Ghoshal<sup>4</sup>

<sup>1</sup>U.S. Army Research Laboratory, RDRL-VTP, Aberdeen Proving Ground, MD 21005

<sup>2</sup>U.S. Army Research Laboratory, RDRL-VTM, Aberdeen Proving Ground, MD 21005

<sup>3</sup>CompRel Inc., 1412 Whittington Dr., Raleigh, NC 27614

<sup>1</sup>chi-yu.shiao.civ@mail.mil; <sup>2</sup>tzikang.chen.civ@mail.mil; <sup>3</sup>justinywu@gmail.com; <sup>4</sup>anindya.ghoshal.civ@mail.mil

Received: July 15, 2015; Sent for review: July 16, 2015; Accepted: September 9, 2015

## Abstract

For the maintenance of fatigue-critical aircraft components, the conventional probabilistic risk assessment (PRA) methodology for life cycle management using nondestructive inspection (NDI) is based on the assumption of independent inspection outcomes. When using an in-situ NDI (INDI) system, however, the independent assumption no longer holds, and the existing PRA methodology must be modified. The major issues to be resolved are how to properly account for correlated inspection outcomes from the same sensors on the same components, and how to quantify their PRA effects. This paper describes a novel probabilistic lifing method for an INDI-based PRA framework with proper modeling of statistical correlations. The framework and the associated probabilistic algorithms are based on the principles of fatigue damage progression, NDI reliability assessment and reliability methods. The core of this method is an accurate and computationally-efficient probabilistic algorithm RPI (Recursive Probability Integration) for PRA. Unlike the existing PRA methods, RPI can incorporate a wide range of uncertainties including material properties, repair quality, crack growth related parameters, loads, inspection reliability and inspection correlations. The RPI algorithm for INDI applications is derived in detail. The effects of correlation strength on risk prediction are also discussed.

## Keywords

RPI; CBM; NDI; in situ NDI; Life cycle management; Damage tolerance; DT, Probabilistic; Risk; Reliability; Inspection dependence; Correlation

## Nomenclature (Acronyms and Symbols)

ARL:	Army Research Laboratory
CBM:	condition-based maintenance
CDF:	cumulative distribution function
CPOF:	cumulative probability of failure
DARWIN:	Design Assessment of Reliability with Inspection
DoD:	Department of Defense
DT:	damage tolerance
INDI:	in situ nondestructive inspection
MCS:	Monte Carlo simulation
NDI:	nondestructive inspection
PND:	probability of missing all inspections
POD:	probability of detection
PRA:	probabilistic risk assessment
PROF:	Probability of Fracture

RPI:	Recursive Probability Integration
SFPOF:	single flight probability of failure
Std:	standard deviation
$a$ :	crack size
$F_m$ :	cumulative distribution function of fatigue life
$f_m$ :	probability density function of fatigue life
$g$ :	limit state function
$K$ :	stress intensity factor
$K_c$ :	fracture toughness
$P$ :	probability
$S_{max}$ :	peak stress in a flight
$t$ :	time
$a$ :	the crack length difference between two inspections
$\rho$ :	correlation between two inspection outcomes

## Introduction

U.S. Army has published a handbook ADS-79D-HDBK [1] to describe the U.S. Army Condition Based Maintenance (CBM) technical guidance necessary to achieve CBM goals for U.S. Army manned and unmanned aircraft systems as Department of Defense (DoD) are undergoing a fundamental shift towards CBM [2] to improve aircraft/rotorcraft availability and readiness at reduced operating cost throughout the system/component life cycle. The CBM approach allows the Army to rapidly repair platforms by seamlessly collecting critical platform information that can be used for risk and remaining useful life assessment. The purpose of CBM is to take maintenance action on system/component where there is evidence of need. By quantifying and managing risk, CBM is expected to be transformed from the traditional labor intensive and cost ineffective scheduled maintenance practice to an integrated, efficient, and semi-autonomous maintenance practice. The inspection and repair burden will be significantly reduced with proper characterizations and assessments of current structural health states and future aircraft usages. Thus, real-time, high-fidelity operational decisions regarding sustainability and maintainability can be obtained.

The CBM practice is enabled through three basic methodologies

- *Prognostics and diagnostics for components*
- *Usage monitoring*
- *Fatigue life management*

To support CBM for fatigue-critical component maintenance, inspection methods either using conventional nondestructive inspection (NDI) or in situ NDI (INDI) systems are being developed at U.S. Army Research Laboratory (ARL). These systems must be validated and verified in which component degradations can be effectively detected, localized and reliably quantified.

To determine the risk of component failure, a probabilistic risk assessment (PRA) and management framework is needed. Many NDI systems installed on-board sensors and used automation processes to minimize human errors [3]. Such settings tend to produce systematically and temporally correlated inspection results because the same sensors are used for a long period of time for the same structures [4, 5, 6]. At the same time, there are many factors which may affect the sensor sensitivity and introduce POD variability (and thus the degree of dependency) over time [7, 8]. For example, on-board sensors may be sensitive to surrounding operating environments such as temperature, moisture, and loads etc. In addition, the location, orientation, and surface condition of a three-dimensional defect, as well as the position of the sensors relative to the defect are among the influential factors which may affect inspection reliability in a semi-systematic/random fashion during many consecutive inspections. As a result, it can be argued that the multiple inspection outcomes of a component under damage evolution from an on-board monitoring system will be somewhere between fully correlated and independent. Without the knowledge on the degree of correlation, one may opt to choose the conservative assumption that the inspection

outcomes are fully correlated [5, 7, 9, 10], provided that the risk assessment result meets the certification requirement. On the other hand, assuming independent inspections may produce a risk result that is non-conservative and unacceptable [8]. Therefore, it is beneficial to obtain inspection correlations by experiments or models and include partial correlations in risk assessment.

PRA using conventional NDI methods has been developed by numerous research organizations for over two decades. PRA analysis software such as PROF (Probability of Fracture) [11-13], original RPI (Recursive Probabilistic Integration) [14-17] and DARWIN (Design Assessment of Reliability with Inspection) [18-20] were all developed based on the assumption of independent inspection outcomes. When using health monitoring systems with in situ sensors, however, it has been noted by several researchers that the independent assumption no longer holds [6, 8], and the existing PRA methodology must be modified. To address the issue, early PRA research assumed fully correlated inspection events [21]. In this paper, we will show how to systematically treat any degrees of inspection correlation in the PRA framework. Although RPI method derived in this paper is mainly for addressing correlated inspection events, it is equally applicable for independent inspection events as assumed in the software PROF or DARWIN. Due to the similarity of RPI and PROF, we will discuss their differences in the following.

For independent inspections, the main difference between RPI and earlier similar approaches is that the RPI framework and the associated computational strategies are intended and are more suitable for general, rather than tailored, damage-tolerance based maintenance optimization problems. For example, unlike the well-used PROF [22] and DARWIN [19] approaches which assumed a small and fixed number of random variable (not more than three, in order to use numerical integration effectively) for well-defined fatigue and fracture problems, RPI has no practical limitation in the number of random variables or the type of damage problems. The flexibility allows RPI to be applied to applications outside of fatigue and fracture mechanics. For example, the damage mechanisms can include corrosion, impact damage, etc. For complicated practical problems, which may involve a wide variety of random variables including initial damage, damage growth parameters, environmental stress risers, geometry, material properties, repair quality, and inspection correlations etc., PROF and DARWIN are not suitable and the traditional Monte Carlo Simulations may be the only viable solution method.

In addition, while PROF allows only deterministic crack growth curve, RPI can treat random crack growth histories. Relative to the traditional MCS approach which simulates the key life cycle processes, including the effect of repair (or replacement) after every inspection, the RPI approach is more efficient because it uses random simulation within a relatively limited scope: Monte Carlo is conducted only to simulate a baseline (i.e., no inspection) and a post-repair random crack growth histories. Relative to PROF, which requires recalculating crack size distribution after an inspection and a repair [23], RPI does not require re-simulating random crack growth. Instead, RPI reuses a single set of simulated post-repair random crack growth curves to generate multiple inputs needed for RPI's unique probabilistic event-tree analysis. While not covered in this paper, it should be noted that more efficient importance sampling approaches could be introduced to replace the random crack growth simulations used in the paper. In addition, RPI is also more efficient than traditional MCS because the probability of detection of a crack size is treated analytically, rather than by random simulation. This feature significantly reduces sampling variability and, as a consequence, reduces the sample size requirement. This paper highlights the treatment of partially correlated inspection events within the RPI framework, while treating independent or fully correlated inspections as two special cases.

A roadmap for managing probabilistic life cycle management has been developed with a near-term focus on treating any degrees of statistical correlation between inspection outcomes. The inspection correlation will be experimentally determined using coupon testing. Future PRA will consider a wide range of uncertainties including material properties, repair quality, crack growth related parameters, loads and POD in the analysis as well as parameter updating using service information. The challenges for this research and development effort include data and model fidelity as well as computational efficiency and accuracy of available probabilistic algorithms for risk assessment. At the conclusion of this research and development, life prognostics methodology for fatigue management and maintenance practice will be developed. Analysis tools for determining risk-based inspection schedule and remaining useful life will be developed. Tools for real-time, high-fidelity operational decisions regarding sustainability and maintainability will also be developed.

This paper summarizes the development of an innovative probabilistic lifing method for fatigue design and life

assessment using RPI. The remainder of the paper is organized as follows. Section 2 describes the probabilistic analysis framework for PRA using NDI. Section 3 discusses the main probabilistic analysis driver RPI. Section 4 provides a verification study using RPI for life assessment. Section 5 presents the results of several case studies designed to understand the effects of inspection correlation on risk predictions. The final section provides conclusion and recommendation for future work.

### A Probabilistic Analysis Framework for Damage Tolerance (DT) and Risk-Based Life Cycle Management

The analysis framework, illustrated in Figure 1, includes a comprehensive procedure and process to support life cycle management for CBM. The framework consists of elements including physics of failure, uncertainty modeling, quantification and update, NDI health monitoring, usage monitoring, probabilistic risk assessment and decision making. In this paper, the focus is on probabilistic risk assessment for life cycle management.

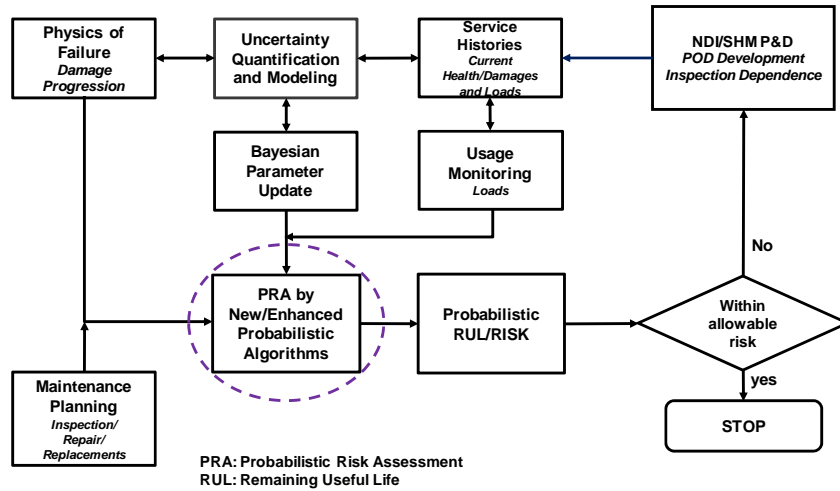


FIG. 1 A PROBABILISTIC ANALYSIS FRAMEWORK FOR DT AND RISK-BASED LIFE CYCLE MANAGEMENT

A schematic of a probabilistic risk assessment is depicted in Figure 2.

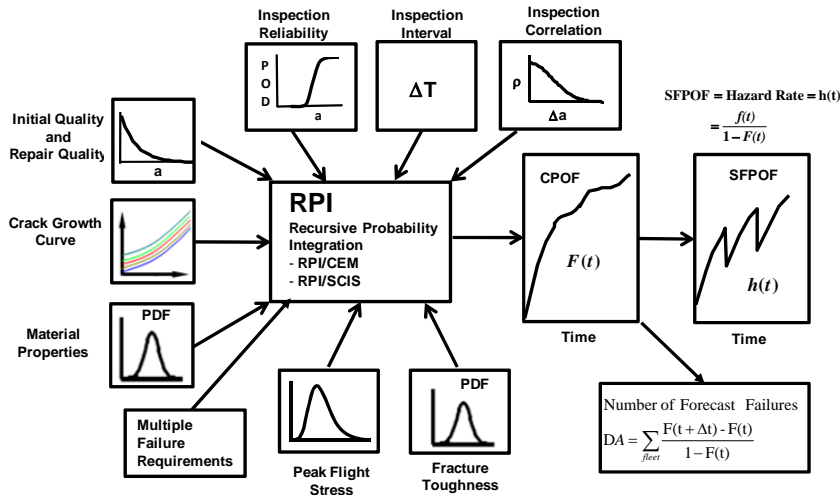


FIG. 2 PROBABILISTIC RISK ASSESSMENT FOR DT AND RISK-BASED LIFE CYCLE MANAGEMENT

As shown in Figure 2, there are a variety of uncertainties which play important roles in risk assessment. They are

- Random or uncertain parameters in material
  - modulus of elasticity
  - fracture toughness
  - yield strength
  - crack growth rate

- Defect or flaw (including size, shape, and location, and the frequency of occurrence)
- Loading, type of usage (with frequency of occurrence)
- Simulation error
- Maintenance related uncertainties
  - inspection schedules, frequency
  - inspection reliability (POD)
  - Inspection correlation
  - Probability of inspection
  - repair/replacement quality
- Impact damage and strength degradation

All the uncertainties are processed through the probabilistic analysis driver “RPI” (Recursive Probability Integration) to provide risk information for maintenance decision-making. Cumulative distribution function (CDF),  $F_m(t)$ , of fatigue life under a set of maintenance plans will be determined first.  $F_m(t)$  can also be defined as the cumulative probability of failure (CPOF) at time  $t$ . Failure criteria for fatigue life analysis can be based on either failure or net section yield. Single flight probability of failure (SFPOF) and defect airplane (DA), two reliability measures related to critical requirements for risk management [22, 24], are shown in the equations below. SFPOF, also called hazard rate, is computed by Equation (1).

$$SFPOF(t) = \frac{f_m(t)}{1 - F_m(t)} \quad (1)$$

Where  $f_m(t)$  is the derivative of  $F_m(t)$ . DA representing the number of forecast failures in a time interval  $[t, t+\Delta t]$  of a fleet is shown in Equation (2).

$$DA = \sum_{fleet} \frac{F_m(t + \Delta t) - F_m(t)}{1 - F_m(t)} \quad (2)$$

### Probabilistic Lifting Method Based on a General-Purpose Recursive Probability Integration (RPI) for DT and Risk-Based Life Cycle Management

Monte Carlo simulation (MCS) offers the most robust and reliable solution framework for general problems. The major issue is that MCS is time-consuming and unable to support timely decisions. For maintenance planning and risk monitoring, the computational issue is further amplified because the conventional approach requires a set of MCS for each different maintenance plan. As a result, numerous sets of MCSs with associated crack growth histories are required to search for the optimal solutions, such as best inspection intervals for minimum allowable risk by exploring the decision parameter space that consists of many possible combinations of inspection scheduling, techniques, and repair/replacement/retirement strategies.

To relieve the computational burden, an efficient method was developed which combined the generality of random simulations with the efficiency of analytical probabilistic methods. The core of the method is a recursive probabilistic integration (RPI) algorithm which allows repeated use of baseline simulation-based crack growth histories for various maintenance plans. The RPI for NDI applications is derived in Appendix A. Throughout the paper,  $n$  represents the number of simulations for random crack growth histories,  $i$  indicates  $i^{\text{th}}$  simulation,  $m$  is the total number of inspections conducted before time  $t$  for life assessment in a simulation, and  $N$  indicates  $N^{\text{th}}$  inspection.

In traditional Monte Carlo simulations, random fatigue crack growth paths (or histories) are generated as a result of random crack growth behavior, random damage detections, random manufacturing, and random repair quality. A significant number of simulations are usually required for a desired accuracy. RPI systematically transforms the random pattern to a more logical and manageable probabilistic event tree for any MCS realizations. Using the event tree [25], state-of-the-art efficient reliability methods, including classical MPP-based and importance sampling methods [18], can be applied which results in a significant improvement on computational efficiency.

As shown in Appendix A, a probabilistic event tree is used to derive the probabilistic algorithm RPI for the determination of cumulative probability of failure (CPOF) at time  $t$ .  $CPOF(t)$ , which is equal to  $F_m(t)$  in Equation (1), is then derived as:

$$CPOF(t) = \frac{1}{n} \sum_{i=1}^n \sum_{N=0}^m \left[ \begin{aligned} & (1 - P_f^{cum,i}(N)) * \left( P\left(\bigcap_{k=0}^{N-1} M_k^i\right) - P\left(\bigcap_{k=0}^N M_k^i\right) \right) * P_f(R_p^N) \\ & + P\left(\bigcap_{k=0}^N M_k^i\right) * P_f^{int,i}(N, N+1) \end{aligned} \right] \quad (3)$$

where the subscript  $i$  refers to the  $i^{\text{th}}$  MCS simulation,  $n$  is the total number of simulations and  $m$  is the number of inspections conducted before time  $t$  for life assessment. All other terms in Equation (3) are defined in appendix A. Single flight probability of failure (SFPOF) at any given time in the interval  $[0, t]$  is then determined using Equation (1).

In the original RPI algorithm [14-17], the recursive scheme is based on backward substitution. By using the backward recursive scheme, the inspection for all of the paths (original and repaired) must be conducted at the same time. This restriction limits the applicability of RPI for better fatigue life management. To overcome this limitation, an enhanced RPI algorithm with a forward recursive scheme to determine the cumulative probability of failure and single flight probability of failure was developed [26]. This new numerical scheme improves the computational efficiency of original RPI and also eliminates the original RPI's restriction by allowing variable inspection intervals for non-repaired and repaired components. The inspection intervals can be determined by different maintenance strategies and regulatory requirements for both non-repaired and repaired components. The forward recursive scheme is illustrated in Appendix B.

Relative to the authors' earlier work [14-17], Equation (3) is the first generalized RPI algorithm which can account for the effect of inspection correlations. In order to solve Equation (3), interval probability of failure  $P_f^{int,i}(N, N+1)$  is determined in Appendix A, cumulative probability of failure of all repair paths  $P_f(R_p^N)$  is discussed in Appendix B, probability of no detections of all  $N$  inspections  $P\left(\bigcap_{j=0}^N M_j^i\right)$  is derived in Appendix C.

### Verification of Recursive Probability Integration (RPI)

A metallic plate with a crack at the edge of a center hole subjected to cyclic fatigue loading was selected to verify the risk assessment of an aircraft component using RPI. The failure is defined by a limit state function  $g$  based on a fracture mechanics criterion:

$$g = K_c - K < 0 \quad (4)$$

where

$$K = S_{max} * H(a) \quad (5)$$

where  $K_c$  is material fractural toughness,  $K$  is the stress intensity factor,  $S_{max}$  is the peak stress in a flight and  $a$  is the crack size. The function  $H(a)$  is defined in Figure 3.

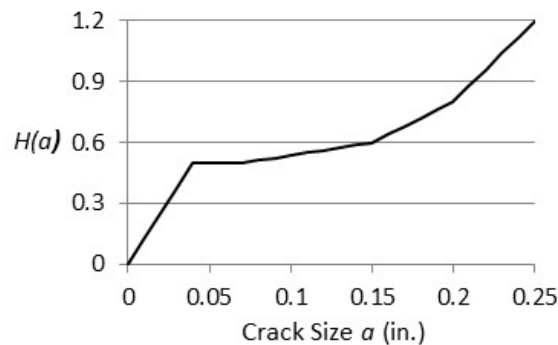


FIG. 3  $K/S_{max}$  VERSUS CRACK SIZE

All of the random variables and their relationships are summarize in the Table 1.

TABLE 1. SUMMARY OF INPUT VARIABLES

Quantity	Distribution	Param. 1	Param. 2
Initial crack size	Truncated Weibull (Truncate $a > 0.13$ )	Scale = 0.02	Shape = 1
Fracture toughness	Normal	Mean = 24.5	Std = 3.1
Peek stress	$f(S_{max}) = \frac{1}{A} e^{-\frac{P_{max}-B}{A}} e^{-e^{-\frac{P_{max}-B}{A}}}$	A = 14.6	B = 1.31
Prob. of detection	$POD(a) = \left\{ 1 + e^{\frac{-1.8[\ln(a) - \ln(a_{50})]}{\sigma}} \right\}^{-1}$	$a_{50} = 0.06$	$\sigma = 0.5$
Crack propagation	$a = \exp(b \cdot (c - t))$	$b = -0.0001$	$c = 80000$

The total flight life of the example is 30,000 cycles and inspection schedule is [4000, 7000, 11000, 15000, 18000, 21000, 24000, 27000]. MCS with 1.6 billion samples was performed. The CPOF and SFPOF by RPI and MCS are shown in Figures 4 and 5, respectively. In both figures, the RPI and MCS curves match closely. The CPU time for the 1.6 billion MCS is about 43 CPU hours on DOD HPC system compared with 220 second on a desktop computer for 1 million simulations for RPI analysis. The ratio of the CPU time for MCS to that of RPI is 700:1.

It is important to select the inspection intervals based on the desired risk level. Since the event trees become too complicated to be analyzed as the number of inspections becomes large, it is impossible to determine the inspection schedule by educated guess. A numerical algorithm needs to be developed in the future to determine the optimal inspection schedule based on SFPOF and a desired risk level.

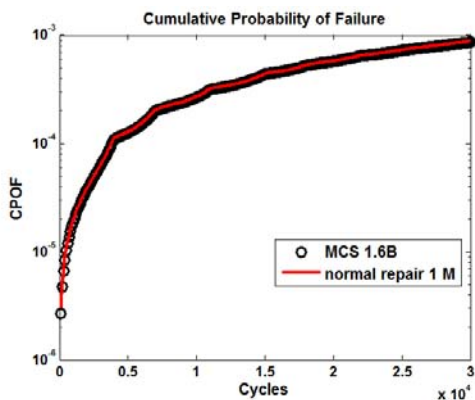


FIG. 4 CPOF OF RPI AND MCS

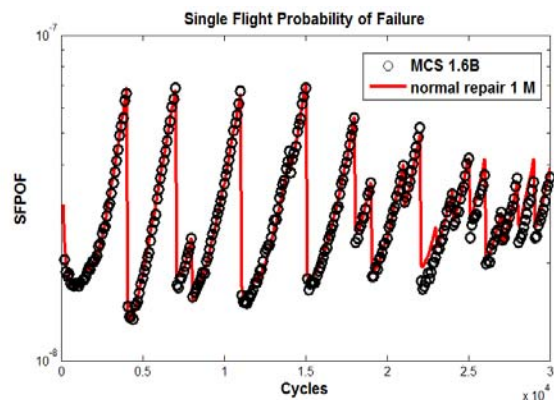


FIG. 5 SFPOF OF RPI AND MCS

### Effect of Correlations among Inspection Events on Risk Predictions

The purpose of this numerical study is to investigate the effect of inspection correlation on the risk prediction for an INDI monitoring system. All of the random variables and their relationships are summarize in the Table 2. In this section, the results of a case study with various correlation assumptions and two inspection intervals will be presented. For a risk analysis using INDI, both POD and inspection correlations defined in a correlation matrix are required.

TABLE 2 SUMMARY OF INPUT VARIABLES

Quantity	Distribution	Param. 1	Param. 2
Initial crack size	Weibull	Scale = 0.02	Shape = 1
Fracture toughness	Normal	Mean = 35.5	Std = 3.1
Peek stress	$f(S_{max}) = \frac{1}{A} e^{-\frac{P_{max}-B}{A}} e^{-e^{-\frac{P_{max}-B}{A}}}$	A = 14.6	B = 1.31
Prob. of detection	$POD(a) = \left\{ 1 + e^{\frac{-1.8[\ln(a) - \ln(a_{50})]}{\sigma}} \right\}^{-1}$	$a_{50} = 0.08$	$\sigma = 0.5$
Crack propagation	$a = \exp(b \cdot (c - t))$	$b = -0.0001$	$c = 80000$

A flexible 2-paramter correlation function was chosen for the investigation.

$$\rho = \exp(-\Delta a^q / \Delta L) \tag{6}$$

In Equation (6),  $\Delta a$  is the crack length difference between two inspections and  $q$  and  $\Delta L$  are variables used to vary the correlation strength. A larger  $q$  or  $\Delta L$  value will result in a larger correlation. Examples of correlations are shown in Figure 6.

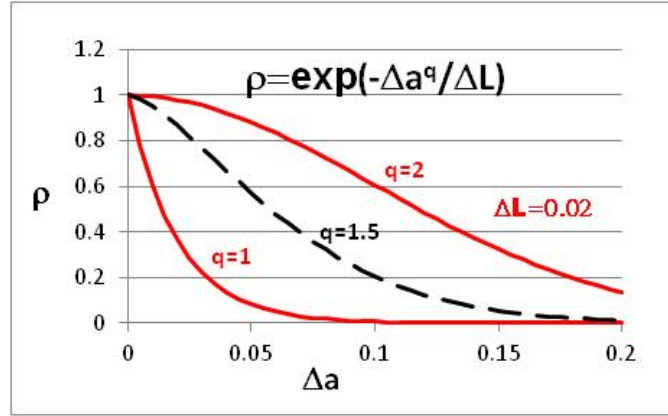


FIG. 6 ASSUMED CORRELATION AMONG INSPECTIONS

In this study, risk predictions using  $q=1, 1.5$  and  $2$  with  $\Delta L = 0.02$  are compared. A weak correlation is represented by  $q=1$ , a medium correlation is represented by  $q=1.5$ , and a strong correlation is represented by  $q=2$ . Correlation strength category is shown in Table 3.

TABLE 3. CORRELATION STRENGTH CATEGORY

$q$	1	1.5	2
Correlation Strength	Weak	Medium	Strong

Based on Equation 6, a correlation matrix was generated and used to construct a non-detection probabilistic event  $M_j^i$  at the  $j^{th}$  inspection for the  $i^{th}$  simulation. Monte Carlo simulations were performed to determine  $P\{\bigcap_{j=0}^N M_j^i\}$  in Equation 3.

Three simulated INDI systems with an identical POD function but different inspection correlation strengths were studied. The cumulative probability of failure (CPOF) and single flight probability of failure (SFPOF) are plotted in Figures 7 to 9 where CPOFs are on the left and SFPOFs are on the right. The inspection interval was fixed at 6000 flights with the inspection correlation strengths varied from weak (Figure 7), to medium (Figure 8), and to strong (Figure 9). The CPOF and SFPOF for all the cases are shown in Table 4. Table 4 shows that the degree of inspection correlation significantly affects the level of risk. The higher the correlation strength is, the larger the predicted risk will be. In this study, only five inspections are considered throughout the life of the component. Should the number of inspections increase to ten, the risk predicted by using independent inspections will be significantly smaller than that by using fully correlated inspections.

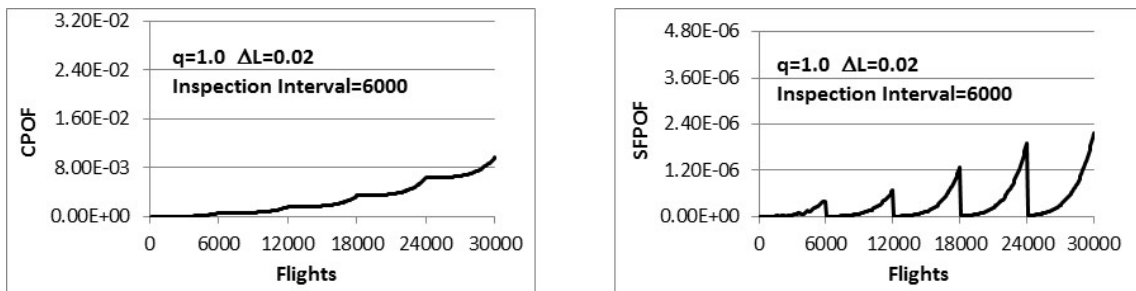


FIG. 7 CUMULATIVE PROBABILITY OF FAILURE (CPOF) AND SINGLE FLIGHT PROBABILITY OF FAILURE (SFPOF) (WEAK INSPECTION CORRELATION)

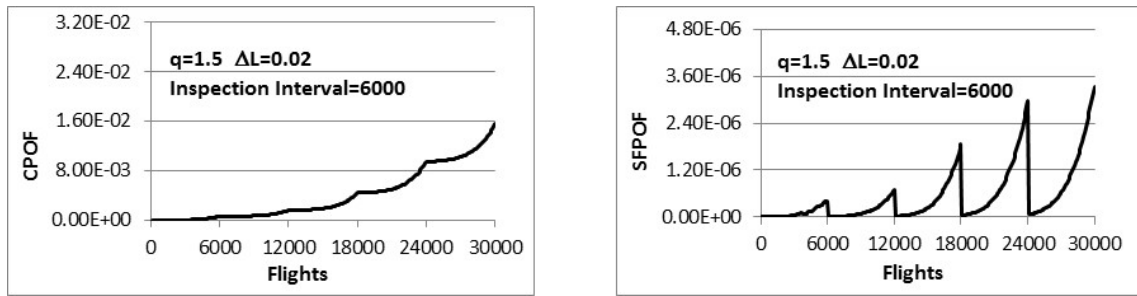


FIG. 8 CUMULATIVE PROBABILITY OF FAILURE (CPOF) AND SINGLE FLIGHT PROBABILITY OF FAILURE (SFPOF) (MEDIUM INSPECTION CORRELATION)

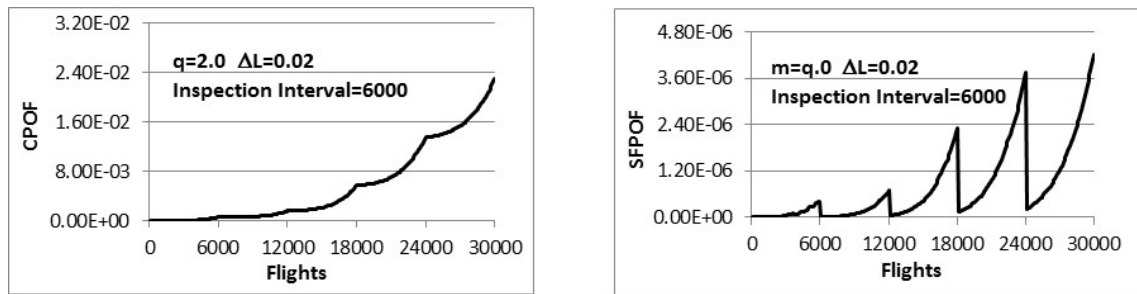


FIG. 9 CUMULATIVE PROBABILITY OF FAILURE (CPOF) AND SINGLE FLIGHT PROBABILITY OF FAILURE (SFPOF) (STRONG INSPECTION CORRELATION)

TABLE 4. CPOF AND SFPOF AT 30000 FLIGHTS

Inspection Correlation Strength	Weak	Medium	Strong
CPOF	9.77E-03	1.55E-02	2.30E-02
SFPOF	2.16E-06	3.35E-06	4.23E-06

### Conclusion and Recommendation

A novel probabilistic lifing method for CBM is developed to properly model any degree of inspection correlation when employing in-situ NDI (INDI) systems. Previous methods which assumed either zero or full correlation could lead to non-conservative or overly conservative risk assessment results. The method features an efficient probabilistic algorithm RPI (Recursive Probabilistic Integration) derived based on an event-tree concept and well known structural reliability method (FORM). The efficiency has been demonstrated using several case studies.

Case studies to investigate the effects of correlation strengths on the probability of missing all inspections (PND) as well as risk predictions have been conducted. The studies have confirmed that the assumption of independent inspection events gives a non-conservative risk prediction while the prediction with the assumption of fully correlated inspection events is conservative. It is also observed from the study that inspection correlation may significantly change the PND and risk predictions even with the identical POD function and the same number of inspections. While the PND with full correlation can provide a conservative bound, it may be overly conservative especially for cases with frequent inspections. The study also showed that the undesirable effect of correlation in the INDI system can be compensated by more frequent inspections. Therefore, for any future INDI systems, a systematic risk and cost based trade-off study of the correlation versus the frequency of the INDI inspections should be beneficial.

The RPI-based probabilistic lifing method has been verified by traditional Monte Carlo simulations. It is also found that this new method is several orders of magnitude more efficient than the traditional Monte Carlo. Future work will include developing advanced numerical strategies to further improve the computational efficiency for PND calculation, performing research to apply importance sampling techniques to further accelerate sampling effectiveness, and conducting experiments to quantify the correlation among inspection events. These improvements will be fed into the health-monitoring based CBM framework to conduct risk-based maintenance optimization.

## REFERENCES

- [1] US Army Research, Development, and Engineering Command, (2013), "Aeronautical Design Standard Handbook for Condition Based Maintenance Systems for US Army Aircraft Systems," ADS-79D-HDBK, US Army Aviation and Missile Command, Aviation Engineering Directorate, Redstone Arsenal, Alabama.
- [2] Zhao, J., Ghoshal, A., (2009), "Structural Reliability and Load Sensing for Condition Based Maintenance Technology," Project Final Report, 2008-B-41-01.1.P3, Center for Rotorcraft Innovation (CRI), Inc.
- [3] "Guidelines for Implementation of Structural Health Monitoring on Fixed Wing Aircraft," SAE Publications, ARP6461, September 2013
- [4] Kabban, C.M.S. and Derriso, M.M., (2011), "Certification in Structural Health Monitoring Systems, "8<sup>th</sup> International Workshop on Structural Health Monitoring, Stanford, University, CA.
- [5] Simonen, F.A.,(1995) "Nondestructive Examination Reliability," Chapter 11, Probabilistic Structural Mechanics Handbook: Theory and Industrial Applications by C.R. Sundararajan, Springer; 1995 Edition.
- [6] Kabban, C., Greenwell, B., DeSimio, M., and Derriso, M., (2015) "The probability of detection for structural health monitoring systems: Repeated measures data", Structural Health Monitoring 1–13, sagepub.co.uk/journalsPermissions.nav, DOI:10.1177/1475921714566530
- [7] Shook, B., Millwater, H., Hudak S., Enright, M.P., and Francis, W.L., (2008), "Simulation of Recurring Automated Inspections on Probability-of-Fracture Estimates," Structural Health Monitoring 2008; 7; 293-307
- [8] Harding, C., and Hugo, G., (2010), "Practical Reliability Validation for Nondestructive Inspections and Structural Health Monitoring Technologies," The Australian Aircraft Airworthiness and Sustainment Conference, Brisbane, Australia.
- [9] Shook, B., Millwater, H., Hudak S., Enright, M.P., and Francis, W.L., (2005), "Impact of Multiple On-Board Inspections on Cumulative Probability of Detection," IGTI Conference, Reno, NV.
- [10] Shook, B., Millwater, H., Hudak S., Enright, M.P., and Francis, W.L., (2005), "Comparison of Continual On-Board Inspections to a Single Mid-Life Inspection for Gas Turbine Engine Disks," 46th AIAA Structures, Dynamics and Materials Conference, Austin, TX.
- [11] Berens, A.P., Hovey, P.W., and Skinn, D.A., (1991), "Risk Analysis for Aging Aircraft Fleets," U.S. Air Force Wright Laboratory Report, WL-TR-91-3066, Vol. 1.
- [12] Lincoln, J.W., (2001) "Risk Assessment of Aging Aircraft," Defense Technical Information Center, Compilation Part Notice, ADP010768.
- [13] Peter, P.W., Berens, A.P. and Loomis, J.S., (1998) "Update of the Probability of Fracture (PROF) Computer Program for Aging Aircraft Risk Analysis, Volume 1 Modifications and User's Guide," U.S. Air Force Wright Laboratory Report, AFRL-VA-WR-TR-1999-3030
- [14] Shiao, M., Le, D., Cuevas, E., (2003), "Feasibility Study of a Reliability-based Damage Tolerance Analysis Method for Rotorcraft Structures and Dynamic Components," The Seventh Joint DOD/FAA/NASA Conference on Aging Aircraft, New Orleans, Louisiana.
- [15] Shiao, M., Boyd, K., and Fawaz, S.,(2005), "A Risk Assessment Methodology and Tool for Probabilistic Damage Tolerance-Based Maintenance Planning," 8<sup>th</sup> FAA/NASA/DoD Aging Aircraft Conference.
- [16] Shiao, M., (2005), "Risk-Based Maintenance Optimization," 9<sup>th</sup> International Conference on Structural Safety and Reliability, Rome, Italy.
- [17] Shiao, M., (2005), "Risk Forecasting and Updating for Damage Accumulation Processes with Inspections and Maintenance", 5<sup>TH</sup> International Workshop on Structural Health Monitoring, Stanford, California.
- [18] Millwater, H.R., Wu, Y.-T., J.W. Cardinal, Chell, G.G. (1996), "Application of Advanced Probabilistic Fracture Mechanics to Life Evaluation of Turbine Rotor Blade Attachments," Journal of Engineering for Gas Turbines and Power, Vol. 118, pp. 394-398.

[19] Leverant, G.R., Littlefield, D.L., McClung, R.C., Millwater, H.R., Wu, Y.-T. (1997). "A Probabilistic Approach to Aircraft Turbine Rotor Material Design," The International Gas Turbine & Aeroengine Congress & Exhibition, Paper No. 97-GT-22, Orlando, FL.

[20] Wu, Y.-T., Enright, M.P., & Millwater, H.R., (2002), "Probabilistic Methods for Design Assessment of Reliability with Inspection (DARWIN)," AIAA Journal, Vol. 40, No. 5, pp. 937-946.

[21] Shiao, M., (2009), "Risk Monitoring of Aircraft Fatigue Damage Evolution at Critical Locations Utilizing Structural Health Monitoring," Encyclopedia of Structural Health Monitoring, John Wiley & Sons, DOI: 10.1002/9780470061626.

[22] Gallagher, J.P., C.A. Babish, and J.C. Malas, (2005), "Damage tolerant risk analysis techniques for evaluating the structural integrity of aircraft structures," Proceedings of the Structural Integrity in Transportation Systems Symposium, 11th International Conference on Fracture, March, Turin, Italy.

[23] Hovey, P.W., Berens, A.P., and Knopp, J., (2006) "Estimating the Distribution of the Size of Flaws Remaining after an Inspection," AFRL-ML-WP-TP-2006-496.

[24] Abernethy, R.B., (2006) "The New Weibull Handbook Fifth Edition, Reliability and Statistical Analysis for Predicting Life, Safety, Supportability, Risk, Cost and Warranty Claims," Published and distributed by Robert B. Abernethy, 2006.

[25] Ericson, C.A., (2005) "Hazard Analysis Techniques for System Safety," 2005 John Wiley & Sons, Inc.

[26] Chen, T., Shiao, M., (2015) "Enhanced Recursive Probabilistic Integration Method for Probabilistic Fatigue Life Management Using Structural Health Monitoring", International Workshop on Structural Health Monitoring, September 1-3, 2015, Stanford, CA

[27] Feller, W., (1973) "An Introduction to Probability Theory and It's Applications," Volume I, Third Edition, John Wiley & Sons, Inc. 1973

[28] Shiao, M. and Shyprykevich, P., (2004), "Hybrid Probabilistic Method for Composite Aircraft Design," 45<sup>th</sup> Structures, Structural Dynamics and Materials Conference.

[29] Wu, Y-T, Shiao, M., and Seneviratne, W., (2011), "Strength-Conditioned Importance Sampling Method for Aircraft Structural Reliability Analysis," 52th AIAA Structures, Dynamics and Materials Conference, Denver, CO.

[30] Parker, A.P., (1981), "The Mechanics of Fracture and Fatigue," E. & F.N. Spon Ltd

[31] Department of Defense, (2009), "Nondestructive Evaluation System Reliability Assessment," MIL-HDBK-1823A.

[32] Haldar, A., Mahadevan, S., (2005) "Probability, Reliability and Statistical Methods in Engineering Design," John Wiley & Sons, Inc.

[33] Madsen, H.O., Krenk, S., and Lind, N.C., (1986), "Methods of Structural Safety," Prentice-Hall, Inc.

APPENDIX A – DERIVATION OF RPI PROBABILISTIC ALGORITHM

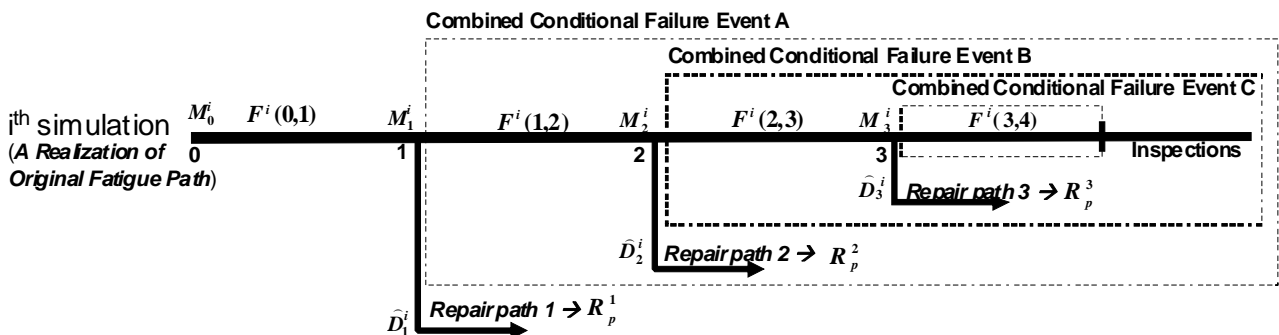


FIG. A1 ORIGINAL PROBABILISTIC EVENT TREE BASED ON THE I<sup>TH</sup> MCS SIMULATION

To determine the cumulative probability of failure at time t as well as single-flight probability of failure at any given time in the interval [0, t], a probabilistic event tree is developed to derive the probabilistic algorithm. Figure A1 depicts the probabilistic event tree using three inspections. The event tree consists of failure events  $F^i(N, N + 1)$  along a crack growth history from the  $i^{th}$  MCS simulation of the original component with manufacturing quality, and failure events  $R_p^N$  including all possible failures

after damage is detected at  $N^{\text{th}}$  inspection and a repair or replacement of the original component is performed after. Crack growth histories are random generated without detections and repairs. The crack growth histories for  $R_p^N$  is generated using a set of realizations associated with the quality of repaired or replacement components. Figure A1 also shows the individual probabilistic events  $M_N^i$ , and  $\widehat{D}_N^i$  which are inspection related probabilistic events.

To illustrate and derive the RPI algorithm, Section A1 will explain all the individual probabilistic events identified in Figure A1, Section A2 will determine the combined overall failure event and Section A3 will determine the probability of failure as described next.

### A.1 Individual Probabilistic Events

The individual probabilistic events identified in Figure A1 are defined below for  $N$  from 0 to 3 where  $N$  is the inspection number. Failure in this paper is defined as a probabilistic event where the peak flight stress is greater than the residual strength of the component. Peak flight stress is the largest peak stress to be encountered in a flight [11] which is modeled as independent random process for a failure analysis.

- $F^i(N, N+1)$  is a failure event along the original fatigue path ( $i^{\text{th}}$  simulation) occurred between  $N^{\text{th}}$  and  $(N+1)^{\text{th}}$  inspections. Treating each simulation as a component of an individual aircraft, the initial flaw size, fracture toughness and other time independent random variables are presented by a set of realizations from random simulations. The only remaining randomness in this simulation is the peak flight stress which is modeled as an independent random process. With such a setup, the interval failure events  $F^i(N, N+1)$  for respective intervals become independent
- $R_p^N$  represents all possible failure events and sequences before the time for life assessment for original component repaired at  $N^{\text{th}}$  inspection or a replacement component to replace the damage original component on the  $i^{\text{th}}$  MCS simulation.  $R_p^N$  can also be defined as a failure event for any component which starts the service at the  $N^{\text{th}}$  inspection. By the second definition, the probability of occurrence of event  $R_p^0$  is the overall probability of failure.
- $D_N^i$  represents a detection event for the crack size  $a_N$  at the  $N^{\text{th}}$  inspection and  $P(D_N^i) = \text{POD}(a_N)$
- $M_N^i$  represents a miss detection event for a given crack size  $a_N$  at the  $N^{\text{th}}$  inspection and  $P(M_N^i) + P(D_N^i) = 1$
- $\widehat{D}_N^i$  is a subset of event  $D_N^i$  where

$$P(\widehat{D}_N^i) = c_N^i * P(D_N^i) \quad (\text{A1})$$

and

$$c_N^i = 1 - \text{cumulative probability of failure at } N^{\text{th}} \text{ inspection} \quad (\text{A2})$$

The explanation follows.  $D_N^i$  is a probabilistic event at  $N^{\text{th}}$  inspection time for  $i^{\text{th}}$  simulation at which the probability of the population to be inspected is equal to 1 conditioned on no failure prior to the  $N^{\text{th}}$  inspection. However, failures may occur before the  $N^{\text{th}}$  inspection for  $i^{\text{th}}$  simulation. Since those failed before  $N^{\text{th}}$  inspection were already out of the service, the probability of the population to be inspected at the  $N^{\text{th}}$  inspection should be reduced from 1 to  $c_N^i$  as shown in Equation (A2). In other words, both detection events use the same inspection technology, but  $\widehat{D}_N^i$  is a subset of  $D_N^i$  with the probability of detection defined by Equation (A1).

Given the above individual probabilistic events, the overall failure event for each of the  $i^{\text{th}}$  probabilistic event tree can be defined in the following section.

### A.2 Combination of Individual Probabilistic Events in a Realization

In Figure A1, the combined event A is an event conditioned on no damage detection and no failure occurrence at and before Inspection 1 in the event tree. The combined event B is an event conditioned on no detections and no failures at and before Inspection 2. Similarly, the combined event C is an event conditioned on no detections and no failures at and before Inspection 3. Also, repair event  $R_p^N$  will occur only when there has no damage detections at and before the  $(N-1)^{\text{th}}$  inspections and a detection at the  $N^{\text{th}}$  inspection.

Using the set theory [27], the failure events A, B and C in Figure A1 can be defined as:

$$A = F^i(1,2) + \widehat{D}_2^i \cap R_p^2 + M_2^i \cap B \quad (\text{A3})$$

$$B = F^i(2,3) + \widehat{D}_3^i \cap R_p^3 + M_3^i \cap C \quad (A4)$$

$$C = F^i(3,4) \quad (A5)$$

The overall failure event  $E^i$  of the  $i^{\text{th}}$  probabilistic event tree can be presented by:

$$E^i = M_0^i \cap \{F^i(0,1) + \widehat{D}_1^i \cap R_p^1 + M_1^i \cap A\} \quad (A6)$$

Substituting  $B$  in Equation (A3) by  $B$  in Equation (A4), we obtain

$$A = F^i(1,2) + \widehat{D}_2^i \cap R_p^2 + M_2^i \cap F^i(2,3) + M_2^i \cap \widehat{D}_3^i \cap R_p^3 + M_2^i \cap [M_3^i \cap C] \quad (A7)$$

Substituting  $C$  in Equation (A7) by  $C$  in Equation (A5), we obtain

$$A = F^i(1,2) + \widehat{D}_2^i \cap R_p^2 + M_2^i \cap F^i(2,3) + M_2^i \cap \widehat{D}_3^i \cap R_p^3 + M_2^i \cap M_3^i \cap F^i(3,4) \quad (A8)$$

Substituting  $A$  in Equation (A6) by  $A$  in Equation (A8), we obtain

$$\begin{aligned} E^i &= M_0^i \cap \widehat{D}_1^i \cap R_p^1 + \bigcup_{N=2}^3 \left\{ \left( \bigcap_{k=0}^{N-1} M_k^i \right) \cap \widehat{D}_N^i \cap R_p^N + M_0^i \cap F^i(0,1) + \bigcup_{N=1}^3 \left( \bigcap_{k=0}^N M_k^i \right) \cap F^i(N, N+1) \right\} \\ &= \bigcup_{N=1}^3 \left[ \left( \bigcap_{k=0}^{N-1} M_k^i \right) \cap \widehat{D}_N^i \cap R_p^N \right] + \bigcup_{N=0}^3 \left[ \left( \bigcap_{k=0}^N M_k^i \right) \cap F^i(N, N+1) \right] \\ &= \bigcup_{N=0}^3 \left[ \left( \bigcap_{k=0}^{N-1} M_k^i \right) \cap \widehat{D}_N^i \cap R_p^N \right] + \bigcup_{N=0}^3 \left[ \left( \bigcap_{k=0}^N M_k^i \right) \cap F^i(N, N+1) \right] \\ &= \bigcup_{N=0}^3 \left\{ \left( \bigcap_{k=0}^{N-1} M_k^i \right) \cap \widehat{D}_N^i \cap R_p^N + \left( \bigcap_{k=0}^N M_k^i \right) \cap F^i(N, N+1) \right\} \end{aligned} \quad (A9)$$

By mathematical induction, the following general form of the combined failure event  $E^i$  for  $m$  inspections can be obtained.

$$E^i = \bigcup_{N=0}^m \left\{ \left( \bigcap_{k=0}^{N-1} M_k^i \right) \cap \widehat{D}_N^i \cap R_p^N + \left( \bigcap_{k=0}^N M_k^i \right) \cap F^i(N, N+1) \right\} \quad (A10)$$

The next step is to determine the probability of failure of event  $E^i$  and the overall probability of failure as discussed in the following section.

### A.3 Cumulative Probability of Failure

Based on the nature of the respective probabilistic events, the following statements can be made.

- Events  $M_k^i$  and  $D_k^i$  are mutually exclusive
- Events  $M_k^i$  for  $k > 0$  can be independent, fully correlated or partially correlated
- Events  $M_0^i$  is independent to all other probabilistic events and  $P(M_0^i) = 1.0$
- Events  $\left\{ \bigcap_{k=0}^{N-1} M_k^i \cap \widehat{D}_N^i \right\}$  and  $R_p^N$  are independent,
- Events  $\left\{ \bigcap_{k=0}^N M_k^i \right\}$  and  $F^i(N, N+1)$  are independent,
- Events  $F^i(N, N+1)$  for all  $N$  are mutually exclusive and
- Events  $F^i(N, N+1)$  and  $R_p^j$  are mutually exclusive

As a result, the following equation can be derived.

$$P_f(E^i) = \sum_{N=0}^m \left[ c_N^i * P \left\{ \left( \bigcap_{k=0}^{N-1} M_k^i \right) \cap \widehat{D}_N^i \right\} * P_f(R_p^N) + P \left\{ \bigcap_{k=0}^N M_k^i \right\} * P_f^{\text{int},i}(N, N+1) \right] \quad (A11)$$

where

$$P_f(F^i(N, N+1)) = P_f^{\text{int},i}(N, N+1) \quad (A12)$$

Define  $P_f^{\text{cum},i}(N)$  as the cumulative probability of failure at the  $N^{\text{th}}$  inspection:

$$P_f^{cum,i}(N) = P_f^{int,i}(0,1) + \sum_{k=2}^N \left[ P\left\{ \bigcap_{j=1}^{k-1} M_j \right\} * P_f^{int,i}(k-1,k) \right] \quad (A13)$$

Substituting Equation (A13) to Equation (A2),  $c_N^i$  can be determined. Also, as proved in Section A.5

$$P\left(\left[\bigcap_{k=1}^{N-1} M_k^i\right] \cap [D_N^i]\right) = P\left(\bigcap_{k=1}^{N-1} M_k^i\right) - P\left(\bigcap_{k=1}^N M_k^i\right) \quad (A14)$$

Substituting Equation (A14) to equation (A11), Equation (A15) is obtained.

$$P_f(E^i) = \sum_{N=0}^m \left[ \begin{aligned} & (1 - P_f^{int,i}(N)) * \left( P\left\{ \bigcap_{k=0}^{N-1} M_k^i \right\} - P\left\{ \bigcap_{k=0}^N M_k^i \right\} \right) * P_f(R_p^N) \\ & + P\left\{ \bigcap_{k=0}^N M_k^i \right\} * P_f^{int,i}(N, N+1) \end{aligned} \right] \quad (A15)$$

The cumulative probability of failure at any time  $t$   $CPOF(t)$ , which is equal to  $F_m(t)$  in Equation (1), can be estimated using the average of the probability of failure of  $E^i$ . The generalized RPI algorithm is then derived as:

$$\begin{aligned} CPOF(t) &= \frac{1}{n} \sum_{i=1}^n P_f(E^i) \\ &= \frac{1}{n} \sum_{i=1}^n \sum_{N=0}^m \left[ \begin{aligned} & (1 - P_f^{cum,i}(N)) * \left( P\left\{ \bigcap_{k=0}^{N-1} M_k^i \right\} - P\left\{ \bigcap_{k=0}^N M_k^i \right\} \right) * P_f(R_p^N) \\ & + P\left\{ \bigcap_{k=0}^N M_k^i \right\} * P_f^{int,i}(N, N+1) \end{aligned} \right] \end{aligned} \quad (A16)$$

where the subscript  $i$  refers to the  $i^{\text{th}}$  MCS simulation,  $n$  is the total number of simulations and  $m$  is the number of inspections conducted before time  $t$  for life assessment.

#### A.4 Derivation of Interval Probability of Failure

Interval probability of failure  $P_f^{int,i}(N, N+1)$  shown in Equation (3) is determined and modeled based on the concept of conditional expectation method [28], and a strength-conditioned expectation method [29] tailored for aircraft applications. Treating each simulation as a component of an individual aircraft, the initial flaw size, fracture toughness and other time independent random variables are presented by a set of realizations from random simulations. Since the peak flight stress is modeled as an independent random process, the interval failure events  $F^i(N, N+1)$  for respective intervals become independent. In this paper, fracture based failure criterion is used. However, failure criterion based on net section yield can also be used [15]. The residual strength based on fracture mechanics [30] can be represented by the following equation as

$$R^i(t) = k_c^i / \left( \sqrt{\pi a_t^i} \beta(a_t^i) \right) \quad (A17)$$

where  $a_t^i$  is the crack size,  $k_c^i$  is the fracture toughness at flight  $t$  in the  $i^{\text{th}}$  simulation,  $\beta(a_t^i)$  is a given geometry factor. The probability of failure (POF) at flight  $t$  in  $i^{\text{th}}$  simulation conditional on no failures before can be defined as the following equation.

$$POF^i(t) = P[\sigma(t) > R^i(t)] \quad (A18)$$

where failure event for each flight is defined as an event that the peak flight stress  $t$  exceeds residual strength  $R(t)$ . Since  $R(t)$  is a deterministic variable and  $t$  is an independent random process, failure events for all flights are independent. As a result, the probability of survival at flight  $t$  in  $i^{\text{th}}$  simulation can be defined as:

$$P_s^{t,i} = \prod_{k=1}^t [1 - POF^i(k)] \quad (A19)$$

The interval probability of failure  $P_f^{int,i}(N, N+1)$  between  $N^{\text{th}}$  and  $N+1^{\text{th}}$  inspections can be shown below.

$$P_f^{int,i}(N, N+1) = P_s^{t_N^i} - P_s^{t_{N+1}^i} \quad (A20)$$

where  $t_N^i$  is the flight time at  $N^{\text{th}}$  inspection. When maintenance actions such as inspections and repair/replacement are

considered, this probability can be considered as a conditional probability conditioned on no damage detections at all previous N inspections.

#### A.5 Derivation of Equation A14

In this appendix, Equation (A14) is proved. Let's define probabilistic events  $U$  and  $V$  as

$$U = \bigcap_{k=0}^{N-1} g_k^i(a_k^i) < 0 \quad (A21)$$

$$V = \bigcap_{k=0}^N g_k^i(a_k^i) < 0 \quad (A22)$$

Also define probabilistic events  $W$  and  $\bar{W}$  as

$$W = g_N^i(a_N^i) < 0 \quad (A23)$$

$$\bar{W} = g_N^i(a_N^i) > 0 \quad (A24)$$

We can find:

$$UW = V \quad (A25)$$

Since  $W$  and  $\bar{W}$  are mutually exclusive and collectively exhaustive events:

$$U(W + \bar{W}) = U \quad (A26)$$

Expanding Equation (A26), we have

$$UW + U\bar{W} = U \quad (A27)$$

Because  $UW$  and  $U\bar{W}$  are also mutually exclusive events

$$P(UW + U\bar{W}) = P(UW) + P(U\bar{W}) = P(V) + P(U\bar{W}) = P(U) \quad (A28)$$

Finally, we obtain the following equation.

$$P(U\bar{W}) = P(U) - P(V) \quad (A29)$$

By substituting Equations (A21) and (A22) to Equation (A29), we obtain

$$P\left(\left[\bigcap_{k=0}^{N-1} g_k^i(a_k^i) < 0\right] \cap \left[g_N^i(a_N^i) > 0\right]\right) = P\left(\bigcap_{k=0}^{N-1} g_k^i(a_k^i) < 0\right) - P\left(\bigcap_{k=0}^N g_k^i(a_k^i) < 0\right) \quad (A30)$$

And Equation (A14) is proved.

## APPENDIX B – ILLUSTRATION OF FORWARD RECURSIVE SCHEME

The forward recursive scheme is illustrated using Figure B1 with N inspections at inspection time  $t_N^I$  respectively where N = 1 to 3. Without loss generality, we assume the original (non-repaired) and repaired components are made of the same material and under the same load histories. This assumption will be removed in future study. Since the original and repaired components have the same initial quality and loading, they should use the same inspection schedules to maintain identical reliability. For example, if the first inspection for the original component is set at  $t = 4000$  cycles in the global time scale, a repaired component should also be inspected at  $t=4000$  where  $t$  is a local time on the N<sup>th</sup> path.

Based on the assumptions, the probability event tree becomes a “self-similar” tree, similar to a “fractal” structure. Figure B1 illustrates a detail probability event tree with inspections performed at time  $t_N^I = 4000, 7000, 9000$ . The event tree is shown in the green dash box and a global time scale is also shown at bottom. Since the event tree exhibits a “self-similarity” pattern, we can write the following equality.

$$P_f(R^N(t_N)) = CPOF(t) \quad (B1)$$

where  $t$  is in the global time scale and  $t_N$  is in the local time scale;  $t_N = t - t_N^I$ . As can be seen, there is no need to recalculate  $P_f(R^N(t_N))$  for all of the repaired/replaced branches since it has already been calculated. With this observation, forward recursive scheme was developed and is explained next.

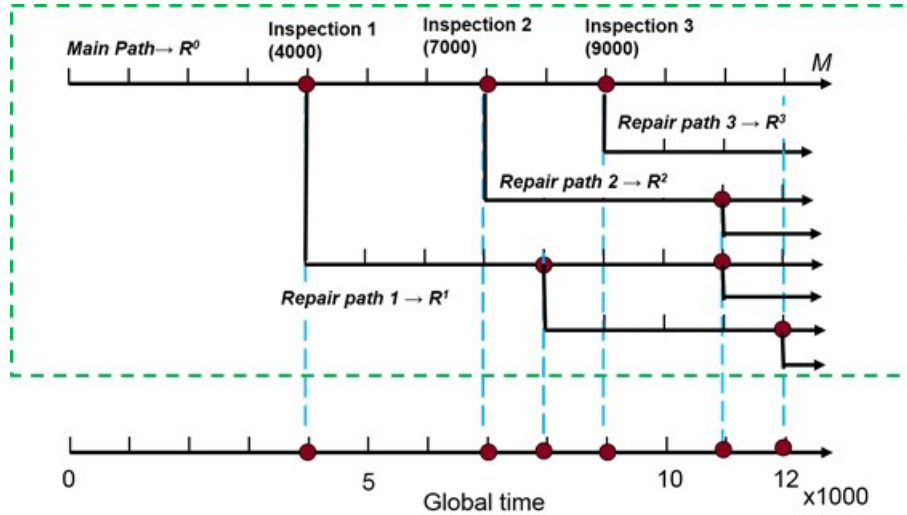


FIG. B1 ILLUSTRATION OF AN EVENT TREE WITH INSPECTION SCHEDULE [4,000 7,000 9,000]

To compute  $CPOF(t=12000)$  using Equation (3),  $P_f(F^i(N, N+1))$  where  $N=0$  to  $3$  along the original fatigue path and  $P_f(R^N(t_N))$  for repair paths 1 to 3 are required. The computation of  $P_f(F^i(N, N+1))$  is explained in Section B.1. From Figure B1,  $P_f(R^1(t_1=8000))$ ,  $P_f(R^2(t_2=5000))$  and  $P_f(R^3(t_3=3000))$  for repair paths 1 to 3 are equal to  $CPOF(t=8000)$ ,  $CPOF(t=5000)$  and  $CPOF(t=3000)$  respectively. It should be pointed out that all the  $CPOF(t)$  for  $t$  less than 12000 were already calculated. With this new forward solution scheme,  $CPOF(t=12000)$  is computed easily and efficiently. Not only computational time is reduced, the repaired and replacement components do not need to be inspected at the same time. Should the qualities of the original and repaired components are different; a second set of RPI analysis should be computed using repair quality to generate  $P_f(R^N(t_N))$  for repair paths.

#### APPENDIX C - DERIVATION OF PROBABILITY OF NO DETECTIONS AT ALL INSPECTIONS

The event of no damage detections for all previous  $N$  inspections  $\bigcap_{k=0}^N M_k^i$  in Equation (3) is the intersection of all individual no-detection events  $M_k^i$ . The probability of the occurrence of such event  $P\{\bigcap_{k=0}^N M_k^i\}$  is defined as PND. As discussed before, individual inspection events can be independent, partially correlated or fully correlated. The model for NDI reliability assessment is now described which will be used to define the correlated inspection events.

##### C.1 NDI Reliability Assessment

Over the last three decades, many NDI reliability assessment programs were conducted, and various quantitative measurements were employed to express the NDI system capabilities [31]. The model developed for reliability assessment of NDI, which is also applicable to INDI system, is used to study the correlation between two inspection events of in-situ sensors on the same component. From the perspective of quantifying the reliability of an INDI system, there is an underlying relationship that must be evaluated between the damage state measurement ( $S_k$ ) and actual damage ( $a_k$ ) as shown in Figure C1. The relationship is commonly represented by the equation:

$$S_k = A + B \ln a_k + X_k \quad (C1)$$

where  $S_k$  is the "apparent" crack size detected by the INDI system and  $X_k$  is the inspection noise (residuals) which is modeled as a correlated random field.  $A$  and  $B$  are derived from linear regression analysis.

Equation C1 is now applied to the  $i^{\text{th}}$  simulation at the  $k^{\text{th}}$  inspection of the probabilistic event tree in Figure A1 and becomes

$$S_k^i = A + B \ln a_k^i + X_k^i = A + B \ln a_k^i + \sigma \sum_{l=1}^k \alpha_{kl} U_l \quad (C2)$$

where correlated random variables  $X_k^i$  for  $k > 0$  are represented as functions of uncorrelated random variables  $U$  via Cholesky decomposition [32];  $a_k^i$  is the predicted crack size at  $k^{\text{th}}$  inspection;  $U$  are standard normal random variables;  $[\alpha]$  is the lower triangular matrix by a Cholesky decomposition of the correlation matrix  $[\rho]$ . The correlation matrix represents the correlation

among all INDI inspection events.

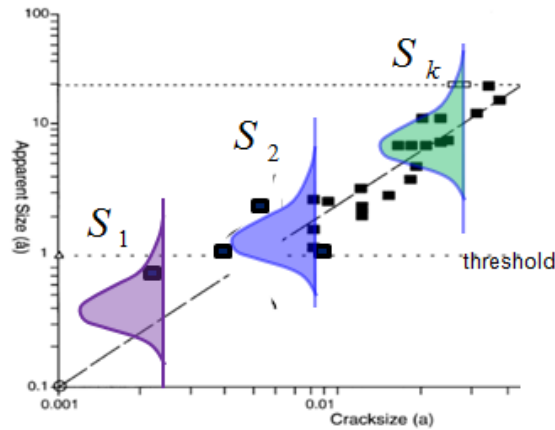


FIG. C1 INDI MEASUREMENT VS. CRACK SIZE

### C.2 Modeling of Correlated Inspection Events

In this section, the POD ( $a$ ) is recast as the probability of a limit function  $g > 0$ . This formulation is useful for employing existing theories in limit state reliability methods to study the correlations among multiple consecutive inspections using INDI. To model the correlated inspection event, a limit state function  $\hat{g}_k^i$  is defined as:

$$\hat{g}_k^i(U) = S_k^i - s_{th} = A + B \ln a_k^i + \sigma \sum_{l=1}^k \alpha_{kl} U_l - s_{th} \quad (C3)$$

where  $s_{th}$  is the detection threshold. The probability of detection for a given crack size  $a_k^i$  is defined in the following equation.

$$POD(a_k^i) = P(\hat{g}_k^i(U) > 0) \quad (C4)$$

Given a POD function, the coefficients  $A$ ,  $B$ ,  $\sigma$  and  $s_{th}$  in Equation (C3) can be found by curve fitting. Furthermore,  $A$  and  $B$  can be treated as additional random variables. The event  $M_k^i$  of no-detection for a given crack size  $a_k^i$  can now be defined as

$$M_k^i = (\hat{g}_k^i(U) < 0) \quad (C5)$$

A different limit state function can also be set by a function transformation. Using the First-Order Reliability Method [33], the limit state function  $\hat{g}$  defined in Equation (C3) can be transformed to a new limit state function  $g$  in Equation (C6) as derived in Section C.3.

$$g_k^i(U) = \beta_k^i + \sum_{l=1}^k \alpha_{kl} U_l \quad (C6)$$

where

$$\beta_k^i = -\Phi^{-1}(1 - POD(a_k^i)) \quad (C7)$$

in which  $\Phi$  is the standard normal CDF. The non-detection event for a predicted crack  $a_k^i$  using Equation (C6) is defined as follows.

$$M_k^i = (g_k^i(U) < 0) \quad (C8)$$

Based on the reliability methods [33], the cosine of the angle between two limit state functions represents the correlation coefficient between two inspections. Given a correlation matrix, the probability of no-detections  $P\{\prod_{k=0}^N M_k^i\}$  can be solved by various numerical methods such as Monte Carlo and Markov-chain simulations. In this paper, the Monte Carlo simulations are used for the proof of concept. More efficient methods desirable for PRA applications will be investigated in the future.

### C.3 Derivation of Equation C6

In this appendix, Equation (C6) is proved. Using the First-Order Reliability Method [33], the limit state function  $\bar{g}$  defined in Equation (C3) can be transformed to a new limit state function  $g$  in Equation (C9).

$$g_k^i(U) = \beta_k^i - \sum_{l=1}^k \bar{\alpha}_{kl} U_l \quad (\text{C9})$$

where

$$[\bar{\alpha}] = -\frac{\nabla \bar{g}(U)}{|\nabla \bar{g}(U)|} \quad (\text{C10})$$

is the normal vector to the limit state surface and the gradients are

$$\nabla \bar{g}(U) = \left( \frac{\partial \bar{g}}{\partial U_1}(U), \dots, \frac{\partial \bar{g}}{\partial U_k}(U) \right) \quad (\text{C11})$$

In Equation (C9),  $\beta_k^i$  is the first-order reliability index and

$$P(g_k^i(U) < 0) = \Phi(-\beta_k^i) \quad (\text{C12})$$

in which  $\Phi$  is the standard normal CDF. Based on the definition of non-detection,

$$P(g_k^i(U) < 0) = 1 - POD(a_k^i) \quad (\text{C13})$$

Therefore

$$1 - POD(a_k^i) = \Phi(-\beta_k^i) \quad (\text{C14})$$

and

$$\beta_k^i = -\Phi^{-1}(1 - POD(a_k^i)) \quad (\text{C15})$$

Substituting Equations (C10) and (C11) to Equation (C9), the limit state function  $g$  can be rewritten for a given crack size  $a_k^i$  as

$$g_k^i(U) = \beta_k^i + \sum_{l=1}^k \alpha_{kl} U_l \quad (\text{C16})$$

which proves Equation C6.

# Investigation on Frequency Responses for Supersonic Intake Based on High Resolution Simulation

Yanping Qin<sup>1</sup>, Junlong Liang<sup>2</sup>

<sup>1</sup>Xi'an Aerospace Propulsion Institute, Xi'an 710100, P.R.China

<sup>2</sup>College of Astronautics, Northwestern Polytechnical University, Xi'an 710072, China

<sup>1</sup>qyp0508@126.com; <sup>2</sup>jiangjl067@163.com

Received: February 1, 2015; Sent for review: February 10, 2015; Accepted: August 5, 2015

## Abstract

The terminal shock within the supersonic inlet is subjected to both internal and external perturbations during the operation of supersonic air-breathing engine. In order to improve the performance of air breathing engine and prevent inlet unstart, it is necessary to control the terminal shock during various disturbance, and determine the dynamics of intake which is valuable for the controller. To simulate the dynamics of intake, high resolution simulation of supersonic inlet based on high order weighted essentially non-oscillatory schemes (WENO) was conducted. To find the interactions of inlet to engine and external conditions, the nonlinear inlet simulation model was subjected to sinusoidal perturbations and the response of shock and static pressure along the inlet in time domain to back pressure and upstream Mach number were obtained and compared to get the dynamics of inlet. Furthermore, the data in time domain were exploited by least-square curve fitting to generate the magnitude ratio and phase shift. Furthermore, according to frequency sweeps, frequency responses of shock position and that of static pressure throughout the intake to back pressure up to 150Hz and free stream Mach number up to 100Hz have been obtained. The results show that frequency response of shock to back pressure is quite different from that to upstream mach number, and the amplitude ratio of static pressure upstream of shock descends with the growth of frequency, while that of pressure downstream of shock reach the peak at several frequencies, which is induced by the movement of shock.

## Keywords

Supersonic Intake; Intake Dynamics; WENO; Frequency Responses

## Introduction

Ramjet technology has evolved in more than hundred years, during which supersonic intake has significant effluence on the maturation of ramjet propulsion[1]. For mixed-compression inlets, optimum internal performance is provided by maintaining the terminal shock near the inlet throat<sup>[2-7]</sup>, which provides higher pressure recovery and reduces flow distortion at the outlet[6]. However, disturbances may occur either upstream or downstream of inlet[2-18]. As shown in Fig1, the terminal shock responds to both upstream from free airstream and downstream disturbances from combustor or compressor, resulting in inlet unstart if terminal shock moves upstream from the throat[9-11]. Unstart causes a sharp reduction in mass flow, pressure recovery and large increase of drag[6-11], what's more, inlet buzz, combustor blowout may occur, so it is valuable to reject unstart, which demands active control of the inlet to keep a stable shock position in the presence of random airflow disturbance and prevent inlet unstart[2,7-10,15].

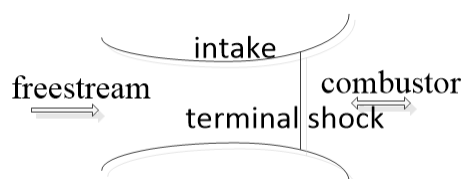


FIG. 1 SCHEME OF INTAKE DYNAMICS

It has attracted much attention to the dynamics of shock motions[9-18]. A low-order model that captures the key features of the shock motions is invaluable for the development of control strategies[9] and the evaluating such a

control[10]. Previous studies have shown that the dynamic model of shock motions oriented for control is established by linearization[9,16], such as theoretical analysis[16], data fitting[10,14,18], or frequency identification[3,17]. The modeling based on linearization is convenient in application. However, it is only suitable to intake flow with small perturbations[6], but unable to represent nonlinearities. Finite difference methods[6,18] can work with variable time step and present time-variant properties with higher resolution[18].

When the flow fields involve shock waves, the numerical schemes should be essentially oscillation free near the discontinuities. In recent years, many efforts have been devoted to the development of high resolution shock-capturing schemes that are higher order accurate in the smooth regions. One class of the numerical schemes among them are higher order ENO and WENO schemes[19-24]. The high resolution simulation code has been completed and verified in Ref [18], the transient responses of shock motion under perturbations coming from free stream and combustor have been calculated and studied, the results show that with the increase of magnitude of the disturbance, the nonlinearity of shock motion becomes more significant. All the analysis of [18] was on time domain responses of shock, and the frequency responses will be presented in this paper to provide a fast, flexible and high accurate method to model the dynamics of intake, which will be useful for the shock position controller design.

The paper is organized as follows. Firstly, the back ground and the state of art of frequency dynamics of supersonic intake were presented. Secondly, the high resolution simulation model was described. Besides, the dynamics of shock and static pressure within the intake in time domain under different frequencies were presented and analyzed. Furthermore, frequency response of intake to back pressure and upstream Mach number were obtained by frequency sweep and least-square curve fitting. Finally, the conclusion is summarized and remarked.

## Mathematical Model

### Governing Equations

In this section, the basic governing equations for solving the one dimensional gas behavior with variable area are presented, and the numerical schemes are simply described to get the gas dynamics. If the cross-sectional area of a flow passage varies very slowly and the radius of curvature of the central axis of the passage is large contrasted to the passage height, the flow inside the passage is said to be a quasi-one-dimensional flow[6]. In this case, the flow properties are assumed to be uniform across all surfaces perpendicular to the mean flow direction. The proper governing equations are as follows.

$$\frac{\partial U}{\partial t} + \frac{\partial F}{\partial x} = J \quad (1)$$

which is equivalent to

$$\begin{cases} \frac{\partial(\rho A)}{\partial t} + \frac{\partial(\rho u A)}{\partial x} = 0 \\ \frac{\partial(\rho u A)}{\partial t} + \frac{\partial(\rho u^2 A + p A)}{\partial x} = p \frac{\partial A}{\partial x} \\ \frac{\partial(\rho A E)}{\partial t} + \frac{\partial(u \rho A H)}{\partial x} = 0 \end{cases} \quad (2)$$

where  $E = e + 0.5u^2$  is the total internal energy,  $e$  is the internal energy,  $H = h + 0.5u^2$  is total internal enthalpy,  $h$  is the enthalpy.  $A$  is the area of inlet,  $u$  is the velocity,  $\rho$  is the density,  $p$  is the static pressure.  $U = [\rho A, \rho u A, \rho A E]^T$  is the vector of conservative variables, and the flux is  $F = [\rho u A, \rho u^2 A + p A, u \rho A H]^T$ ,  $J$  is the source term considering the area variation. It is assumed perfect gas thermodynamics, therefore

$$\begin{aligned} p &= (\gamma - 1) \rho (E - 0.5u^2) \\ a &= \sqrt{\gamma p / \rho} \end{aligned} \quad (3)$$

where  $a$  is the speed of sound,  $\gamma$  is the specific heat ratio, for air  $\gamma = 1.4$ .

### Dimensionless Governing Equations

In this section, the governing equations are non-dimensionalized by using the density, pressure and static temperature as reference density, pressure and temperature, the intake length as the reference length, the throat area as the reference area, and the  $u_f = \sqrt{p_{in}/\rho_{in}}$  as the reference velocity. So the dimensionless dynamic equations of motion (continuity, momentum, and energy) are shown as follows

$$\frac{\partial \tilde{U}}{\partial \tilde{t}} + \frac{\partial \tilde{F}}{\partial \tilde{x}} = \tilde{J} \quad (4)$$

which is equivalent to

$$\begin{cases} \frac{\partial(\tilde{\rho}\tilde{A})}{\partial \tilde{t}} + \frac{\partial(\tilde{\rho}\tilde{u}\tilde{A})}{\partial \tilde{x}} = 0 \\ \frac{\partial(\tilde{\rho}\tilde{u}\tilde{A})}{\partial \tilde{t}} + \frac{\partial(\tilde{\rho}\tilde{u}^2\tilde{A} + \tilde{p}\tilde{A})}{\partial \tilde{x}} = \tilde{p} \frac{\partial \tilde{A}}{\partial \tilde{x}} \\ \frac{\partial(\tilde{\rho}\tilde{A}\tilde{E})}{\partial \tilde{t}} + \frac{\partial(\tilde{u}\tilde{\rho}\tilde{A}\tilde{H})}{\partial \tilde{x}} = 0 \end{cases} \quad (5)$$

The dimensionless perfect gas equations of state and the sonic velocity are as follows

$$\begin{aligned} \tilde{p} &= \tilde{\rho}\tilde{T} = (\gamma-1)\tilde{\rho}(\tilde{E}-0.5\tilde{u}^2) \\ \tilde{a} &= \sqrt{\gamma\tilde{p}/\tilde{\rho}} \end{aligned} \quad (6)$$

Especially, if the area of the duct is constant, the above equations are equivalent to the one dimensional Euler equations.

### Numerical Method

#### 1) WENO Schemes

The fifth-order Finite different scheme is adopted to simulate the shock motion in supersonic intake. When solving the Euler equations, the evaluation of the numerical flux functions for the characteristic-wise finite different WENO scheme involves the following steps:

At each fixed  $\tilde{x}_{j+0.5}$ , the average state  $\tilde{U}_{j+0.5}$  is computed by the Roe average.

$$\tilde{U}_{j+0.5} = B^{Roe}(\tilde{U}_{j+1}, \tilde{U}_j) \quad (7)$$

The eigenvalues  $\tilde{\lambda}_{j+0.5}^i (i=1,2,3)$  and the left eigenvectors  $l_{j+0.5}^i (i=1,2,3)$  and the right eigenvectors of Jacobin  $F'(\tilde{U}_{j+0.5})$  are computed in terms of  $\tilde{U}_{j+0.5}$ .

$$\begin{aligned} R &= R(\tilde{U}_{j+0.5}) \\ L &= L(\tilde{U}_{j+0.5}) \\ \Lambda &= \Lambda(\tilde{U}_{j+0.5}) \end{aligned} \quad (8)$$

Based on the left eigenmatrix  $L$ , the fluxes are transformed into local characteristic flow field using  $V_m = L\tilde{F}_m$ . The local characteristic decompositions of the flux functions at  $x_m (m = j+1-k, j+k)$  are computed using

$$\begin{aligned} w_m^i &= l_{j+0.5}^i \tilde{F}_m^i, i=1,2,3 \\ m &= j-k+1, \dots, j+k \end{aligned} \quad (9)$$

In the local characteristic fields every component is reconstructed by WENO to generate  $\hat{W}_{j+0.5}$  for obtaining the flux  $\hat{F}_{j+0.5}$ . The flux  $\hat{W}_{j+0.5}$  is transformed back into physical space using

$$\hat{F}_{j+0.5} = R\hat{W}_{j+0.5} \quad (10)$$

The Roe type characteristic-wise WENO scheme is less dissipative and thus achieves higher resolution than the WENO scheme based on the flux vector splitting, especially in capturing the contact discontinuities and shear layers in viscous flows[24]. But the Roe type WENO scheme admits rarefaction shocks that do not satisfy the entropy condition, therefore, certain entropy fix procedure is needed. "H-correction" procedure is adopted to calculate every component of  $\hat{W}_{j+0.5}$ , which is showed as follows.

$$w_{j+0.5}^{i,WENO} = \begin{cases} \hat{w}_{j+0.5}^{i,WENO-Roe}, & \min(|\lambda_j^i|, |\lambda_{j+1}^i|) \geq \eta_{j+0.5} \\ \hat{w}_{j+0.5}^{i,WENO-LF}, & \min(|\lambda_j^i|, |\lambda_{j+1}^i|) < \eta_{j+0.5} \end{cases} \quad (11)$$

In the above equation,  $\eta_{j+0.5}$  is determined by

$$\eta_{j+0.5} = \left| \tilde{u}_{j+1} - \tilde{u}_j \right| + \left| \tilde{a}_{j+1} - \tilde{a}_j \right| \quad (12)$$

Every component of characteristic field is calculated as follows:

$$\hat{w}_{j+0.5}^{i,WENO-Roe} = \begin{cases} \hat{w}_{j+0.5}^{i+}, \lambda_{j+0.5}^i \geq 0 \\ \hat{w}_{j+0.5}^{i-}, \lambda_{j+0.5}^i < 0 \end{cases} \quad (13)$$

where the reconstruction of  $\hat{w}_{j+0.5}^{i+}$  and  $\hat{w}_{j+0.5}^{i-}$  is based on the characteristic flux  $w_m^i$ . While the LF flux splitting finite different method is

$$\hat{w}_{j+0.5}^{i,WENO-LF} = \hat{w}_{j+0.5}^{i+} + \hat{w}_{j+0.5}^{i-} \quad (14)$$

where the reconstruction of  $\hat{w}_{j+0.5}^{i+}$  and  $\hat{w}_{j+0.5}^{i-}$  is based on the positive flux and the negative flux.

The high order of WENO attributes to the convex combination of all of the candidate stencils  $v_{j+0.5}^r$ . For 5 order WENO,  $k=3$ , suppose the  $k$  candidate stencils

$$S_r(i) = \{x_{j-r}, \dots, x_{j-r+k}\}, r=0, \dots, k-1 \quad (15)$$

produce  $k$  different reconstructions to the value  $v_{j+0.5}^+$

$$v_{j+0.5}^r = \sum_{m=0}^{k-1} c_{rm} v_{j-r+m}, r=0, \dots, k-1 \quad (16)$$

The coefficient  $c_{rm}$  can be found in Ref [19] and [22]. WENO reconstruction takes a convex combination of all  $v_{j+0.5}^r$  as a new approximation to the cell boundary value  $v_{j+0.5}^+$ .

$$v_{i+0.5}^+ = \sum_{r=0}^{k-1} \omega_r v_{i+0.5}^r \quad (17)$$

The weight coefficient  $\omega_r$  is the key to the success of WENO. For Jiang-Shu[20] nonlinear weights, the weights are defined as

$$\omega_r = \frac{\alpha_k}{\sum_{l=0}^{r-1} \alpha_l}, \alpha_k = \frac{d_k}{(\beta_k + \varepsilon)^p} \quad (18)$$

The coefficient  $d_k$  are the optimal weights, are given by

$$d_0=0.3, d_1=0.6, d_2=0.1 \quad (19)$$

$\beta_k$  is the smoothness indicator of WENO. For WENO-Z scheme, it can be found in Ref [21].

## 2) Source Term

The source term due to geometry is discreted by fourth order central difference

$$\left(\frac{\partial A}{\partial x}\right)_j = \frac{8(A_{j+1}-A_{j-1})-(A_{j+2}-A_{j-2})}{12\Delta x} \quad (20)$$

## 3) Boundary Condition

The inlet plane of intake is supersonic, so the parameter of upstream boundary is given by free stream condition. The outlet is subsonic, with given pressure, so the other parameters of outlet are gotten by extrapolating the internal flow information. What's more, near the boundary, the flux reconstruction may use the ghost nodes, in this case, the weights of stencil with ghost nodes are set to zero. It may reduce the order, but it is very robust.

## 4) Time Integration

In present work, the time integration is performed by means of a three-stage, TVD Runge-Kutta schemes. Defining the semidiscreted form as

$$L_j(v) = -\frac{1}{\Delta x} (\hat{f}_{j+1/2} - \hat{f}_{j-1/2}) \quad (21)$$

Then this schemes is given by

$$\begin{aligned} v_j^{(1)} &= v_j^n + \Delta t L_j(v_j^n) \\ v_j^{(2)} &= \frac{3}{4} v_j^n + \frac{1}{4} v_j^{(1)} + \frac{1}{4} \Delta t L_j(v_j^{(1)}) \\ v_j^{(n+1)} &= \frac{1}{3} v_j^n + \frac{2}{3} v_j^{(2)} + \frac{2}{3} \Delta t L_j(v_j^{(2)}) \end{aligned} \quad (22)$$

In order to keep the high accuracy, the time step is determined by

$$\Delta t = \sigma \frac{(\Delta x)^{5/3}}{\max_j (|u_j| + a_j)} \quad (23)$$

when  $\sigma$  is the courant number,  $0 < \sigma < 1$ , the solution is stable. In order to obtain constant output time interval, the final step was slightly adjusted.

## 5) Shock Detector

In order to analysis the dynamics of shock position, the key to success is the shock detector. The most simple method is that possible method is to use the pressure variation just like MacCormack scheme with

$$q_j = \frac{|p_{j-1} - 2p_j + p_{j+1}|}{|p_{j-1} + 2p_j + p_{j+1}|} \quad (24)$$

In the smooth area, the parameter  $q_j$  is

$$q_j = \frac{\left| \frac{\partial^2 p}{\partial x^2} (\Delta x)^2 + O((\Delta x)^4) \right|}{\left| 4p_j + O((\Delta x)^2) \right|} \quad (25)$$

so the  $q_j$  is very small. While near the shock,  $q_j$  is very large. In this case, the peak position is defined as shock

front. If this position was defined as shock position, as shown in Ref [18], the shock position discontinues which was caused by the space step of the grid point. In reality, the motion of shock continues, so the interpolation around the shock front area is utilized to obtain shock position, which is defined as the location where the Mach number is one.

## Results and Discussion

### Dynamic Response Analysis

In this paper, the geometry of the supersonic inlet and the boundary condition are the same as Ref [18]. For clarity, it is shown again. The dimensionless area of intake varies with  $\tilde{x}$  only:

$$\tilde{A} = \begin{cases} 1 + (\tilde{A}_{in} - 1)(25(x - 0.2)^2), & 0 < \tilde{x} \leq 0.2 \\ 1 + (\tilde{A}_e - 1)(1.5(1.25x - 0.25)^2 - 0.5(1.25x - 0.25)^4), & 0.2 < \tilde{x} \leq 1 \end{cases} \quad (29)$$

where  $\tilde{A}_{in}$  is the ratio of inlet area to the throat area and given as 1.1, and  $\tilde{A}_e$  is the ratio of outlet area to the throat area and specified as 2. The free stream Ma number is selected as 2.5, the initial shock position is specified as 0.6.

In this section, the numerical solution has been computed on 100 uniform grids using a Courant number 0.5 at timespan of 20ms. The upstream static temperature is taken to be 300K, the total inlet length is 2m. The simulation is done on dimensionless algorithm and has been verified in Ref[18].

The static pressures at  $\tilde{x}=0.3$  and 0.7 are recorded to give the dynamic response of pressure, with simplicity the two points are numbered as U and D along the flow direction. Point U locates in the upstream of initial shock position, and point D in the downstream of initial shock position. The shock position is identified by combination of shock detector and interpolation method, which means the discrepancy of shock position and theoretical ones with one space interval.

The responses of inlet to back pressure and upstream Mach number with relative magnitude lower than 10% were linear, and thereby the relative disturbance magnitude was set to 5%. The dynamic response of shock position to the symmetrical sinusoidal back pressure with frequency at 10Hz, 20Hz and 40Hz were calculated, and the numerical results are plotted in Fig2.

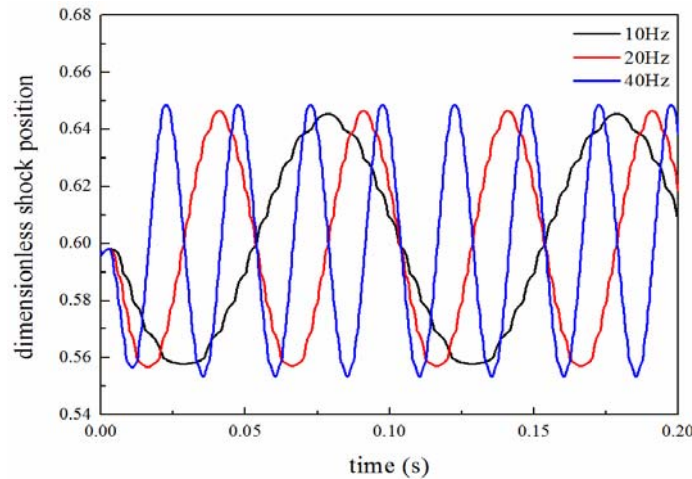


FIG.2 TIME DOMAIN RESPONSE OF SHOCK POSITION TO BACK PRESSURE AT DIFFERENT FREQUENCIES

As shown in Fig2, after a short dead time, shock starts to move upstream with the increase of back pressure, the shock moves between 0.54 and 0.66, which means it can't reach Point U or D. Besides, after one period the wave shape is nearly similar to each other with the same peak values. The peak shock position at 40Hz is slightly larger than that at 10Hz and 20Hz, which suggests that there may be a resonance roughly at 40Hz. The shock moves smoothly, which implies the effectiveness of the improvement of shock detector. It is clear that the period of shock shortens with the increase of the exciting frequency.

The dynamic responses of shock position to the symmetrical sinusoidal upstream Mach number with frequency at 10Hz, 20Hz and 40Hz were computed, and the numerical results are presented in Fig3.

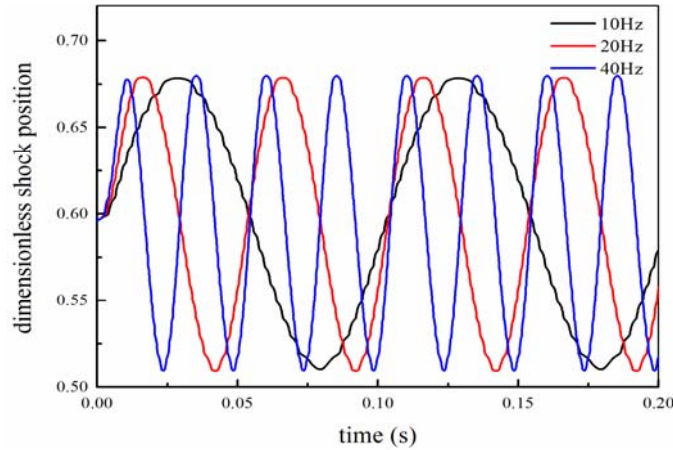


FIG.3 FREQUENCY RESPONSE OF SHOCK POSITION TO UPSTREAM MACH NUMBER AT DIFFERENT FREQUENCIES

As shown in Fig3, after a very short dead time, shock moves downstream with the increase of upstream Mach number, the shock moves between 0.5 and 0.7, which means it can't reach Point U or D. The wave shape are nearly identical to each other during each period, with the same peak values. The peak shock position at 40Hz is slightly larger than that at 10Hz and 20Hz, and the peaks are roughly the same at lower frequency. The period of shock position decreases as the frequency of disturbance grows.

#### *Frequency Response of Supersonic Intake*

The high resolution simulation model of supersonic inlet was perturbed by upstream Mach number or back pressure with the shape of sin wave, so the dynamic response can be generated, however, it is difficult to get the amplitude ratio and phase shift, which is important for frequency responses. In order to solve this problem, the curve fitting based on least square method was utilized to determine the frequency characteristics, namely the frequency responses of supersonic intake to upstream or downstream perturbations. In order to capture the frequency characteristic lower than 150Hz, the sample frequency must be larger than 300Hz, in this paper, the sample frequency is 1000Hz. Furthermore, the computed time is nearly at 0.001 ms, so it's very robust to temporal resolution and space resolution.

#### *Back Pressure Perturbation*

The frequency response results of shock to back pressure at frequency up to 150Hz are plotted in Fig4, and the amplitude curve is plotted as normalized amplitude ratios which are normalized by dividing by the amplitude ratio at 1Hz. It is clearly there is a resonance at about 49Hz. The phase lag increases as the frequency grows. In addition, the frequency response of shock to back pressure is very similar to that of lag element.

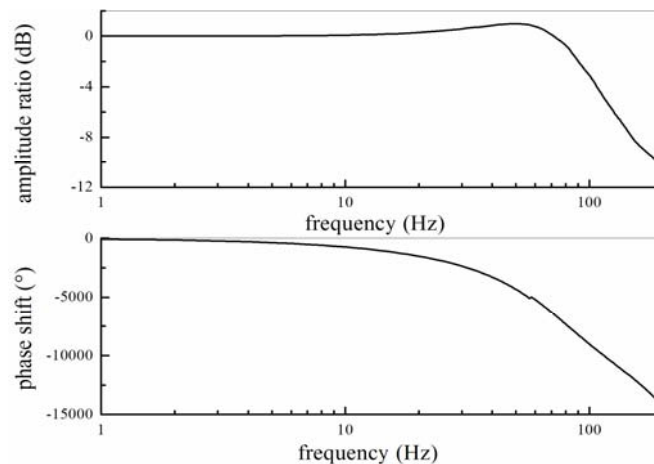


FIG.4 FREQUENCY RESPONSE OF SHOCK POSITION TO BACK PRESSURE

It is clear from Fig3, shock can't move forward to point U, which is located in fully supersonic regime, and is only affected by upstream disturbance, so the static pressure at Point D is given in Fig5, the magnitude ratio of static pressure at D nearly keeps constant when frequency is lower than 10, and then surges as frequency goes up, and then reaches the peak at 55Hz, the resonance of static pressure downstream of shock is very similar to that of the shock. The difference may lie in that the downstream of shock is subsonic and affected by both the downstream perturbation and the upstream movement of shock. It is clear that the upstream of shock is supersonic flow and can't be affected by back pressure disturbance at outlet, and the flow which changes with downstream disturbance is located between outlet and shock, so it forms a closed chamber with closed ends and in this condition it is easy to generate resonance.

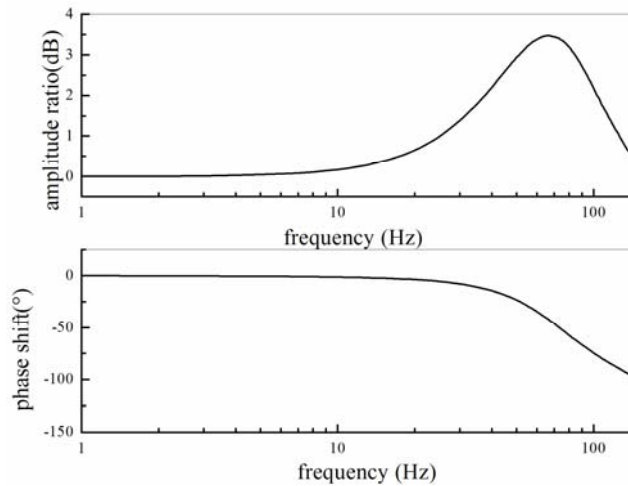


FIG.5 FREQUENCY RESPONSE OF STATIC PRESSURE TO BACK PRESSURE

#### *Upstream Mach Number Perturbations*

The calculated results of frequency response of shock position to upstream Mach number are shown in Fig6. It is clearly there are several peaks at 6Hz, 26Hz, 48Hz, and 64Hz, which implies that the dynamics may be represented by the distributed system. The phase lag is smaller that of shock to back pressure, in that it needs shorter time for disturbance propagating from inlet plane to shock during which the velocity of characteristic waves is very large in supersonic duct.

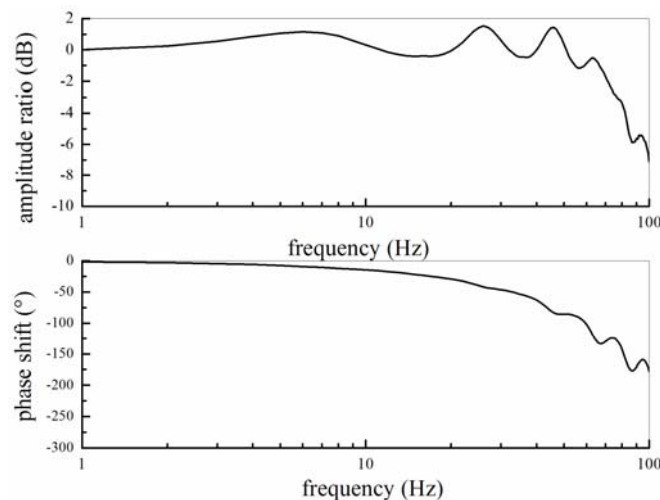


FIG.6 FREQUENCY RESPONSE OF SHOCK TO UPSTREAM MACH NUMBER

The magnitude of each response rises with the growth of frequency for pressure located at U and D, and it changes slowly with frequency less than 10Hz, however, with the growth of frequency, the magnitude of pressure response at point D has more peaks, while that at point U is quite different, it grows as frequency increases. The difference may lie in that point U is only affected by upstream as shown in Fig3 (shock can't reach point U), while point D is affected by both downstream and upstream. The magnitude curve of static pressure at D is very complex coupled

with more peaks than that of shock position. As showed in Fig7, the phase lag grows with the growth of frequency, and the difference between that of pressure at U and D is very small.

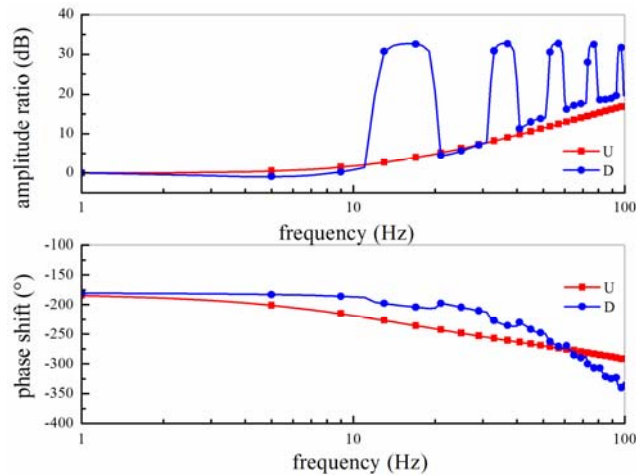


FIG.7 FREQUENCY RESPONSE OF STATIC PRESSURE WITHIN THE INLET TO UPSTREAM MACH NUMBER

## Conclusions

The frequency dynamics of shock and static pressure throughout the supersonic intake are investigated by perturbing the high resolution simulation model, and the conclusions are summarized as follows.

The frequency of shock movement increases with the growth of the frequency of the external disturbance. The amplitude ratio of shock to back pressure and upstream Mach number changes slowly at frequency lower than 20Hz.

The frequency response of shock to upstream Mach number is quite different from that to back pressure with more peaks in the magnitude curve and smaller phase lag.

The frequency response of static pressure downstream of shock to back pressure is quite similar to that of shock, which can be represented by lag element.

The frequency responses are very complex, so in the future the rational polynomial transfer function approximation may be introduced by frequency identification, and be reduced by the model reduction to get low order transfer function for controller design.

## REFERENCES

- [1] Ronald S. Fry. "A Century of Ramjet Propulsion Technology Evolution." *Journal of Propulsion and Power*, 20(2004):27-58.
- [2] Bruce Lentine, John R. Z. "Application of Quadratic Optimization to Supersonic Inlet Control." *Automatics*, 8(1972):563-574.
- [3] George K, Joseph W. Connolly." Shock Positioning Controls Design for a Supersonic Inlet." AIAA 2009-5117.
- [4] Jun-Woo Park, Ik-Soo Park, Min-Jea Tahk." Adaptive Backstepping Nonlinear Controller Design for Shock Position Control of Supersonic Engine." *The 11th International Conference on Control, Automation and Systems*, Oct.26-29, 2011 in KINTEX, Gyeonggi-do, Korea.
- [5] Jun-Woo Park, Ik-Soo Park, Bong-Gyun Seo, et al. "Optimal Terminal Shock Position Under Disturbances for Ramjet Supercritical Operatio." *Journal of Propulsion and Power*, 29(2013):238-248.
- [6] M. O. Varner, W. R. Martindale, W. J. Phares, et al. "Large perturbation flow field analysis and simulation for supersonic inlets final report." NASA CR 174676, 1987.
- [7] George H. Neiner, Michael J. Crosby, Gary L. C. "Experimental and analytical investigation of fast normal shock position controls for a mach 2.5 mixed-compression inlet." NASA TN D-6382, 1971.
- [8] SC Himmel. "Some Control Considerations for Ram-jet Engines." NACA RM E52F10, 1952.

- [9] Douglas G. MacMartin. "Dynamics and Control of Shock Motion in a Near-Isentropic Inlet." *Journal of aircraft*, 41(2004):846-853.
- [10] Ik-Soo Park, Sun-Kyoung Kim, Hyo-Won Yeom, et al. "Control-Oriented Model for Intake Shock Position Dynamics in Ramjet Engine." *Journal of Propulsion and Power*, 27(2011):499-503.
- [11] Ik-Soo Park, N. Ananthkrishnan, Min-Jea Tahk, et al. "Low-Order Model for Buzz Oscillations in the Intake of a Ramjet Engine." *Journal of Propulsion and Power*, 27(2011):503-506.
- [12] Vasu G, Wilcox F A, Himmel S C. "Preliminary Report of Experimental Investigation of Ram-Jet Controls and Engine Dynamics." NACA RM E54H10, 1954.
- [13] N K Gupta, B K Gupta, N Ananthkrishnan, et al. "Integrated Modeling and Simulation of an Air-breathing Combustion System Dynamics." "AIAA2007-6374.
- [14] P B C Kumar, N K Gupta, N Ananthkrishnan, et al. "Modeling, Dynamic Simulation, and Controller Design for an Air-breathing Combustion System." "AIAA2009-708.
- [15] Takao Ohshima, Katsuhiko Kanbe, Hideo Kimura, et al. "Control of the Intake Shock Position in the Test Rig for Ramjet Engine." "AIAA1997-2885.
- [16] Willoh R G. "A mathematical analysis of supersonic inlet dynamics." "NASA TN D-4969,1968.
- [17] Qin Yan-ping, LI Bin, Liang Jun-long. "Rational Polynomial Transfer Function Approximations for Supersonic Inlet Dynamics." *Journal of Propulsion Technology*, 34(2013):583-388.
- [18] Qin Yan-ping, LI Bin, Liang Jun-long. "High Resolution Numerical Simulations on Dynamics of Intake Shock Motion." The 65th International Astronautical Congress, Toronto, Canada, IAC-14-C4.8.8, 2014.
- [19] Chi-wang Shu. "Essentially non-oscillatory and weighted essentially non-oscillatory schemes for hyperbolic conservation laws ." NASA/CR 97-206253.
- [20] Guang-Shan Jiang, Chi-Wang Shu. "Efficient Implementation of Weighted ENO Schemes." *Journal of Computational Physics*, 126(1996): 202-228.
- [21] R. Borges, M. Carmona, B. Costa, et al. "An improved weighted essentially non-oscillatory scheme for hyperbolic conservation laws." *Journal of Computational Physics*, 227(2008):3191-3211.
- [22] G. A. Gerolymos, D. Senechal, I. Vallat. "Very-high-order WENO schemes." *Journal of Computational Physics*, 228(2009):8481-8524.
- [23] Marcos Castro, Bruno Costa, Wai Sun Don. "High order weighted essentially non-oscillatory WENO-Z schemes for hyperbolic conservation laws." *Journal of Computational Physics*, 230(2011):1766-1792.
- [24] Yu-Xin Ren, Miao'er Liu, Han-xin Zhang. "A characteristic-wise hybrid compact-WENO scheme for solving hyperbolic conservation laws." *Journal of Computational Physics*, 192(2003): 365-386.

# Numerical Flow Simulation over a Flapping Wing Using Implicit RANS Solver

Sharanappa V. Sajjan\*<sup>1</sup> and K. Siva Kumar<sup>2</sup>,

Computational and Theoretical Fluid Dynamics Division, Council of Scientific and Industrial Research-National Aerospace Laboratories, Bangalore, Karnataka, India-560017

\*<sup>1</sup>svsajjan@ctfd.cmmacs.ernet.in; <sup>2</sup>shivak@ctfd.cmmacs.ernet.in

Received: March 27, 2015; Sent for review: April 3, 2015; Accepted: August 5, 2015

## Abstract

Numerical simulations are performed for the flow past a flapping wing to study the effect of reduced frequency on the thrust generation and propulsive efficiency. Time accurate solution has been obtained by using an implicit RANS solver IMPRANS that employs finite volume nodal point spatial discretization scheme with dual time stepping. The efficiency of the solver for making time-accurate computations is enhanced by implementing an implicit dual time stepping procedure. In this approach, an equivalent pseudo steady state problem is solved at each real time step using local time stepping. The algebraic eddy viscosity model due to Baldwin and Lomax is used for turbulence closure. The computations are carried out by varying the reduced frequencies (from  $k = 0.5$  to  $k = 1.0$ ) to study the effect on thrust generation and propulsive efficiency at Mach number 0.3 and Reynolds number  $10^5$ . The results are obtained in the form of aerodynamic coefficients, thrust coefficient and propulsive efficiency.

## Keywords

*Unsteady Flow; RANS Solver; Implicit Method; Dual Time Stepping; Flapping Wing*

## Introduction

Micro Air Vehicles (MAVs), Nano Air Vehicles (NAVs) and Small Unmanned Air Vehicles (UAV's) have gained increasing interest over the past few years due to many applications such as civilian, rescue missions, defence applications or military surveillance missions. They should be able to fly inside and outside the building, around street corners or attach on the window whenever necessary.

In the olden days, the major idea of utilizing the thrust generated by flapping wings for the propulsion of man-made objects such as MAVs, NAVs and remote controlled small unmanned aerial vehicles (UAV's) etc. emerged from observations of birds, insects, fish etc.

Birds or insects while flying, they perform flapping motion (i.e., combined pitching and plunging motion with some phase difference between them) and they produce more lift and thrust compared with stationary wings. There are practical benefits as well: flapping wings potentially offer improved efficiency, better maneuverability and reduced noise compared with the rotary-driven aeroplanes and helicopters. At present, there are many scientific works are undergoing in several countries to develop small aerial vehicles which use flapping-wing systems. So, there is a need for detailed understanding of the flow physics behind combined pitching and plunging (flapping) wings which will help in the design of flapping wings for MAVs, NAVs and small UAVs etc.

Wei Shyy et al. [1] discussed kinematics of flapping wings and aerodynamic models for analyzing lift, drag and power. They also presented the issues related to low Reynolds number flows and aerofoil shape selection. Trizila et al. [2] numerically investigated two and three-dimensional hovering airfoil/wing aerodynamics at a low Reynolds number. For selected kinematics, they also examined the environmental sensitivity during hovering. Wei Shyy et al. [3] reviewed the important features related to the aerodynamics associated with rigid flapping wings and flexible flapping wings. Christopher and Anouck [4] presented an overview of the various analyses of flight dynamics, stability and control of flapping wing micro-air vehicles. The majority of stability issues focused on linear, time-

invariant stability in the vicinity of reference flight conditions, such as hover or forward flight. Alessandro et al. [5] investigated the behavior of two-dimensional symmetric flapping wings moving in a viscous fluid. They performed some numerical simulations by solving the fluid-structure interaction problem through a strongly coupled partitioned approach. Also, they employed Monte Carlo simulation strategy to characterize the flight behavior subjected to lateral wind conditions. The challenges facing future Micro Air Vehicle development was described by Pines and Bohorquez [6]. Ashraf et al. [7] reviewed the recent computational and experimental studies in the context of two dimensional flapping wing in forward flight. They performed preliminary CFD study to analyse the effects of the reduced frequency ( $k$ ), amplitude of oscillation ( $h$ ) and the maximum non-dimensional flapping velocity ( $kh$ ) on the thrust generation and propulsive efficiency of a NACA 0012 airfoil undergoing pure plunge motion at a Reynolds number of 20,000. Tatjana and Cameron [8] experimentally investigated the aerodynamic forces of an avian flapping wing model system that was performed in a wind tunnel at Reynolds numbers between 28,000 and 141,000 (3 -15 m/s), throughout a range of reduced frequencies between 0.04 and 0.20. They showed the comparison between the PIV measurements in the two perpendicular planes and the direct force balance measurements, and concluded that within certain limitations, the wake visualization was a powerful tool to gain insight into force generation and the flow behaviour on flapping wings over the wing beat cycle. Zaeem Khan and Sunil Agrawal [9] designed and fabricated a robotic flapper which could flap dynamically scaled wings in a desired kinematic pattern. An aerodynamic model and wing testing methodology was developed based on unsteady aerodynamic mechanisms. They mentioned that, the model additionally accounted for the wing twisting. They concluded that the model can be used in the aerodynamic module for the determination of aerodynamic force and moment components. For any given wing shape, the coefficients must be determined using the robotic flapper; procedure could also be used to optimize wing geometry and wing kinematics. Kamali and Rezaei Ravesh [10] developed a computer code based on the unsteady panel method which was capable of modelling MAV's flapping wings in different unsteady conditions at low Reynolds number. They computed the aerodynamic design coefficients using that code. At the end the optimum wing shape and flapping frequency were discussed as other findings of their study. From the results they concluded that, more lift force was produced if the wing span to chord ratio or angle of attack or flapping frequency and flapping amplitude increased.

In the present work, we have performed three-dimensional unsteady flow simulation over a flapping wing to study the effect of reduced frequency on the thrust generation and propulsive efficiency at a Mach number of 0.3 and Reynolds number of  $10^5$  for different reduced frequencies ( $k = 0.5$  to  $k = 1.0$ ). The following sections briefly describe about RANS solver IMPRANS, grid generation, results and finally the conclusions.

### Imprans Solver

The Reynolds-averaged Navier-Stokes equations for three-dimensional unsteady compressible viscous flow in a moving domain in non-dimensional conservative form are given by

$$\frac{\partial \bar{U}}{\partial t} + \frac{\partial E}{\partial x} + \frac{\partial F}{\partial y} + \frac{\partial G}{\partial z} = 0. \quad (1)$$

Here,  $\bar{U}$  is the vector of conserved variables,  $E$ ,  $F$  and  $G$  flux vectors,  $(x, y, z)$  is the Cartesian coordinate system and  $t$  is the time variable.

An implicit finite volume nodal point scheme with dual time stepping approach [11 - 14] is employed for solving the above governing equations (1). The dual time stepping consists of an implicit discretization in real time and the marching of solution in a pseudo time to steady state at each physical time step. Use of an implicit second order accurate backward difference formula for discretization in real time and Euler's implicit time differencing formula for pseudo time results are in the following equation

$$\left[ I + \frac{3\Delta t^*}{2\Delta t} I + \Delta t^* \left( \frac{\partial R}{\partial U} \right)^m \right] \Delta U^m = -\Delta t^* \left[ R(U^m) + \frac{3U^m}{2\Delta t} - \frac{2\bar{U}^n}{\Delta t} + \frac{\bar{U}^{n-1}}{2\Delta t} \right] \quad (2)$$

Here  $U^m = U(t^*) = U(m \Delta t^*)$  is the solution vector at pseudo time level  $m$ ,  $\Delta U^m = U^{m+1} - U^m$  is the change in  $U^m$  over the time step  $\Delta t^*$  and  $\Delta t$  denotes the real or physical time step that is required to resolve the physical unsteadiness

of the flow. The barred quantities denote the solution vectors at the previous real time levels  $n$  and  $n - 1$  whereas  $R$  represents the spatial operators which give rise to the flux residual after a discretization in space.

This basic equation (2) of the implicit dual time stepping technique can be solved at each real time step by employing a finite volume nodal point spatial discretization scheme. In this approach, the flow variables are associated with each mesh point  $(i, j, k)$  of the grid and the centroids of the eight neighbouring hexahedron cells surrounding the nodal point are joined to form the control volume  $\Omega_{ijk}$ . To facilitate the finite volume formulation, the equations are written in an integral form and the surface integrals are evaluated by summing up the contributions due to the flux terms over the six faces of the computational cell. Applying integral conservative equations to each control volume, linearising the changes in flux vectors using Taylor's series expansions in time, assuming locally constant transport properties, and dropping the superscript  $m$  we obtain

$$\begin{aligned}
& \left( I + \frac{3\Delta t^*}{2\Delta t} I \right) \Delta U_{ijk} + \frac{\Delta t^*}{\Omega_{ijk}} \sum_{m=1}^6 \left\{ \left[ \left( A - \frac{\partial E_R}{\partial x} \right) \Delta U \right] S_{mx} \right. \\
& \left. + \left[ \left( B - \frac{\partial F_s}{\partial y} \right) \Delta U \right] S_{my} + \left[ \left( C - \frac{\partial G_T}{\partial z} \right) \Delta U \right] S_{mz} \right\} \\
& = - \frac{\Delta t^*}{\Omega_{ijk}} \left\{ \sum_{m=1}^6 \left[ (E_I - E_V)_m S_{mx} + (F_I - F_V)_m S_{my} + (G_I - G_V)_m S_{mz} \right] \right\} \\
& - \Delta t^* \left( \frac{3\bar{U}_{ijk}}{2\Delta t} - \frac{2\bar{U}_{ijk}^n}{\Delta t} + \frac{\bar{U}_{ijk}^{n-1}}{2\Delta t} \right), \tag{3}
\end{aligned}$$

Here  $\Omega_{ijk}$  is the control volume surrounding the nodal point  $(i, j, k)$  of the curvilinear grid;  $A = \partial E_I / \partial U$ ,  $B = \partial F_I / \partial U$ ,  $C = \partial G_I / \partial U$ ,  $E_R = \partial E_V / \partial U_x$ ,  $F_s = \partial F_V / \partial U_y$  and  $G_T = \partial G_V / \partial U_z$  are the Jacobian matrices;  $E_I$ ,  $F_I$  and  $G_I$  are the inviscid flux vectors and  $E_V$ ,  $F_V$  and  $G_V$  are the viscous flux vectors;  $S_{mx}$ ,  $S_{my}$  and  $S_{mz}$  are the  $x$ ,  $y$  and  $z$  components of the surface vector corresponding to the  $m^{\text{th}}$  surface of the control volume.

It is important to note that the terms containing inviscid flux vectors can be calculated by using the flow variables at the six neighbouring points and Taylor's series expansions can be utilised to discretize the derivatives in the viscous flux terms directly in the physical plane. The resulting block tridiagonal system of equations is solved by using a suitable block tridiagonal solution algorithm and proper initial and boundary conditions. In order to ensure convergence and to suppress oscillations near shock waves, a blend of second and fourth order artificial dissipation terms [15] is added explicitly. Implicit second order dissipation terms are also added to improve the practical stability bound of the implicit scheme. The algebraic eddy viscosity model due to Baldwin and Lomax [16] is used for turbulence closure. For a moving body, the equations are solved in the inertial frame of reference by employing a grid which remains fixed to the body and moves along with it. At each real time step  $t + \Delta t$ , starting from the solution at the previous time step  $t$ , the solution is marched in pseudo time  $t^*$  using local time stepping. Since the choice of physical time step  $\Delta t$  is no longer limited by stability considerations, a much larger time step, with a fixed but small number of inner iterations in pseudo time, can be used to reduce the undesirably large computational time for unsteady flow calculations. Based on this dual time stepping method an implicit Reynolds averaged Navier-Stokes solver IMPRANS has been developed at NAL for computing a wide variety of two-dimensional and three-dimensional unsteady viscous compressible flows. This RANS solver has been extensively validated for computing unsteady flow past pitching aerofoils and wings [17], plunging aerofoils and wings [18, 19], flapping aerofoils [20, 21], helicopter rotor blades [12, 13], wind turbines [14] etc. Here, the solver has been applied for simulating three-dimensional unsteady compressible viscous flow over a combined pitching and heaving rectangular NACA 0012 wing at different reduced frequencies.

## Grid Generation

For all the present simulations, a structured single block C-H-type grid around a NACA 0012 rectangular wing with an aspect ratio of 4 was used which is shown in Fig. 1(a). The surface grid is shown in Fig. 1(b). The number of grid points is  $247 \times 65 \times 62$  in the chord wise, normal and span-wise directions respectively. The points are

clustered near the leading and trailing edges and wing tip properly to capture the flow gradients. The grid spacing normal to the wall was  $2.0 \times 10^{-5}c$  used.

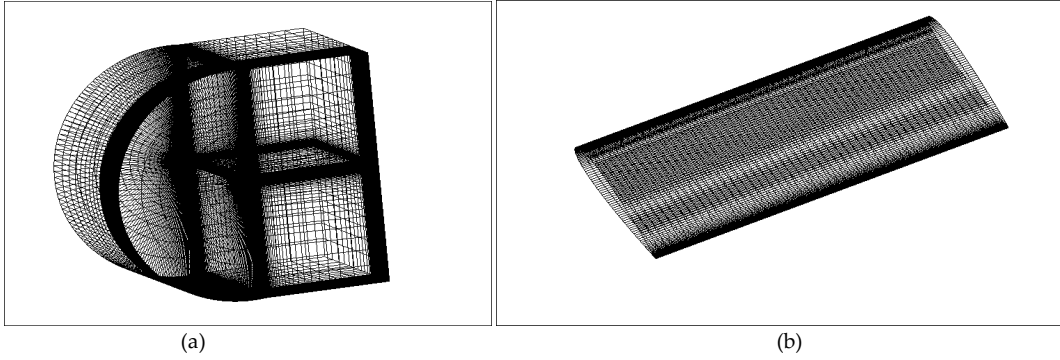


FIG. 1 (a): C-H TOPOLOGY GRID AROUND THE WING; (b): SURFACE GRID ON THE WING

### Flapping Motion of the Wing

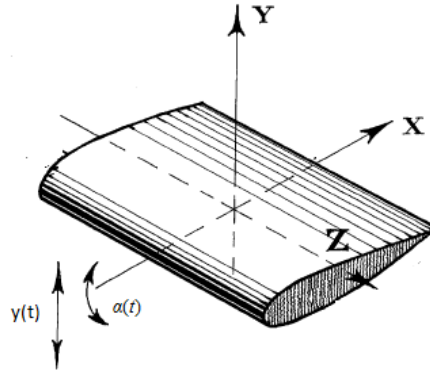


FIG. 2: SCHEMATIC DIAGRAM SHOWING FLAPPING MOTION OF THE WING

The sinusoidal motion of combined pitching and heaving / plunging wing is shown in Fig. 2 and is defined by the following expressions.

The pure plunge or heave motion in normal direction is defined by

$$y(t^*) = h_a \sin(k t^*) \quad (4)$$

and the plunging velocity is given by the following expression

$$\dot{y}(t^*) = h_a k \cos(k t^*) \quad (5)$$

The coupled pitching oscillation is defined as rotating about a pivot point on the aerofoil chord. The instantaneous angle measured clockwise from the mean chord is  $\alpha(t^*)$  which is given by

$$\alpha(t^*) = \alpha_m + \alpha_o \sin(k t^* + \phi) \quad (6)$$

where  $\alpha_o$  is the amplitude of pitching oscillation,  $\alpha_m$  is the mean angle of attack,  $k$  is the reduced frequency,  $h_a$  is non-dimensional heave amplitude  $h_a$  and  $\phi$  is the phase angle ahead of the plunging motion.

The mean thrust coefficient and propulsion efficiency are computed using the following expressions. The mean or time-averaged thrust coefficient is defined as

$$\overline{C}_t = -\overline{C}_d + (C_d)_{\text{steady}} \quad (7)$$

where  $\overline{C}_d$  is the mean drag coefficient, averaged for one flapping period.  $(C_d)_{\text{steady}}$  is the steady drag of the non-moving wing at its present angle of attack.

The propulsive efficiency ( $\eta_{\text{prop}}$ ) can be calculated from the ratio between power output and power input. In this case, this is given by ratio of mean drag coefficient ( $\overline{C}_d$ ) to mean input power coefficient where mean power input coefficient is calculated from the product of lift coefficient,  $C_l$  and plunging velocity,  $\dot{y}(t^*)$ .

Results and Discussion

The numerical simulations have been carried out for three-dimensional unsteady viscous flow over a combined pitching and heaving rectangular NACA 0012 wing having aspect ratio of 4, for different reduced frequencies ( $k = 0.5$  to  $k = 1.0$ ) at a Mach number of 0.3 and Reynolds number of  $10^5$ . For all the simulations, steady state solutions are first obtained. After steady state convergence is reached, the wing then undergoes a prescribed sinusoidal motion, both pitching about half chord (i. e,  $a = c/2$ ) and heaving motion. For all the cases, five consecutive cycles were computed to obtain periodic solution.

The non-dimensional time step,  $\Delta t = 0.005$  (approx.), the non-dimensional plunge amplitude of 1.0, the amplitude of pitching motion is  $20^\circ$  and the phase angle between the pitching and heaving motion  $90^\circ$  were used at different reduced frequencies.

The IMPRANS solver has been previously, validated for the unsteady flow over a flapping aerofoil (combined pitching and plunging) with the experimental and numerical data available in the literature in [20]. The same solver has been used in the present simulations.

Figs. 3 (a) and 3 (b) represent the coefficient of lift and thrust versus the angle of attack for a combined pitching-heaving rectangular wing computed by using IMPRANS solver at  $0^\circ$  mean angle of attack and at reduced frequency of 0.83. Similarly for the above case, the force coefficients are plotted versus heaving distance are shown in Figs. 4 (a) and 4 (b) respectively. The computed loops of the lift and thrust coefficients clearly demonstrate the hysteresis property existing between the up-stroke and down-stroke. The lift values are higher during down stroke than those during up stroke. The thrust values are positive throughout the cycle of flapping oscillation.

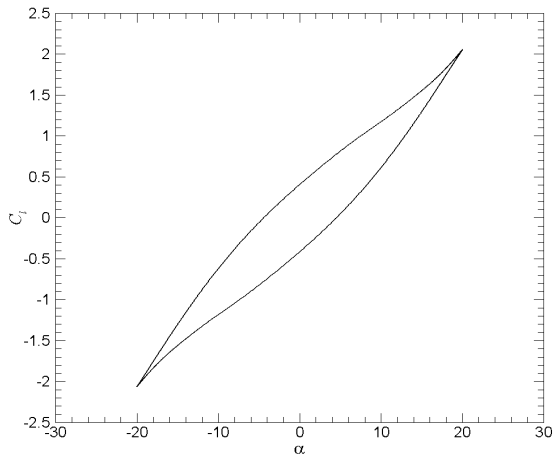


FIG. 3(a): COEFFICIENT OF LIFT VERSUS ANGLE OF ATTACK FOR THE FINAL CYCLE

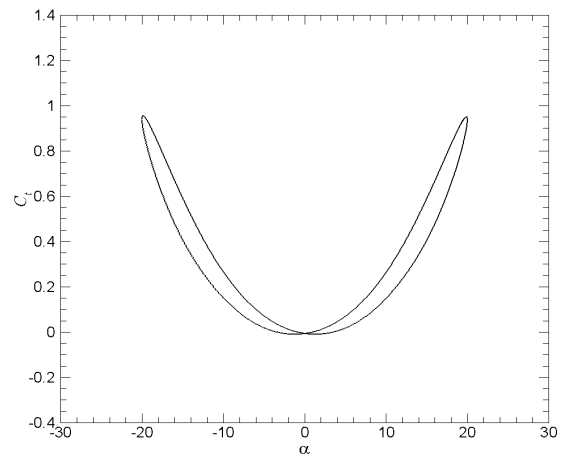


FIG. 3(b): COEFFICIENT OF THRUST VERSUS ANGLE OF ATTACK FOR THE FINAL CYCLE

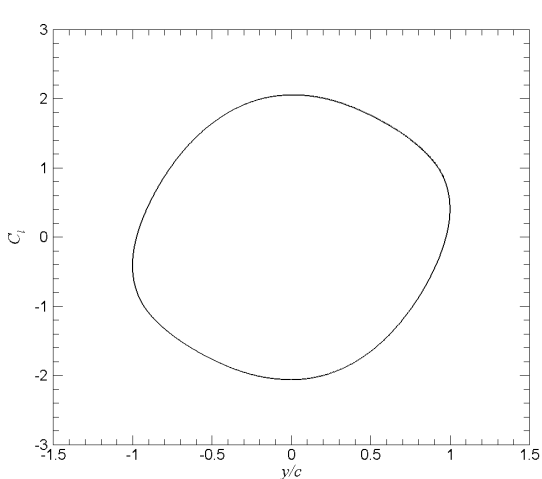


FIG. 4 (a): COEFFICIENT OF LIFT VERSUS HEAVE DISTANCE

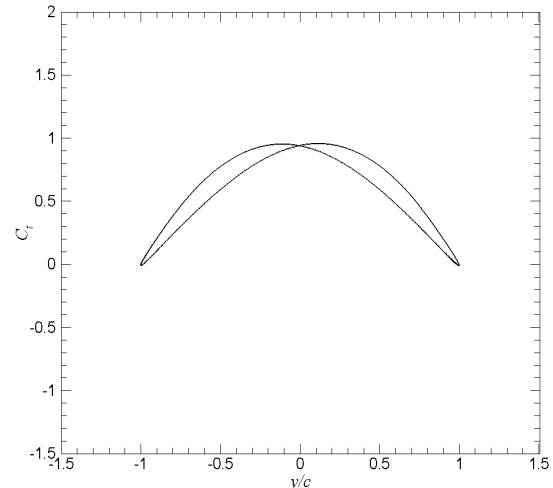


FIG. 4 (b): COEFFICIENT OF THRUST VERSUS HEAVE DISTANCE

The pressure fields of the wing section at 78% of span are shown in Fig. 5 for eight different instants of time while undergoing flapping motion. During downward motion, the pressure at upper surface is higher near leading edge when it is at  $20^\circ$  angle of attack. And lower pressure is observed at  $0^\circ$  angle of attack and higher pressure at lower surface near leading edge when it reaches to  $-20^\circ$  angle of attack. During upward motion, the pressure at upper surface is higher near leading edge when it reaches to initial position. The corresponding vorticity field plots are shown in Fig. 6. In the lower surface the wing section, the vorticity shed from leading edge to trailing edge during downward motion, similar behaviour can be observed on the upper surface of the wing section during the cycle and at the end of the cycle, finally it settles to lower surface when it reaches to initial position. The surface pressure fields on the upper and the lower surface of the wing for the same case at  $k = 0.83$  are shown in Fig. 7 for eight different instants of time while undergoing flapping motion for the final converged cycle. The corresponding vorticity plots on the upper and lower surface of the wing for the same instants are plotted in Fig. 8. From these field plots the variation of pressure and vorticity on the lower and upper surface can be observed for the complete cycle. Though there is not much change near the root of the wing as moving towards the tip, there are lot of variations in the pressure and vorticity distribution is observed, it may be due to the flow separation.

The coefficient of lift and thrust versus the angle of attack for the final cycle are shown in the Figs. 9 (a) and 9 (b) for  $k = 1.0$ . Though the figures look similar to the one at  $k = 0.83$  shown in Figs. 3 (a) and 3 (b). There are many differences in the area under the curve, which finally give the values of thrust coefficient and the propulsive efficiency. The mean-thrust coefficient and propulsive efficiency obtained for several cases from  $k = 0.5$  to  $k = 1.0$  are listed in Table 1, for Mach number = 0.3, Reynolds number =  $1.0 \times 10^5$  and keeping other parameters constant (such as  $h_0 = 1.0$ ,  $\alpha_a = 20^\circ$ ,  $a = 1/2$ ,  $\varphi = 90^\circ$ ). From the values obtained, it can be observed that as the reduced frequency increases the thrust coefficient also increases and the propulsive efficiency decreases for range of reduced frequency values considered in the present computations.

This effect can also be seen from the Figs. 10 and 11. In general, with the increase of reduced frequency the thrust coefficient increases but the propulsion efficiency decreases. As the flow becomes more and more unsteady with increasing reduced frequency, a large amount of vorticity is shed from the trailing edge, the thrust increases but the propulsive efficiency decreases.

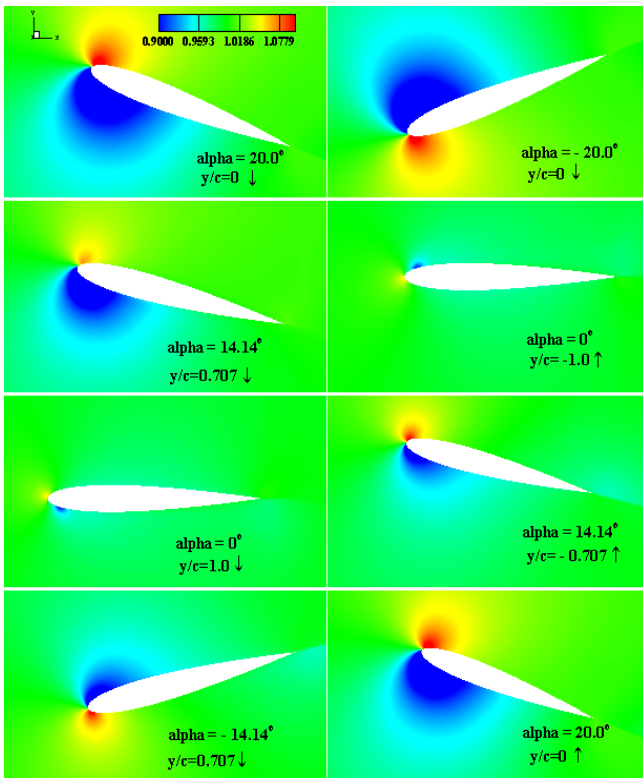


FIG. 5: PRESSURE FIELDS FOR A FLAPPING NACA 0012 WING AT DIFFERENT INSTANT OF TIME AT  $k = 0.83$  AND  $z/s = 0.78$

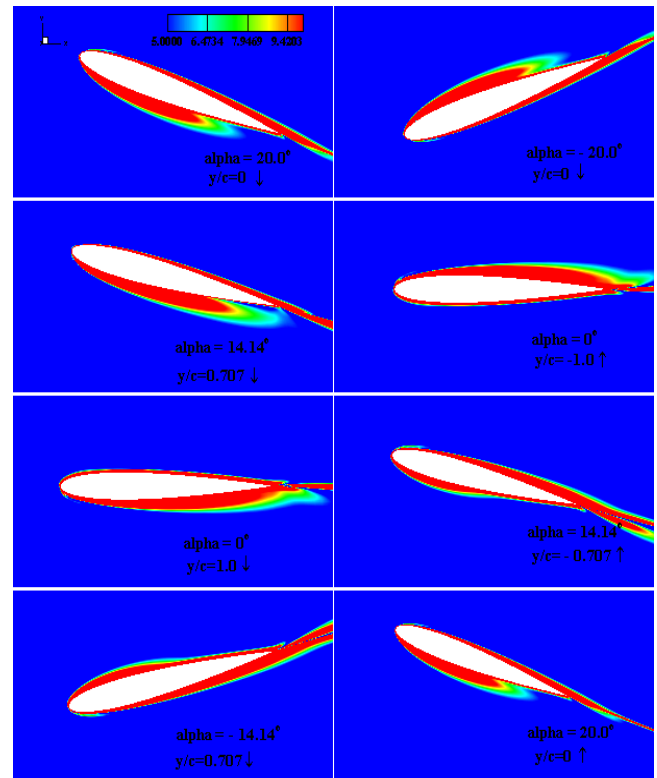


FIG. 6: VORTICITY FIELDS FOR A FLAPPING NACA 0012 WING AT DIFFERENT INSTANT OF TIME AT  $k = 0.83$  AND  $z/s = 0.78$

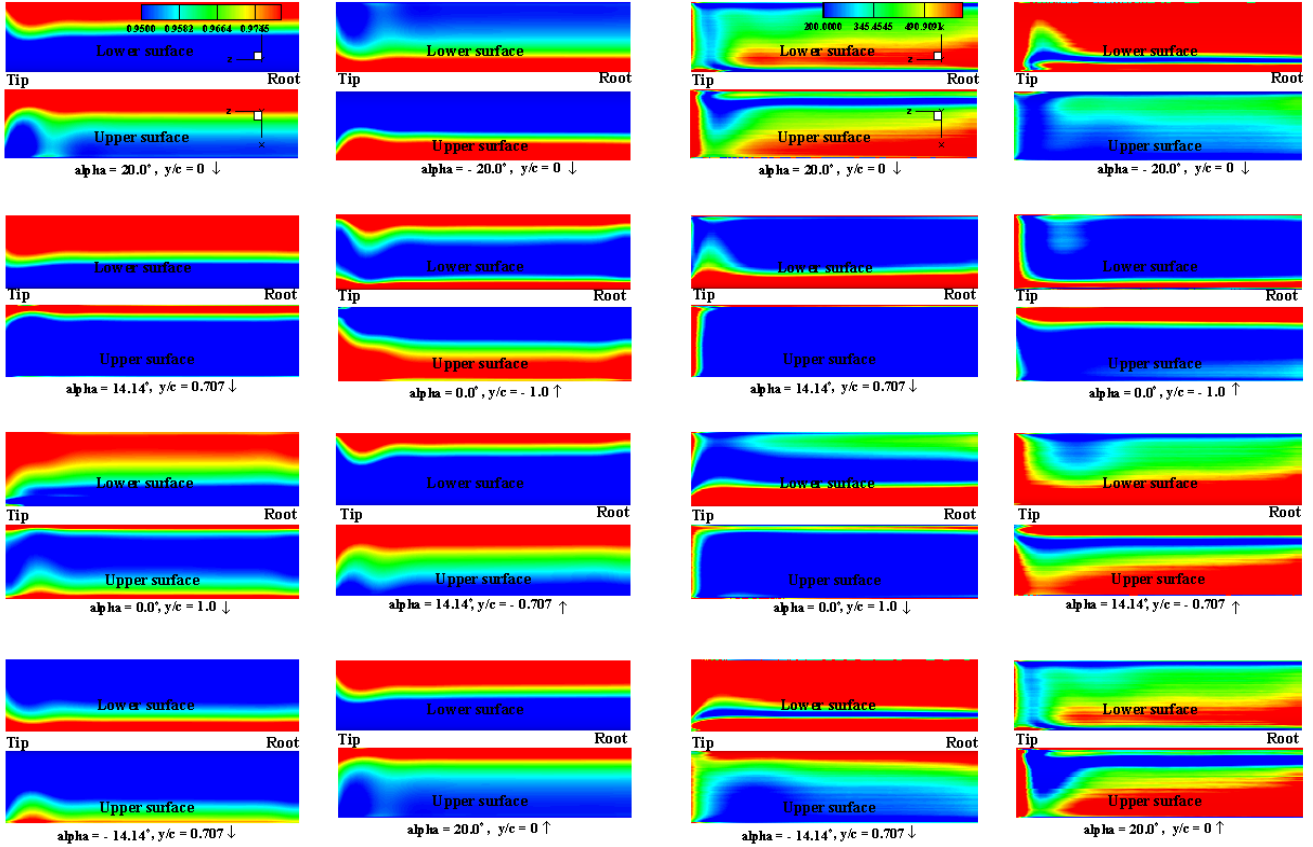
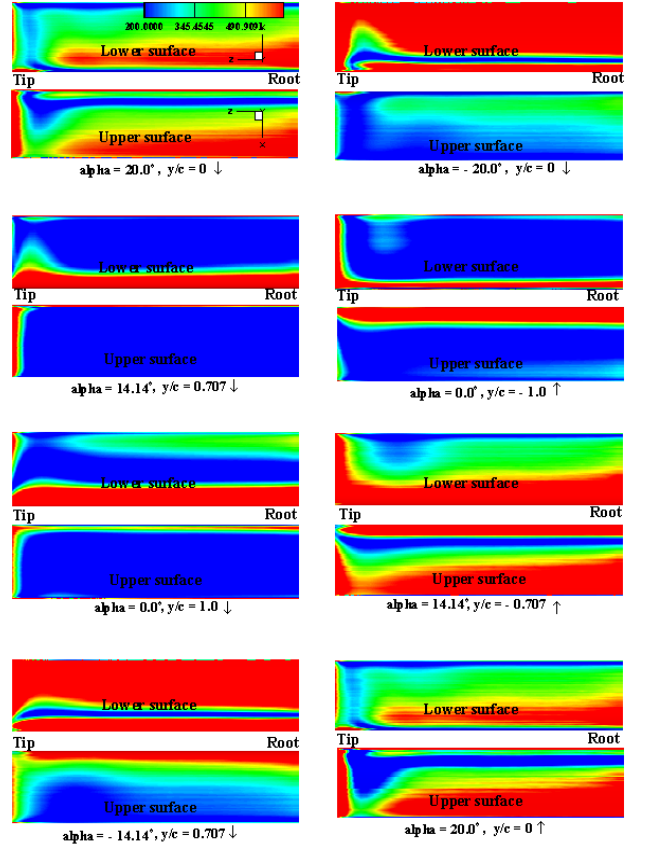
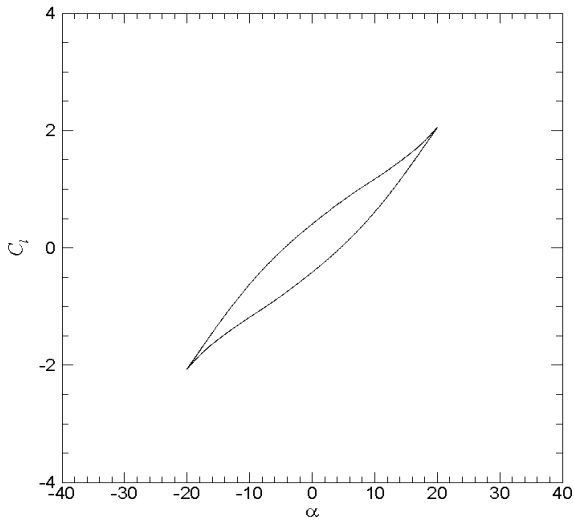

 FIG. 7: PRESSURE FIELDS ON LOWER AND UPPER SURFACE OF THE WING AT DIFFERENT INSTANT OF TIME AT  $k=0.83$ 

 FIG. 8: VORTICITY FIELDS ON LOWER AND UPPER SURFACE OF THE WING AT DIFFERENT INSTANT OF TIME AT  $k=0.83$ 


FIG. 9(a): COEFFICIENT OF LIFT VERSUS ANGLE OF ATTACK FOR THE FINAL CYCLE

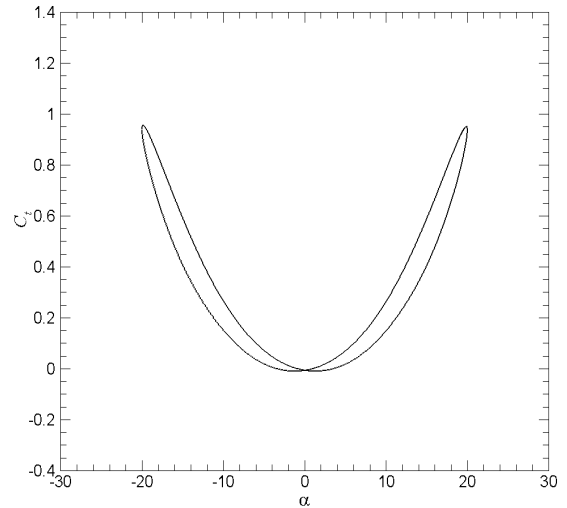


FIG. 9 (b): COEFFICIENT OF THRUST VERSUS ANGLE OF ATTACK FOR THE FINAL CYCLE

 TABLE 1: COMPUTED THRUST AND PROPULSIVE EFFICIENCY AT DIFFERENT  $k$  VALUES

Reduced Frequency, $k$	Mean-thrust coefficient, $C_t$	% Propulsive efficiency, $\eta_{Prop}$
0.5	0.14076403	60.435814
0.7	0.28639600	58.953339
0.83	0.45177373	55.293947
1.0	0.50836027	39.588696

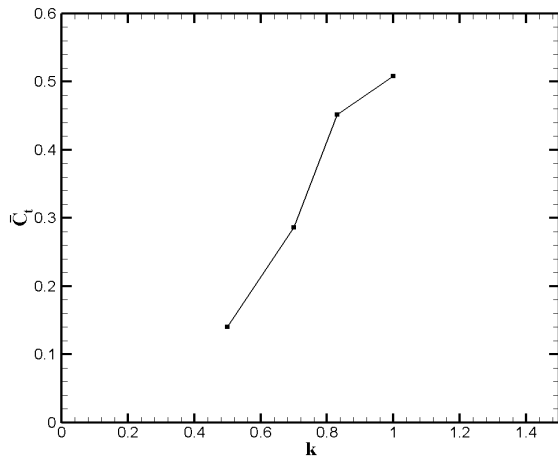


FIG. 10: MEAN-THRUST COEFFICIENT VERSUS REDUCED FREQUENCY FOR FLAPPING WING

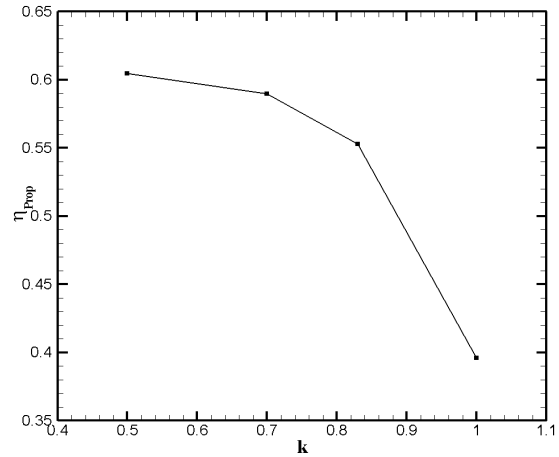


FIG. 11: PROPULSION EFFICIENCY VERSUS REDUCED FREQUENCY FOR FLAPPING WING

## Conclusions

The three-dimensional unsteady viscous flow over a combined pitching and heaving rectangular wing has been computed using an implicit RANS solver IMPRANS. The effect of reduced frequency on the time-averaged thrust coefficient and propulsive efficiency has been studied. From the results it is observed that, as reduced frequency increases, the time-averaged thrust coefficient increases and propulsion efficiency decreases for the range of values considered in the present computations. In all the cases, higher thrust occurred at higher reduced frequency, while higher propulsive efficiency occurred at lower reduced frequency.

## REFERENCES

- [1] Wei Shyy, Mats Berg and Daniel Ljungqvist, "Flapping and wings for biological and micro air vehicles", Progress in aerospace sciences, Vol. 35, Issue 5, pp. 455 - 505, 1999.
- [2] Trizila P., Kang C. K., Aono H, Shyy W., Visbal M., "Low-Reynolds number aerodynamics of a flapping rigid flat plate", AIAA Journal Vol. 49, No. 4, 806 - 823, 2011.
- [3] Wei Shyy, Hikaru Aono, Satish Kumar Chimakurthi, Trizila P., Kang C. K., Carlos E. S. Cesnik and Hao Liu, "Recent progress in flapping wing aerodynamics and aeroelasticity", Progress in Aerospace Sciences, Vol. 46, Issue 7, pp. 284 - 327, 2010.
- [4] Christopher T. Orłowski and Anouck R. Girard, "Dynamics, stability, and control analyses of flapping wing micro-air vehicles", Progress in Aerospace Sciences, Vol. 51, pp. 18 - 30, 2012.
- [5] Alessandro De Rosis, Falcucci G., Ubertini S and Ubertini F., "Aeroelastic study of flexible flapping wings by a coupled lattice Boltzmann-finite element approach with immersed boundary method", Journal of Fluids and Structures, Vol. 49, pp. 516 - 533, 2014.
- [6] Pines D and Bohorquez F., "Challenges Facing Future Micro-Air-Vehicle Development", Journal of Aircraft, Vol. 43, No. 2, pp. 290 - 305, 2006.
- [7] Ashraf M. A., Lai J. C. S and Young J., "Numerical Analysis of Flapping Wing Aerodynamics", 16<sup>th</sup> Australasian Fluid Mechanics Conference Crown Plaza, Gold Coast, Australia, pp.1283-1290, December 2<sup>nd</sup> - 7<sup>th</sup>, 2007.
- [8] Tatjana Y. Hubel and Cameron Tropea, "Experimental investigation of a flapping wing model", Exp. Fluids, Vol. 46, pp. 945 - 961, 2009.
- [9] Zaem A. Khan and Sunil K. Agrawal, "Force and Moment Characterization of Flapping Wings for Micro Air Vehicle Application", American Control Conference. Portland, OR, USA, pp. 1515 - 1520, June 8<sup>th</sup> - 10<sup>th</sup>, 2005.
- [10] Kamali R and Rezaei Ravesh S., "Numerical Analysis of MAV's Flapping Wings in Unsteady Conditions", JAST, Vol. 5, No. 1 pp. 1- 11, Iranian Aerospace Society, 2008.

- [11] Dutta P. K., Vimala Dutta and Sharanappa, "An Implicit RANS Solver for Unsteady Compressible Flow Computations", Proc. Seminar on State of the Art and Future Trends of CFD at NAL, NAL SP 0301, NAL, Bangalore, 2003.
- [12] Vimala Dutta, Sharanappa and Dutta P. K., "Navier-Stokes Computations for a Helicopter Rotor Blade in Hover", Proc. 8<sup>th</sup> Annual CFD Symposium, CFD Division of Aeronautical Society of India, Bangalore, August 11<sup>th</sup> - 13<sup>th</sup>, CP 18, 2005.
- [13] Sharanappa, Vimala Dutta and Dutta P. K., "Viscous Unsteady Flow around a Helicopter Rotor Blade in Forward Flight". Proc. 9<sup>th</sup> Annual CFD Symposium, CFD Division of Aeronautical Society of India, Bangalore, August 11<sup>th</sup> - 12<sup>th</sup>, CP13, 2006.
- [14] Dutta P. K., Vimala Dutta and Sharanappa, "RANS Computation of Flow past Wind Turbine Blades", Proc. 7<sup>th</sup> Asian Computational Fluid Dynamics Conference (ACFD7), Bangalore, November 26<sup>th</sup> - 30<sup>th</sup>, Paper 8.1, pp. 335- 353, 2007.
- [15] Pulliam T. H., "Implicit Solution Methods in Computational Fluid Dynamics", App. Num. Math., (Trans. IMACS), 2, 6, pp. 441 - 474, 1986.
- [16] Baldwin B. S. and Lomax H., "Thin Layer Approximation and Algebraic Model for Separated Turbulent Flows", AIAA Paper No. 78 - 257, 1978.
- [17] Sharanappa V. Sajjan, Vimala Dutta and Dutta P. K., "Numerical Simulation of flow over pitching bodies using an implicit Reynolds-averaged Navier-Stokes solver", Proc. of 12<sup>th</sup> Asian congress of Fluid Mechanics, Daejeon, Korea, August 18<sup>th</sup> - 21<sup>st</sup>, 2008.
- [18] Siva Kumar K and Sharanappa V. Sajjan, "Computation of Unsteady Flow over a Plunging Aerofoil Using an Implicit Reynolds averaged Navier-Stokes Solver", Proceedings of The 8<sup>th</sup> Asian Computational Fluid Dynamics Conference (ACFD8), Hong Kong, January 10<sup>th</sup> - 14<sup>th</sup>, 2010.
- [19] Siva Kumar K and Sharanappa V. Sajjan, "Three-dimensional Unsteady Flow over a Heaving Rectangular Wing", Frontier in Aerospace Engineering, Vol. 2. Issue 3, pp. 199 - 206, 2013.
- [20] Siva Kumar K and Sharanappa V. Sajjan, "Unsteady Flow past a Combined Pitching and Plunging Aerofoil using an Implicit RANS Solver", Applied Mechanics and Materials, Vols. 110 - 116, pp 3481- 3488, 2012.
- [21] Sharanappa V. Sajjan and Siva Kumar K., "Effect of Various Parameters on the Flapping Motion of an Aerofoil", Frontier in Aerospace Engineering, Vol. 2. Issue 2, pp. 129 - 135, 2013.

# Study of a Gossamer Sail and Its Application to LEO Spacecraft for Space Debris Mitigation and Attitude Control

Chan Ham\*<sup>1</sup> and Kuo-Chi Lin<sup>2</sup>

Mechatronics Engineering, Kennesaw State University, Kennesaw, GA 30144, USA / Mechanical and Aerospace Engineering, University of Central Florida, Orlando, FL 32816, USA

\*[cham4@kennesaw.edu](mailto:cham4@kennesaw.edu); <sup>2</sup>[kurt.lin@ucf.edu](mailto:kurt.lin@ucf.edu)

Received: April 23, 2015; Sent for review: April 27, 2015; Accepted: September 23, 2015

## Abstract

It presents the study of a novel space system for Low-Earth-Orbit (LEO) satellites developed as the experimental payload of the satellite for the U.S. Air Force Research Lab's University Nanosatellite Program. The proposed system is equipped with an inflatable magnetic sail, *magsail*, that provides an innovative navigation and control mechanization for a LEO spacecraft. It utilizes the magsail's aerodynamic force for the orbit transferring and magnetic torque for the attitude control. The proposed gossamer technology is an attractive technical solution for LEO satellites because of the extremely lightweight and minimal stowage volume. Finally, it presents the application study of the proposed system to a space debris mitigation and a satellite attitude control.

## Keywords

*Gossamer Sail; LEO Spacecraft; Space Debris; Attitude Control*

## Introduction

There have been several space missions to demonstrate solar sail technologies for space debris mitigation. NASA's Nanosail-D deployed a small experimental solar sail, which has potential to develop into an aerobraking system [1]. The CanX-7 mission focused on the validation of a drag sail as a deorbit device for nano- and micro-satellites [2]. However, all systems are solely based on aerodynamic drag forces with an inflatable structure.

The magnetic sail is a deployable gossamer structure with an imprinted torque coil. The conceptual satellite is illustrated in Figure 1. It aims to develop a novel technical solution for both attitude control and orbit maneuvering of LEO satellites, utilizing a state-of-the-art gossamer structure. The main advantage is the development of reliable, low-cost, and enabling technologies for LEO satellites that would considerably extend the performance envelope of an existing satellite's capability.

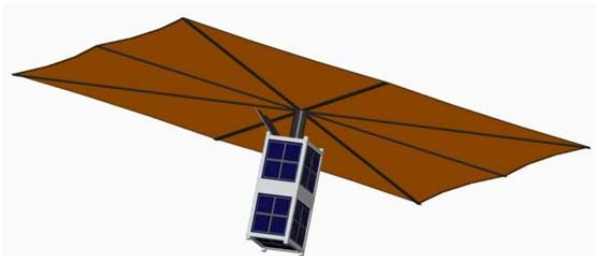


FIG.1 CONCEPTUAL DRAWING OF A SATELLITE WITH A MAGNETIC SAIL [3]

The magsail system was developed as the experimental payload of the satellite project as part of the Air Force Research Lab's University Nanosatellite Program (UNP). The UNP provides the opportunity for university faculty and student to work with professionals in the space society on a satellite development while competing for a launch opportunity. The program is required to design all the spacecraft subsystems from determining system requirement to delivering functioning prototypes.

The magsail will be able to generate torque on the satellite using electrodynamic interactions with the Earth's magnetic field according to the equation  $T = M \times B$  where  $T$  is the torque exerted by the coil,  $M$  is the magnetic dipole moment of the coil, and  $B$  is the magnetic field vector of the Earth. Since the earth's magnetic field's intensity is proportional to the inverse of  $R^3$  where  $R$  is the distance measured from the center of the earth, the magnetic force can be used for LEO satellites in achieving moderately fast attitude controls.

The magsail concept revolves around the idea of a large area gossamer sail, deployed from a much smaller stowed configuration. This magsail would be augmented beyond current solar sail designs through the inclusion of a large coil of magnet wire at the outside perimeter of the sail. By supplying power to the coil, a relatively large magnetic moment could be created to aid in the attitude control of the spacecraft.

In addition, the magsail will assist in orbit changing by increasing drag on the satellite due to the dramatic decrease in the ballistic coefficient of the satellite when the magsail is deployed. The aerodynamic drag is given by

$$D = \frac{1}{2} \rho V^2 C_D A$$

where  $\rho$  is the atmospheric density,  $V$  is the velocity of the satellite,  $C_D$  is the drag coefficient of the satellite, and  $A$  is the cross-sectional area of the satellite. It is clear from this equation that an increase in the cross-sectional area will lead to an increase in the aerodynamic drag.

The magsail greatly improves existing satellite attitude and orbit maneuvering technologies, providing greater torque than a torque rod of the same volume, mass, and power, while at the same time providing orbit-lowering capabilities.

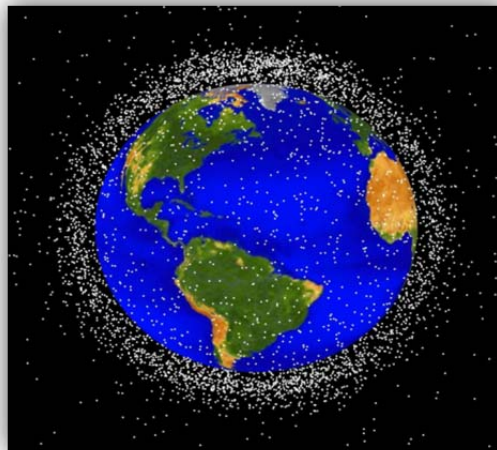


FIG.2 A SIMULATION SHOWING THE LARGER DEBRIS IN LEO. (NASA ORBITAL DEBRIS OFFICE)

Space debris consists of artificial objects that remain in orbit while not serving any use. The concern of space debris is growing. As shown in Figure 2, there are over 19,000 objects greater than 10 centimeters in diameter and many hundreds of thousands of smaller objects currently being tracked by U.S. Space Surveillance Network. These objects are threatening both commercial and scientific spacecraft. On February 10, 2009, destruction of the Iridium 33 communications satellite by collision with the disabled Russian Kosmos-2251 generated over two thousand pieces of new debris. This was the first time in history in which two satellites accidentally collided with each other and produced hundreds of pieces of space debris that continue to pose a threat to other spacecraft [4]. It forced the International Space Station to run a collision avoidance maneuvering.

Dead satellites, rocket stages, and fragments from spacecraft explosions or collisions all contribute to the population of space debris. All of these objects have the potential to collide with and critically damage operational spacecraft. Much of the debris will remain in orbit for hundreds of years, posing a long-term threat to current and future space missions [5].

In light of these events, the orbital debris mitigation policy has been agreed between international space agencies such as NASA, ESA, JAXA, ASI, BNSC, CNES, DLR, etc. One of the requirements is that all debris released during

a spacecraft's LEO mission shall be limited to a maximum orbital lifetime of twenty-five years [6, 7]. The rationale for such requirement is stated in the document as: *"The 25-year removal time from LEO limits the growth of the debris environment over the next 100 years while limiting the cost burden to programs and projects. The limit of 25 years has been thoroughly researched and has been accepted by the U.S. Government and the major space agencies of the world."*

Traditionally, large satellites have used an onboard propellant to maneuver in orbit and position themselves for removal. However, small satellites generally lack these means of maneuvering. This requirement has led to the development of propellantless orbital maneuvering systems suitable for smaller spacecraft. The least complex of these orbital maneuvering systems work by increasing the surface area of the spacecraft. This imparts more drag, reducing the velocity and increasing the rate of orbital decay.

Objects over 600 km are of the greatest concern, as their orbits may last longer than 25 years. Objects between 500 and 1000 km will likely be easier to bring out of orbit than to be pushed into a storage orbit. The magsail provides an inexpensive, lightweight, and efficient means to bring obsolete, damaged, or disabled spacecraft out of these orbits.

The magsail provides a drastic increase in cross-sectional area from a compact, lightweight storage system utilizing the unique folding and deployment of a gossamer sail. This system has been tested using sails as small as [2m x 2m] and as large as [20m x 20m], allowing it to be used on spacecraft of various sizes. The uniform deployment of the magsail, along with its perimeter magnetic torque coil will allow for stable flight and provide the potential for future development of propellantless multi-orbit missions. Simulation results show that the magsail system can reduce the orbit time of a spacecraft at 600km from 25 years to less than five months.

This paper details the design of the magsail to ensure the deorbiting of the satellite within 25 years and to utilize it as the attitude control including overviews of the support subsystems including the spacecraft structure. This is followed by a discussion of the simulations used to demonstrate the effectiveness of the magsail.

## Development of the Magsail and KnightSat II

The basic configuration of the magnetic sail consists of the booms, torque membrane, and release mechanism. The prototype magsail was developed by L'Garde. The deployed magsail has a square shape that is equivalent to one-axis magnetic torque coils. The sail system is implemented in the satellite bus that provides the electronics for membrane release and power to the torque coils on the membrane. Based on the baseline design, the required specifications, requirements, risk trades, configuration trades, and the list of all necessary elements such as equipment, components, and mass properties were defined. Then, relevant mission parameters and environments were utilized to refine the magsail design. Finally, the integrated magsail system fit within the satellite modular block were developed and the integrated ground prototype system were demonstrated.

### *Magsail System*

The magnetic sail consists of a coil shaped circuit imprinted upon a 10m<sup>2</sup> Kapton® film membrane. It was assured that the proposed ground prototype will achieve all of its objectives within the defined parameters, making it as close to a flight model as possible. The main performance characteristics for these gossamer structures are their packageability, structural stability and deployability. The estimated mass of the deployed membrane is to be roughly 0.5 kg, allowing an additional 1 kg for the deployment and support structure as well as the containment vessel for the flight unit.

Though some top-level trades on the deployment and support structure was conducted, the lightest way to proceed would be to use "carpenter tape" segments forming a cruciform from the center of the square membrane to its four corners with possible additional bracing that are connected with reinforced outskirts. The tape segments (longerons) are rolled along with the membrane to the center of the sail for stowage. Upon opening the containment vessel, the longerons will unroll to their initial "shape memory" configuration, deploying the membrane and supporting it for the life of the experiment.

As shown in Figure 3, the sail system consists of a square stowage box with four doors that open outward in order to permit the magsail deployment. The box contains an electronics package, pressure vessel, the sail, and booms.

The stowed dimensions of the box are 35 cm (L) x 35 cm (W) x 5 cm (H). The projected mass of the entire magsail system is expected to be less than 5 kg. The dimensions of the sail are represented in Figure 4.

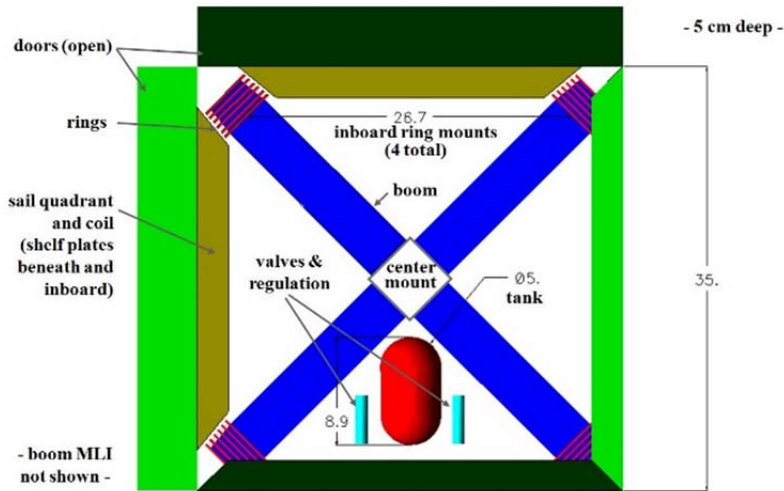


FIG.3 MAGSAIL STOWAGE BOX

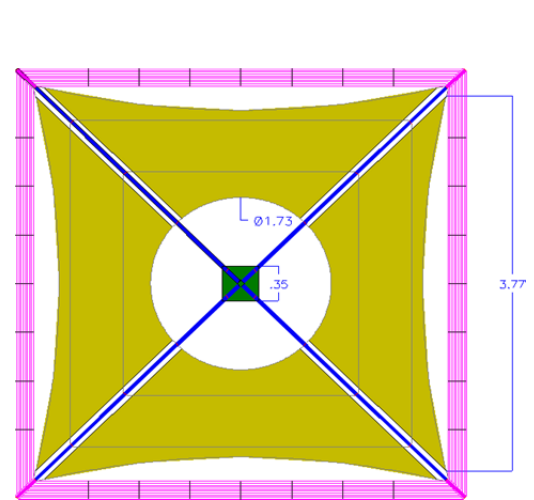


FIG.4 DEPLOYED MAGSAIL

Initiation of the deployment process may require a remote control mechanism. The deployed volume is estimated to be roughly  $2000\text{cm}^3 - 3000\text{cm}^3$ . Allowing for a packaging factor of 10, which would yield a very comfortable packaging environment for the membrane, the stowage volume would be  $200\text{cm}^3 - 300\text{cm}^3$ . The proposed magsail volume deployed is less than  $3000\text{cm}^3$ , which the augmented satellite size (effective area) is smaller than ordinary small satellites in low earth orbit. Therefore, the potential risk would not be more serious than other LEO small satellites.

The electronics control the sequence of deployment, and ensure that the booms deploy in a uniform manner. The pressure vessel provides nitrogen gas that inflates the booms. The magsail is stored in four segments, with each segment stored on one side of the box. The magsail segments are attached to four booms that are conically folded at each corner of the box. A schematic of a boom segment is shown in Figure 5.

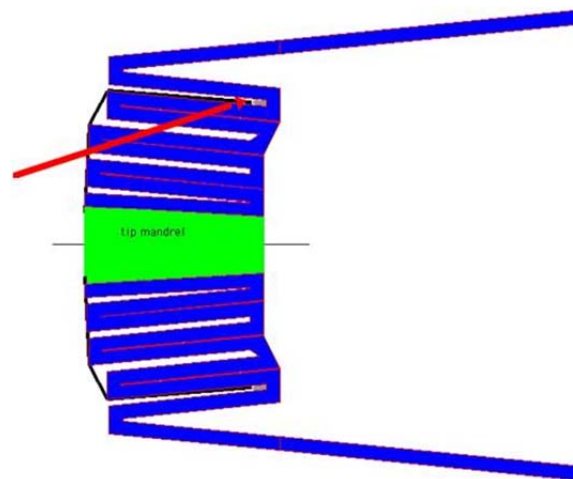


FIG.5 CONICAL FOLDING OF BOOM SEGMENT

Once deployed, the sail will have a cross-sectional area of  $10\text{m}^2$ . At the perimeter of the sail are ten turns of 30 AWG wire. The wire leads are laid down on the inside of the booms and run through the stowage box, where they interface with the satellite's power and command and data handling systems. These perimeter coils will provide magnetic attitude control once current is passed through them. By taking advantage of the large surface area provided by the sail, the coils will generate a significant amount of magnetic torque.

The magsail itself is made of  $7.62\mu\text{m}$  Kapton, which is 70% emissive. This emissivity is advantageous because it will allow for light to reach the satellite's solar panels. However, the power system design should consider the 30% emissivity loss in order to produce enough power for satellite's mission. In addition, worse radiation environment

at higher altitudes should also be considered for the power system development. The booms are made of Sub-Tg resin impregnated Vectran fabric, which is pliable when heated and rigid once cooled. Heaters will be used to prepare the boom segments for deployment and disabled when deployment is complete. The booms are painted in reflective coatings to prevent loss of rigidity once they have been deployed. Materials similar to this were flown and tested on the Cibola Flight Experiment in the form of deployable antennae [8].

The major concern with the magsail is premature deployment. To address this issue, the booms will be completely purged during the launch preparation. Not until the satellite has been released from the launch vehicle, charged, and capable of sending power to the magsail would the ascent valves be closed and deployment be possible. Electrical inhibits and redundant closed valves between the pressure vessel and the regulator supplying pressure to the booms provide additional mechanisms, preventing unwanted deployment.

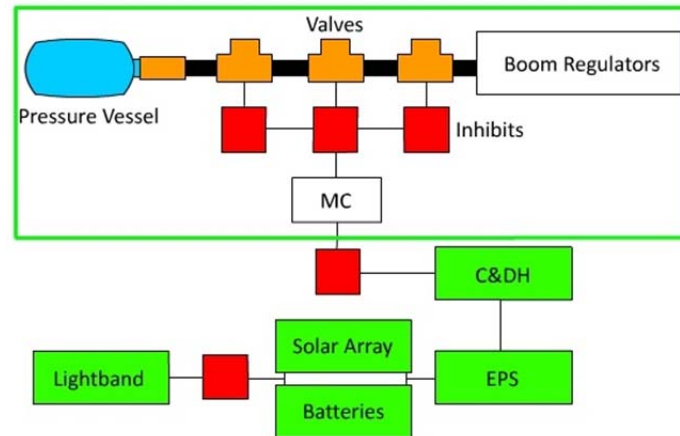


FIG.6 MAGSAIL FAULT TOLERANCE SYSTEM

In order to address the safety concern, the magsail utilized two fault tolerances for the entire system. The current concept for the fault tolerance system is presented in Figure 6. In the figure, MC stands for micro-controller, C&DH and EPS stand for command and data handling and electrical power system, respectively.

### Ground Prototype

Given factors such as cost, durability, and available deployment space, the system was simplified. The boom material was changed to 0.25 inch neoprene fabric so that it could be repeatedly deployed and repackaged. The sail material was changed to 0.03 inch aluminized Mylar film. The increased thickness of these materials required a larger stowage box to be used. The size of the sail was reduced to [2m x 2m] so that it could be deployed indoors.



FIG.7 MAGSAIL GROUND PROTOTYPE

The prototype deployment system shown in Figure 7 utilizes an external pressure system that is attached to a fitting at the center of the four booms. Upon inflation, the booms extend and drag the Mylar sail outward. Attached to the end of the booms are ten turns of 30 AWG wire separated by Kapton tape battens, similar to the ones that

will be utilized on the magsail. Despite the differences in construction, the ground prototype provides a suitable demonstration for the simplicity and reliability of the deployment system, as the booms and membrane are folded and deployed in the same way as the final magsail components will. This prototype has been deployed dozens of times for testing and demonstrations at the Flight Competition Review (FCR) at the U.S. Air Force.

### ***Supporting Mechanism and Bus Subsystems***

This development involves the supporting structure, computer board, software development, stowage bin, release mechanism, and power electronics. The limited size of the satellite modular block requires a different design approach from the traditional bus and subsystem based design. To maximize volume, mass, and power efficiency, the satellite is instead designed as a single integrated system.

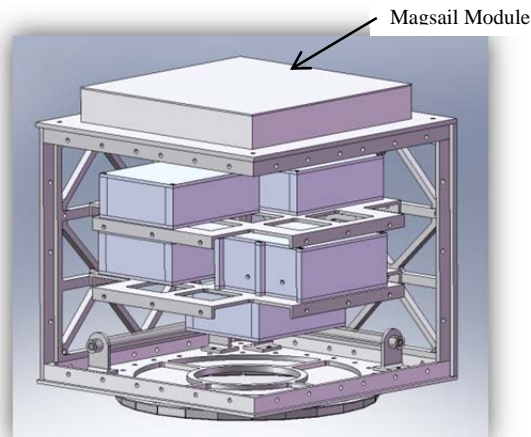


FIG.8 KIGHTSATII STRUCTURE CUTAWAY

As shown in Figure 8, the structure of KnightSat II was designed to be modular and easy to work with during assembly. That was accomplished by using a large isogrid pattern to allow ease of access to the internals, and the ability of the structure to support itself with multiple walls removed. The structure was composed of 6061 T6 Aluminum and chemical film coated. The requirements for the structure to withstand a 20G load in the  $x$ -,  $y$ -, and  $z$ -axis and have a fundamental frequency greater than 100 Hertz.

The basic design objective is to achieve the mission goals by developing the most efficient engineering design that is fully complied with most launch vehicles. In order for the technical reliability and space compliance, off-the-shelf satellite components are used as much as possible. Those products are already proven with space qualification heritage. Our own development would be the custom design of the deployable structure tray and the associated structure and mechanism.

Initial stabilization of the spacecraft prior to the deployment of magsail will be achieved by use of three EFI alloy 50 magnetic torque rods controlled by an RCM5700 processor and a 3DM-GX1 Inertial Motion Unit (IMU). Data from the IMU will be relayed to the primary flight computer for compression and transmission to the ground.

### ***Sail Performance***

Preliminary simulations suggest that a sail of the parameters mentioned above could provide a magnetic dipole moment of about  $60 \text{ A}\cdot\text{m}^2$ . This simulation is for the sail at room temperature. In the space environment, it could be much greater due to cooling of the circuitry in space. This is on par with or better than many commercially available torque rods. The performance of the sail for orbit lowering is hard to characterize without considering the nature of the orbit, but it is expected that the sail would lower the ballistic coefficient of the satellite by a factor of roughly 250. Theoretically, this would lead to an increase in deceleration due to aerodynamic drag by the same factor.

### ***Risks and Mitigation***

There are two technical implementation issues on the magsail especially for extremely small satellites. One is the deployment issue and the other is the mechanical loading to the integrated satellite. The main risk is excessive

deployment speed due to the stored energy in the rolled longerons. At very high deployment speeds, the membrane could be damaged. However, based on previous spaceflight experiments, membrane structures of similar size were deployed at the speed range of 80-100[ms] without any damage. Nonetheless, the membrane should be reinforced, either at the edge or at regular intervals over its area using Kevlar or Vectran twine and/or tape.

The overall efficiency of the sail may be affected by the surface wrinkles, flexibility, and deformations in sail shape that also may be crucial to the controllability of the sail. It requires an extensive simulations on the mechanical properties and dynamic characteristics of the integrated satellite. Though at this time the membrane rigidization of the ground prototype may not provide any advantage, the result would determine the necessity of the rigidization of the spaceflight model. The rigidizable material that has flown in space is L'Garde's cold rigidizable (Sub- $T_g$ ) material, which would require multilayer insulation to keep it rigid in thermal environments, such as solar irradiation and the earth's albedo at LEO, thus pushing the stowage volume and mass even higher.

### Application to Space Debris Mitigation

The Debris Assessment Software (DAS) developed by NASA was used to perform the debris assessments for the satellite. These assessments included deorbit simulations and the probability of collisions with objects while in orbit. DAS is intended to ensure that the space mission conforms to the requirements specified in the NASA Technical Standard 8719.14. The DAS uses the propagators PROP3D and GEOPROP, which are used by NASA's debris environment evolutionary models [9].

The force models include Earth's atmosphere and gravitational field, solar and lunar gravitation, and solar radiation pressure. Values for the solar flux are used in the atmospheric calculations, and are based on NOAA short-term predications and NASA long-term predictions. The DAS was used to find the highest orbital altitude which the satellite could be placed in while still deorbiting within twenty-five years. After numerous simulations were run, this altitude was found to be about 580 kilometers. A plot of the satellite's altitude history is shown in Figure 9. It found that in 580 kilometer circular orbit, the satellite would take about 25 years to deorbit. If the satellite were any higher than this, it would take longer than 25 years to deorbit.

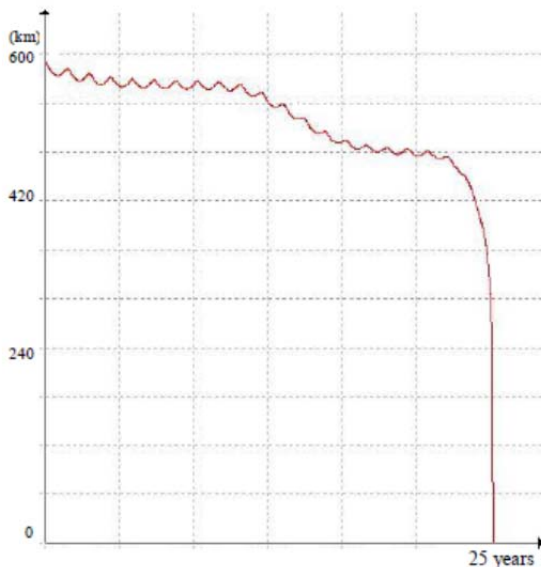


FIG.9 SATELLITE ORBITAL LIFETIME WITHOUT SAIL

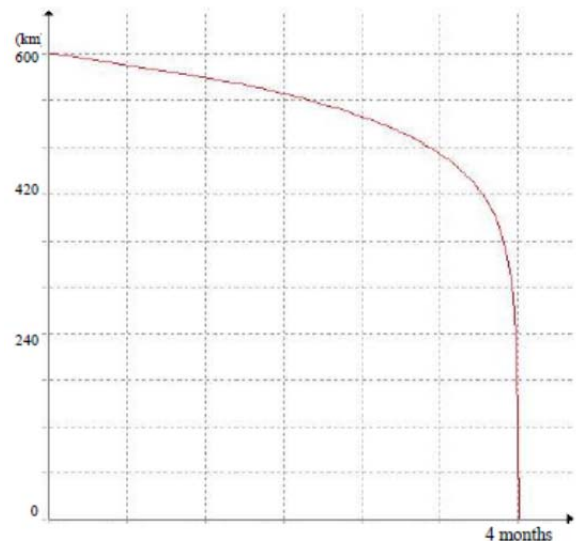


FIG.10 SATELLITE ORBITAL LIFETIME WITH MAGSAIL

A DAS simulation was then conducted for the satellite with the fully-deployed magsail. This simulation showed a significant reduction in the orbital lifetime. As the result shown in Figure 10, the satellite can be completely deorbited within 4 months. The simulation result shows a dramatic improvement resulted from the magsail utilization. Since the magsail enables the satellite to deorbit in such a short amount of time, the satellite can be placed in a much higher orbit where the drag will cause it to deorbit within 25 years. The new operational ceiling of the satellite is shown in Figure 11. It shows that with the magsail deployed, the satellite would take about 25

years to deorbit from an altitude of 900 kilometers. This could be advantageous for satellites whose missions seek to take advantage of higher altitudes.

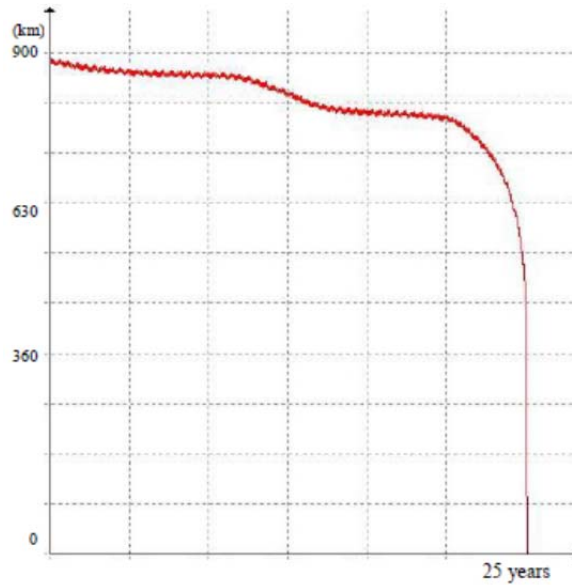


FIG.11 SATELLITE ORBITAL LIFETIME WITH THE MAGSAIL STARTING FROM 900KM ALTITUDE

These simulations showed promising results, in that the magsail produced a significant enough drag force to reduce the orbit time by a large margin. It shows the spacecraft's possible operating altitude ceiling can be increased from 600km limit to 900km. The effects are significant enough to justify the large increase of cross-sectional area when the sail is deployed.

#### Application to Satellite Attitude Control

The magsail is also envisioned as providing an integral aspect of the attitude control system. The perimeter of the sail will be laced with ten turns of magnetic coils, which, combined with two magnetic torque rods located within the satellite, will provide magnetic attitude control. The magsail's application to an attitude control was investigated since the application concept may provide a clear benefit to a small LEO satellite. The potential advantage of the magsail for the attitude control is the utilization of a large sail area since the magnitude of a magnetic torque is proportional to the loop area covered by coils. The relatively large magnetic moment could be utilized to configure the total attitude control system in addition to magnetic torque rods implemented inside of the satellite. As a result, the magnetic torque generated by large surface area of the sail can extend the limited size of a small satellite.

Once deployed, the magsail will act like a shuttlecock, shifting the satellite's center of pressure to the center of the magsail. This will help stabilize the satellite after the magsail is fully deployed from the satellite. The magsail is constrained for the attitude control for altitudes below 600 km unless the mission life of the satellite is less than 4 months. However, it may be utilized as a supplementary attitude control system for altitudes higher than 600km.

The attitude of the satellite using the system would consist of active control from the magsail as well as two small torque rods, as well as passive stabilization about the pitch and roll axes from the gravity gradient effect of the sail. The satellite is modeled as a 50 cm x 50 cm x 50 cm cube with a mass of 47.5 kg, with a 3m x 3m flat plate of infinitesimal width and with a mass of 2 kg attached to one side.

Major disturbance sources are atmospheric drag and from the restoring force of the sail. Both of these torques can be modeled as the cross product of the offset vector (the distance of the point acted on by the disturbing force from the center of gravity) and the disturbing force. In the case of the atmospheric drag, the force can be modeled as a point force acting on the center of the sail, giving us an offset vector of:

$$\boldsymbol{\gamma} = \begin{bmatrix} \gamma_x \\ \gamma_y \\ \gamma_z \end{bmatrix} = \begin{bmatrix} \mathbf{0} \\ \mathbf{0} \\ 0.25 \end{bmatrix} \mathbf{m},$$

assuming that the center of gravity is coincident with the center of the cube where  $x$ ,  $y$ , and  $z$  are positions in the satellite body frame. The force itself can be found by multiplying the previously mentioned drag acceleration formula by the mass of the satellite.

$$\vec{F}_{drag} = \frac{1}{2} \rho c_D A v_{rel}^2 \frac{\vec{v}_{rel}}{|\vec{v}_{rel}|},$$

where  $\rho$  is atmospheric density [kg/m<sup>3</sup>],  $c_D$  is drag coefficient,  $A$  is cross sectional surface area [m<sup>2</sup>], and  $v_{rel}$  is velocity relative to atmosphere [m/s].

This drag acts along the negative velocity vector, so, using the small angle approximation, the vector can be expressed as:

$$\vec{F}_{drag} = \begin{bmatrix} -F_{drag} \\ \psi F_{drag} \\ -\theta F_{drag} \end{bmatrix},$$

from which the atmospheric disturbance torque can be derived as

$$\vec{\tau}_{DA} = \gamma \times \vec{F}_{drag} = \begin{bmatrix} -(\gamma_y \theta + \gamma_z \psi) F_{drag} \\ -(\gamma_z - \gamma_x \theta) F_{drag} \\ (\gamma_y + \gamma_x \psi) F_{drag} \end{bmatrix} = \begin{bmatrix} 0 \\ \gamma_x \theta F_{drag} \\ \gamma_x \psi F_{drag} \end{bmatrix},$$

where  $\theta$  and  $\psi$  are the roll- and yaw-angle [rad], respectively.

Firstly, the magnitude of the disturbing force should be found. Assuming that the sail is hanging perfectly in the vertical direction, the tension in the sail can be expressed as [10]:

$$F_{GG} \approx 3Lm\omega_0^2,$$

where  $m$  is the mass above the center of mass of the satellite end-mass system,  $L$  is the length from the satellite to the center of mass, and  $\omega_0$  is the orbital velocity. This length can be approximated as:

$$L = \frac{\sum m_i r_i}{\sum m_i} = \frac{0 + .5(1000)}{50} = 10m,$$

where  $m = 49.5$  kg (the mass of the system without the end-mass). The force acts in the Nadir direction, so, again using the small angle approximation, the force vector can be expressed as:

$$\vec{F}_{GG} = \begin{bmatrix} -\theta F_{GG} \\ \phi F_{GG} \\ F_{GG} \end{bmatrix},$$

where  $\phi$  is the pitch angle [rad].

Then, the disturbance torque is given by

$$\vec{\tau}_{DGG} = \gamma \times \vec{F}_{GG} = \begin{bmatrix} (\gamma_y - \gamma_z \phi) F_{GG} \\ -(\gamma_z \theta + \gamma_x) F_{GG} \\ (\gamma_x \phi + \gamma_y \theta) F_{GG} \end{bmatrix} = \begin{bmatrix} -\gamma_z \phi F_{GG} \\ -\gamma_z \theta F_{GG} \\ 0 \end{bmatrix}.$$

A PD controller can be used to control the attitude of the satellite by the control torques [11]:

$$\begin{aligned} m_x &= K_{PX} \phi + K_{DX} \dot{\phi} \\ m_y &= K_{PY} \theta + K_{DY} \dot{\theta} \\ m_z &= K_{PZ} \psi + K_{DZ} \dot{\psi} \end{aligned}$$

where  $K_P$  and  $K_D$  are proportional- and derivative-control gain, respectively.

These torques are not always attainable, depending upon the orientation of the Earth's magnetic field relative to the satellite body axis. The actual torques exerted by the magnetic torquers are approximated by the equation [11]:

$$\vec{\tau}_c \cong \frac{L(\vec{B}^0) \cdot \vec{m}}{|\vec{B}^0|},$$

where  $\vec{B}^0$  is the magnetic field vector in the orbital frame and  $L(\vec{B}^0)$  is the matrix:

$$\begin{bmatrix} -((B_y^0)^2 + (B_z^0)^2) & B_x^0 B_y^0 & B_x^0 B_z^0 \\ B_y^0 B_x^0 & -((B_x^0)^2 + (B_z^0)^2) & B_y^0 B_z^0 \\ B_z^0 B_x^0 & B_z^0 B_y^0 & -((B_x^0)^2 + (B_y^0)^2) \end{bmatrix}$$

The 3-DOF rotational equation of motion for the chosen Euler angle rotation can be expressed as:

$$\begin{aligned} I_x \ddot{\phi} + 4\omega_0^2(I_y - I_z)\phi - (I_x - I_y + I_z)\omega_0 \dot{\psi} &= T_{CX} + T_{DX} \\ I_y \ddot{\theta} + 3\omega_0^2(I_x - I_z)\theta &= T_{CY} + T_{DY} \\ I_x \ddot{\psi} + \omega_0^2(I_y - I_x)\psi + (I_x - I_y + I_z)\omega_0 \dot{\phi} &= T_{CX} + T_{DX} \end{aligned}$$

These dynamic formulas can be used to create a dynamic simulation of the satellite's attitude, using numerical integration. The main obstacle to design a control is the time-variant nature of the  $B^0$  field. To circumvent this issue, the orbital averages of these values are used instead when determining the roots of the system for stability purposes [11].

Simulations were conducted to output the performance of the torque coil for a large variety of design conditions, to demonstrate how changes in various design parameters effect performance. Power is perhaps the easiest of the variables to analyze, since it is not related to the structure, and, as such, involves no trade-offs with other design elements. The magnetic moment of the coil is proportional to the square root of the power.

In the simulation, the NRLMSISE-00 Atmosphere Model was used to determine the value of the atmospheric density, and the World Magnetic Model was used to determine the magnitude of the Earth's magnetic field. The simulation used a quaternion representation of 6 degrees-of-freedom equations of motion with respect to the satellite's body axis.

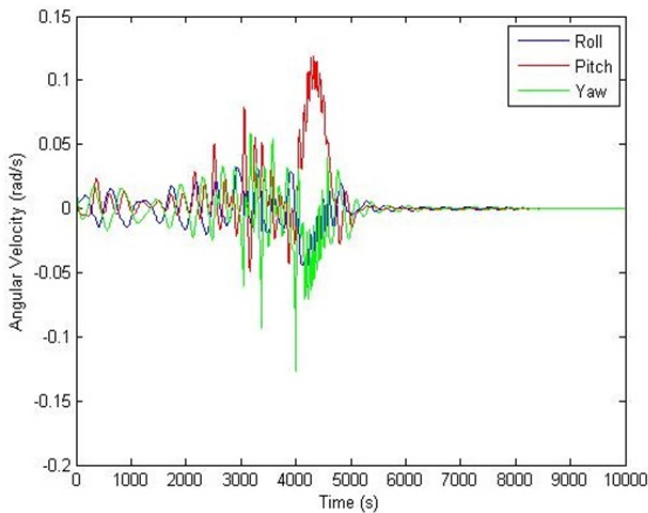


FIG.12 SATELLITE ORIENTATION

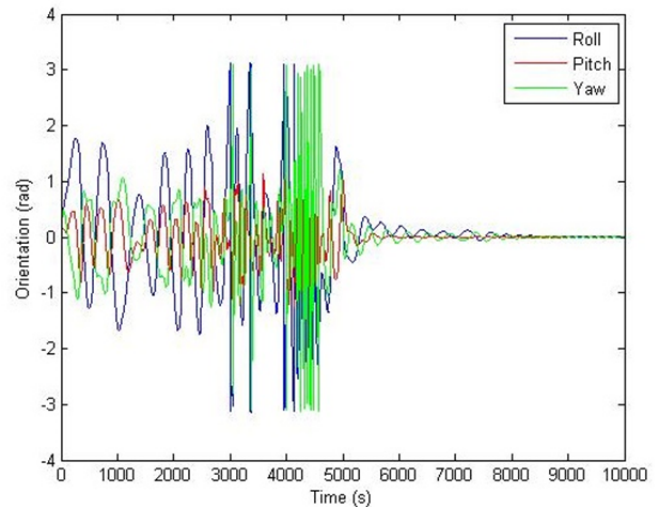


FIG.13 ANGULAR VELOCITIES OF THE SATELLITE ATTITUDE

As shown in Figure 12 and 13, simulation results show that it would take about two hours for the satellite to stabilize. For a mission that may require rapid reorientation and stabilization, this may not be the system of choice. But for a mission where rapid attitude control is not required, this system is very effective.

## Conclusions

This study focused on the top level research and design concept work for the magsail. The proposed gossamer magsail offers an effective means by which to rapidly deorbit satellites at the end of their operational lifetimes, as well as raise their operational ceilings. This study also showed the effectiveness of the magsail as an attitude control system. The successful deployments of the ground prototype have proven the feasibility and effectiveness of the magsail deployment system.

## ACKNOWLEDGMENT

This research is sponsored by U.S. Air Force Office of Scientific Research under the 6th Air Force University Nanosatellite Program, Contract Number: FA95500910122.

## REFERENCES

- [1] Whorton M., Heaton A., Pinson R., Laue G., and Adams C., "NanoSail-D: The First Flight Demonstration of Solar Sails for Nanosatellites," *22<sup>nd</sup> Annual AIAA/USU Conference on Small Satellites*, SSC08-X-1, 2008.
- [2] Cotton B., Sears T., Hiemstra, J., Chung J., Bonin G., and Zee R., "The CanX-7 Nanosatellite Deorbit Mission: Demonstrating Sustainable Use of Low-Earth Orbit," *Small Satellite Systems and Services Symposium*, 2014.
- [3] Preliminary Design Report for the U.S. Air Force Office of Scientific Research's University Nanosatellite Program, Contract Number FA95500910122, University of Central Florida, 2009.
- [4] "Satellite Collision Leaves Significant Debris Clouds." *Orbital Debris Quarterly News*. Volume 13, Issue 2. April 2009.
- [5] "Chinese Ant-satellite Test Creates Most Severe Orbital Debris Cloud in History." *Orbital Debris Quarterly News*. Volume 11, Issue 2. April 2007.
- [6] "NASA Technical Standard 8719.14, Process for Limiting Orbital Debris." National Aeronautics and Space Administration, Washington, DC.
- [7] [http://www.esa.int/Our\\_Activities/Operations/Space\\_Debris/Mitigating\\_space\\_debris\\_generation](http://www.esa.int/Our_Activities/Operations/Space_Debris/Mitigating_space_debris_generation)
- [8] Caffrey M., Keith M., Roussel-Dupre D., Robinson S., Nelson, Salazar A., Wirthlin M., Howes W., Richins D. "On-Orbit Flight Results from the Reconfigurable Cibola Flight Experiment Satellite (CFESat)," *Proceedings of FCCM '09*, 2009
- [9] "Debris Assessment Software User's Guide, Version 2.0." Astromaterials Research and Exploration Science Directorate, Orbital Debris Program Office. November 2007.
- [10] Cosmo M. and Lorenzini E., "Tethers in space handbook," prepared for NASA Marshall Space Flight Center, Dec. 1997.
- [11] Martel F., Pal P., and Psiaki M., "Active magnetic control system for gravity gradient stabilized spacecraft," presented at the 2<sup>nd</sup> Annual AIAA/USU Conference on Small Satellites, Logan, UT, 1988.

**Dr. Chan Ham** is currently an Associate Professor of the Mechatronics Engineering Department at the Kennesaw State University. He served as the director of Space System Programs at NASA Florida Space Grant Consortium in 2009. He has also been involved in the development of diverse space systems such as spacecraft and Mars surface support equipment. His research projects were funded by NASA, US Air Force, and industries. His main research interests are developments of space and mechatronics systems.

**Dr. Kurt Lin** is currently an Associate Professor of Department of Mechanical and Aerospace Engineering at the University of Central Florida since in 1990. His major interest is mainly in the fields of renewable energy, rotating machinery, modeling and simulation, and small satellite.

# Limits of Stable Combustion in an Engine of Ultra-Small Spacecrafts

Kanysh O. Sabdenov\*<sup>1</sup>, Johann Dueck<sup>1,2</sup>

\*<sup>1</sup>L.N. Gumilyov Eurasian National University, Munaitpasov-Str. 5, 010008 Astana, Kazakhstan

<sup>2</sup>Friedrich-Alexander-University Erlangen-Nuremberg, Paul-Gordan-Str. 3, 91052 Erlangen, Germany

E-mail: sabdenobko@yandex.kz

Received: June 20, 2015; Sent for review: June 24, 2015; Accepted: November 18, 2015

## Abstract

Using the analytical and numerical methods, an analysis of low-frequency stability of combustion in a micro-thruster rocket of solid propellant under the condition of a loss of heat from the combustion zone is conducted.

The problem of stability of the engine is solved by applying the phenomenological  $T_0^*$ -theory.

In a micro-thruster rocket, the domain of stable combustion becomes much narrower, due to occurrence of strong  $\omega$ -instability, i.e. the exponential grow of perturbations with time. Nevertheless, there is a range of parameters, characterizing the laws of propellant combustion for which the sustained combustion may be possible.

## Keywords

*Rocket Micro-Engines on Solid Propellant, Efficient Initial Temperature,  $T_0^*$ -Theory, Unsteady Combustion, Instability of Burning*

## Nomenclature

$c_c$  – thermal capacity of solid propellant, J/(kg·K)  
 $c_p$  – gas thermal capacity by constant pressure, J/(kg·K)  
 $E$  – effective activation energy of chemical reactions in the gas phase, J/mol  
 $E_c$  – effective activation energy of the gasification reaction of the solid phase, J/mol  
 $F_{cr}$  – minimum (critical) cross-section of the nozzle, m<sup>2</sup>  
 $h_w$  – wall thickness, m  
 $j$  – heat flux, J/(m<sup>2</sup>·s)  
 $k, r$  – phenomenological coefficients  
 $L$  – heat of phase transition, J/kg  
 $p$  – pressure, Pa  
 $p_\infty$  – pressure and its characteristic value in F. Williams's equation, Pa  
 $R_c$  – internal radius of engine, m  
 $R_g$  – gas constant, J/(kg·K)  
 $R$  – universal gas constant, J/(K·mol)  
 $S_p$  – surface area of combustion, m<sup>2</sup>  
 $T_s$  – temperature of gasification surface of the solid propellant, K  
 $T_0$  – initial temperature, K  
 $T_0^*$  – effective initial temperature, K  
 $T_c$  – temperature in the solid phase, K  
 $T_{c,av}$  – “average” value of the propellant temperature, K  
 $T_b$  – actual temperature of the flame (gas phase), K  
 $T_{b,ad}$  – adiabatic temperature of flame (gas phase), K  
 $T_w$  – temperature of the wall, K  
 $T_k$  – temperature in the engine chamber, K  
 $T_d$  – characteristic temperature of dissociation, K  
 $t$  – time, s  
 $t_g$  and  $t_c$  – the characteristic times of the gas and solid phases of propellant, s

$u$  – burning rate, m/s

$V_k$  – volume of gas combustion products or combustion chamber volume, m<sup>3</sup>

$x_s(t)$  – coordinate of a surface of the gasification, m

$x_i(t)$  – coordinate of a thin zone of chemical reaction, m

$x$  – coordinate, m

$Y_s$  – concentration (volume fraction) of the product

### Greek Symbols

$\alpha$  – heat transfer coefficient, W·m<sup>-2</sup>·K<sup>-1</sup>

$\gamma$  – adiabatic index

$\kappa$  – thermal diffusivity of gas, m<sup>2</sup>/s,

$\kappa_c$  – thermal diffusivity of propellant, m<sup>2</sup>/s,

$\lambda_w$  – coefficient of heat conductivity of a wall, W·m<sup>-1</sup>·K<sup>-1</sup>

$\mu_c$  – molecular weight, kg/mol

$\mu$  and  $\nu$  – phenomenological coefficients

$\rho$  – solid propellant density, kg/m<sup>3</sup>

$\lambda_c$  – heat conductivity coefficient of solid propellant, W·m<sup>-1</sup>·K<sup>-1</sup>

$\rho$  – gas density, kg/m<sup>3</sup>

$\sigma$  – Stefan-Boltzmann constant, W m<sup>-2</sup> K<sup>-4</sup>

$\tau$  – dimensionless time

$\omega_f$  – frequency of fluctuations, Hz

$\omega$  – real frequency (dimensionless)

$\Omega$  – complex frequency (dimensionless)

### Introduction

With the appearance of ultra-small spacecraft [1, 2], the creation of micro-thrusters, running on solid propellant becomes important. They can be used for correction of the orbits, or for landing of spacecraft on asteroids and small planets. Besides, ultrafine motors can be used in microscopic military missiles.

Micro-thrusters are characterized by low ratio of volume to outer surface. At lower operating temperatures, this may lead to significant loss of heat from the propellant combustion zone. The relaxation time of gas-dynamic processes in the combustion chamber is also greatly reduced. These factors lead to new qualitative changes affecting the work of the micro-thruster.

Many relevant non-stationary processes in rocket engines: the establishment of a steady state burning, low-frequency and high-frequency sound fluctuations of the pressure and of the burning rate [3-10], or more complex vortex phenomena [11, 12], as a rule, are associated with the stability of steady state combustion of propellant in a combustion chamber of the rocket engine. Investigation of the stability is conveniently carried out on the basis of Zeldovich and Novozhilov theory (ZN-theory), where the basic laws are established from measurements of burning rate and temperature of surface of gasification of solid propellant in stationary mode of combustion [13, 14].

The phenomenological approach can also be formulated on the basis of the introduction of an explicit effective initial combustion temperature [15 – 17]. Here is given a summary of this approach.

From experiments on the observation of stationary burning functions

$$u^0 = u^0(p, T_0), \quad T_s^0 = T_s^0(p, T_0), \quad u^0 = u^0(p, T_s^0), \quad (1)$$

are determined the dependences for burning rate  $u^0$  and temperature of gasification surface of the propellant  $T_s^0$  of initial temperature  $T_0$  and pressure  $p$ . Steady state burning parameters are denoted by the superscript 0.

In unsteady combustion of solid propellant burning laws (1) can be written in the form

$$u = u(p, T_0^*), \quad T_s = T_s(p, T_0^*), \quad u = u(p, T_s), \quad (2)$$

where  $T_0^*$  – is an effective initial temperature.

Let  $\omega_f$  be the characteristic frequency of fluctuations of thermodynamic or hydrodynamic parameters, with  $t_g$ , and  $t_c$  – the characteristic times of the gas and solid phases of propellant, so that their relation is small,  $t_g/t_c \ll 1$ . In the low-frequency region is  $\omega_f t_g \ll 1$ . This inequality allows us not to consider in detail the processes in the gas phase, which greatly simplifies the theoretical study.

For reasons of convenience, any pair of equations (1) and (2) can be used in equations (1) and (2). To carry out a theoretical analysis, it is often necessary to introduce the phenomenological coefficients  $k$ ,  $r$ ,  $v$  and  $\mu$  [13, 14]:

$$k = \frac{\partial \ln u^0}{\partial T_0}, \quad r = \frac{\partial T_s^0}{\partial T_0}, \quad v = \frac{\partial \ln u^0}{\partial \ln p^0}, \quad \mu = \frac{1}{T_s^0 - T_0} \frac{\partial T_s^0}{\partial \ln p^0},$$

where  $p^0$  – is stationary base pressure.

The equation of heat transport is supplemented by the boundary condition for the heat flux at the gasification surface of the propellant (see below).

Previously, by other authors [18, 19] the temperature similar to  $T_0^*$  was proposed to determine from the first equation of (2). In  $T_0^*$ -theory [16, 17], this temperature is directly related to the instantaneous rate of burning and temperature gradient at the surface of the solid propellant, respectively, for an interval of the change of this temperature which is given an assessment.

### Physical Statement of the Problem

Let us consider the problem of one-dimensional stability of the combustion in the rocket motor of cylindrical shape with a relatively large heat loss (Fig. 1). Solid propellant has a heat capacity  $c_c$ , density  $\rho_c$ , coefficient of heat conductivity  $\lambda_c$ , and thermal diffusivity  $\kappa_c = \lambda_c/(c_c \rho_c)$ .

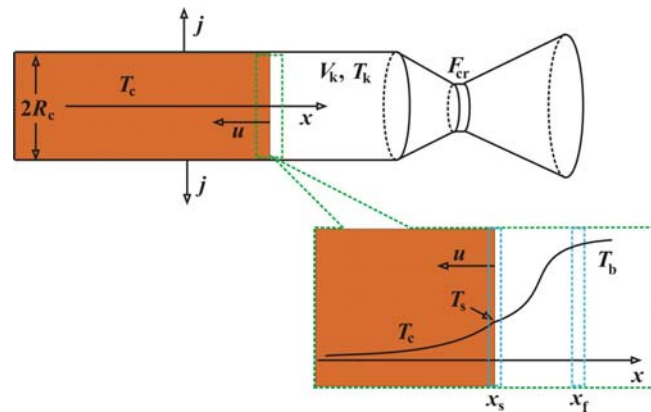


FIG. 1. SCHEMA OF A MISSILE MICRO-THRUSTERS WITH A CRITICAL SECTION  $F_{cr}$ ;  $R_c$  – INTERNAL RADIUS OF ENGINE;  $V_k$  – VOLUME OF GAS COMBUSTION PRODUCTS OR COMBUSTION CHAMBER VOLUME.

The temperature of the propellant in the solid phase is denoted  $T_c(t, x)$ .

On the surface at the coordinate  $x_s(t)$ , occurs the gasification of solid phase at a temperature  $T_s$ , the coordinate of a thin zone of chemical reaction is  $x_f(t)$ . Temperature of the flame (gas phase) is marked as  $T_b$ .

In the most unfavourable conditions of outer space the propellant in a micro-thruster must burn at ultra-low initial temperature  $T_0 \approx 2.73$  K. At the present time there are no experimental data indicating the possibility of burning at such low temperatures. We can only argue a reduction of combustion stability while reducing the initial temperature [13]. Therefore, below it is assumed that the condition for the existence of a stationary combustion [17] is fulfilled.

Heat flux  $j$  from the side surface of the propellant charge can be represented by the formula of Newton  $j = \alpha_\Sigma(T_c - T_0)$ , where  $\alpha_\Sigma$  – is heat transfer coefficient.

The total heat transfer coefficient can be calculated on the basis of the rule of addition of thermal resistances [20]: the heat flow from the propellant itself, then the heat transport through the outer wall of the apparatus, and the heat (mainly by radiation)  $\alpha_\Sigma^{-1} = \alpha_c^{-1} + \alpha_w^{-1} + \alpha_{eff}^{-1}$ . Here,  $\alpha_c^{-1} = 3\lambda_c/R_c$  results from the problem of cooling a cylinder

(regular mode),  $\alpha_w^{-1} = \lambda_w/h_w$  from the problem of heat transfer through the wall and

$$\alpha_{\text{eff}} = 4\sigma T_0^3 \left[ 1 + \frac{3}{2} \left( \frac{T_{c,\text{av}}}{T_0} - 1 \right) \right],$$

describes the heat loss due the radiation.

The loss of heat by radiation under the conditions of space dominates can be described by a nonlinear equation after the Stefan-Boltzmann:  $j = \sigma(T_w^4 - T_0^4)$ .

In this case it is difficult to obtain simple and descriptive analytical solution. The equation of heat loss can be linearized, representing  $j = \alpha_{\text{eff}}(T_w - T_0)$  with an effective heat transfer coefficient  $\alpha_{\text{eff}}$  with some "average" value of the propellant temperature  $T_{c,\text{av}} = \text{const}$ .

### Equation for the Energy in Solid Phase of the Propellant

The combustion front moves with velocity  $u = -dx_s/dt$ . With the same speed, it moves the  $x$ -coordinate. In the laboratory coordinate system, combustion front can be described by the equation [17]:

$$\frac{\partial T_c}{\partial t} + u \frac{\partial T_c}{\partial x} = \kappa_c \frac{\partial^2 T_c}{\partial x^2} - \frac{2\alpha_\Sigma}{c_c \rho_c R_c} (T_c - T_0). \quad (3)$$

Equation (3) allows the performing a complete analysis and gives a correct qualitative physical picture suitable for more complex types of heat loss.

Let the point  $x = 0$  coincide with the gasification surface of solid propellant. Then the boundary and initial conditions are given by [17]:

$$\begin{aligned} x \rightarrow -\infty: \quad T_c &= T_0; \\ x = 0: \quad T_c &= T_s(t, p), \quad \kappa_c \frac{\partial T_c}{\partial x} = gu(T_0^*, p)(T_s - T_0^*), \\ g &= \frac{1 + \sqrt{1 + 4\varphi}}{2}, \quad \varphi = \frac{\kappa_c}{(u^0)^2} \frac{2\alpha_\Sigma}{c_c \rho_c R_c}; \\ T_c(0, x) &= T_c^0(x). \end{aligned}$$

Let us introduce the following dimensionless quantities:

$$\text{temperature } \theta_c = (T_c - T_0)/(T_s^0 - T_0),$$

$$\text{burning rate } B = u/u^0,$$

$$\text{surface temperature } \theta_s = (T_s - T_0)/(T_s^0 - T_0),$$

$$\text{pressure } \eta = p/p^0,$$

$$\text{time } \tau = t(u^0)^2/\kappa_c \text{ and coordinate } \xi = u^0 x/\kappa_c.$$

Equation (3) in these new variables takes the form

$$\frac{\partial \theta_c}{\partial \tau} + B \frac{\partial \theta_c}{\partial \xi} = \frac{\partial^2 \theta_c}{\partial \xi^2} - \varphi \theta_c, \quad (4)$$

Equation (2) can now be brought in the form of:  $B = B(\theta_s^*, \eta)$ ,  $\theta_s^* = \theta_s^*(\theta_s, \eta)$  with the boundary and initial conditions

$$\xi = -\infty: \quad \theta_c = 0; \quad (5)$$

$$\xi = 0: \quad \theta_c = \theta_s, \quad \frac{1}{g} \frac{\partial \theta_c}{\partial \xi} = B(\theta_s^*, \eta)(\theta_s - \theta_s^*).$$

$$\theta_c(0, \xi) = \theta_c^0(\xi), \quad B^0 = 1, \quad \theta_s^0 = 1.$$

The stationary solution  $\theta^0(\xi)$  of equation (4) must satisfy the following boundary conditions:

$$\theta^0(-\infty) = 0, \quad \theta^0(0) = 1, \quad B = 1.$$

A simple calculation yields

$$\theta^0(\xi) = \exp(g\xi). \quad (6)$$

Relative pressure fluctuation  $\delta\eta = (p - p^0)/p^0$  are assumed to be very small. Therefore, it suffices to consider linear perturbations in temperature, combustion rate, etc., caused by changes in  $\delta\eta$ . Their dependence on the time can be represented by an exponential function  $\delta\eta \sim e^{\Omega\tau}$ , with  $\Omega$  as a complex frequency.

The surface temperature is a function of the effective initial temperature and pressure  $\theta_s = \theta_s(\theta_s^*, \eta)$  and can be expanded in series:

$$\theta_s \approx 1 + \frac{\partial\theta_s}{\partial\theta_s^*} \delta\theta_s^* + \frac{\partial\theta_s}{\partial\eta} \delta\eta.$$

Since  $\delta\theta_s = \theta_s - 1$ , then using the definition of the coefficients

$$r = \frac{\partial\theta_s}{\partial\theta_s^*} \approx \frac{\partial T_s^0}{\partial T_0}, \quad \mu = \frac{\partial\theta_s}{\partial\eta} \approx \frac{1}{T_s^0 - T_0} \frac{\partial T_s^0}{\partial \ln p},$$

the equation for  $\delta\theta_s^*$  can be expressed as:

$$\delta\theta_s^* = \frac{\partial\theta_s^*}{\partial\theta_s} \delta\theta_s - \frac{\partial\theta_s^*}{\partial\theta_s} \frac{\partial\theta_s}{\partial\eta} \delta\eta = \frac{\delta\theta_s}{r} - \frac{\mu}{r} \delta\eta.$$

Then, taking into account the resulting equation we obtain for the burning rate the following representation [10]:

$$B(\theta_s^*, \eta) \approx 1 + \frac{\partial B}{\partial\theta_s^*} \delta\theta_s^* + \frac{\partial B}{\partial\eta} \delta\eta = 1 + \frac{\partial B}{\partial\theta_s^*} \left( \frac{\delta\theta_s}{r} - \frac{\mu}{r} \delta\eta \right) + \frac{\partial B}{\partial\eta} \delta\eta.$$

Here the derivations of the function of burning rate can be written using definition of the coefficients

$$k = \frac{\partial B}{\partial\theta_s^*} \approx (T_s^0 - T_0) \frac{\partial \ln u^0}{\partial T_0}, \quad v = \frac{\partial B}{\partial\eta} \approx \frac{\partial \ln u^0}{\partial \ln p}$$

as following:

$$B = 1 + \frac{k}{r} \delta\theta_s + \left( v - \frac{\mu k}{r} \right) \delta\eta. \quad (7)$$

The difference  $\theta_s - \theta_s^*$  included in the second boundary condition (5) must be also written in the linear approximation:

$$\theta_s - \theta_s^* = 1 + \delta\theta_s - \delta\theta_s^* = 1 + (1 - 1/r) \cdot \delta\theta_s + \mu \cdot \delta\eta/r.$$

Therefore, the second boundary condition in equation (5) after accounting the equality (7) after simple transformations takes the form

$$\frac{1}{g} \frac{\partial\theta_c}{\partial\xi} = 1 + \frac{k+r-1}{r} \delta\theta_s + v \delta\eta. \quad (8)$$

Let's find the solution the differential equation (4).

Assuming that

$$\theta_s = \exp(g\xi) + \delta\theta_s, \quad \delta\theta_s = \mathcal{A} \cdot e^{\Omega\tau}, \quad B = 1 + b e^{\Omega\tau},$$

where  $\delta\theta_s$  and  $b \cdot e^{\Omega\tau}$  – are small perturbations of temperature and burning rate with amplitudes  $\mathcal{A}(\xi)$  and  $b$ .

The use of equation (4), holding only linear values, leads to the equation

$$\frac{d^2 \mathcal{G}_c}{d\xi^2} - \frac{d\mathcal{G}_c}{d\xi} - (\varphi + \Omega)\mathcal{G}_c = b \frac{d\theta_c^0}{d\xi}.$$

Its solution corresponding to the condition  $\mathcal{G}_c(-\infty) = 0$  has the form

$$\mathcal{G}_c(\xi) = A \cdot e^{z\xi} - b \frac{g}{\Omega} \cdot e^{g\xi}, \quad z = \frac{1 + \sqrt{1 + 4(\varphi + \Omega)}}{2}. \quad (9)$$

In equation (7) and in the boundary condition (8), let's go over to the amplitude  $b$  of the perturbation of burning rate  $b$  and to the temperature of the propellant surface  $\mathcal{G}_c(0)$ :

$$b \cdot e^{\Omega\tau} = \frac{k}{r} \mathcal{G}_c(0) \cdot e^{\Omega\tau} + \left( v - \frac{\mu k}{r} \right) \delta\eta, \quad (10)$$

$$\frac{e^{\Omega\tau}}{g} \frac{\partial \mathcal{G}_c(0)}{\partial \xi} = \frac{k+r-1}{r} \mathcal{G}_c(0) \cdot e^{\Omega\tau} + \left( \frac{\mu}{r} + \frac{vr - \mu k}{r} \right) \delta\eta.$$

If there the formula (9) for  $\mathcal{G}_c(\xi)$  is used, then after simple transformations two equations for the variables  $A$  and  $b$  can be obtained:

$$A(z - ag) + \frac{k-1}{r} \frac{g^2}{\Omega} b = (\mu + \Delta) \frac{g}{r} e^{-\Omega\tau} \delta\eta, \quad (11)$$

$$A - \left( \frac{r}{k} + \frac{g}{\Omega} \right) b = -\frac{\Delta}{k} e^{-\Omega\tau} \delta\eta,$$

$$a = \frac{k+r-1}{r}, \quad \Delta = vr - \mu k.$$

The pressure fluctuation can be presented similar as ( $\eta_a$  – amplitude)

$$\delta\eta = \eta_a \exp(\Omega\tau). \quad (12)$$

From the equations (11) the relationship between the amplitudes of the burning rate  $b$  and pressure  $\eta_a$  can be found as:

$$b \left[ \left( r + \frac{kg}{\Omega} \right) (z - g) - g(k-1) \right] = [vg + \Delta(z - g)] \eta_a. \quad (13)$$

The Equation for the Pressure in the Combustion Chamber

Modeling of processes in the gas phase and the mechanism of the decomposition the solid phase of a propellant represents a separate complex and important task. This was the subject in a large number of studies [21-27 et al.]. Even modeling the properties of homogeneous propellant [21, 22] is fraught with difficulties.

Therefore, it is of interest when the most general laws of combustion are used. The simplest models are given by Belyaev-Zel'dovich [13, 14], Merzhanov-Dubovitskii [27], and Denison-Baum [21]. They can be interpreted as special cases of the model of Williams [22]:

$$u = \text{const} \cdot \exp\left(-\frac{E_c}{2RT_s}\right) \left[ 1 - \frac{pY_s}{p_\infty} \exp\left(\frac{\mu_c L}{RT_s}\right) \right].$$

Here are:  $E_c$  – effective activation energy of the gasification reaction (pyrolysis) of solid phase of the propellant;  $R$  – universal gas constant;  $p$  and  $p_\infty$  – pressure and the characteristic value of  $p$  when the heat of phase transition of evaporation  $L$  dominates the pyrolysis;  $Y_s$  – concentration (volume fraction) of the product of gasification with a molecular weight  $\mu_c$ .

According to Williams [22], at low pressures  $p \ll p_\infty$ , the gasification of propellant occurs like pyrolysis (model of Merzhanov-Dubovitskii [27], and Denison-Baum [21]) and the burning rate is  $u = \text{const} \cdot \exp(-E_c/2RT_s)$ .

At high pressures  $p \gg p_\infty$ , the gasification propellant is like the evaporation (model of Belyaev-Zeldovich) and the concentration  $Y_s$  and the temperature  $T_s$  on the surface are linked by Clausius-Clapeyron relation:  $Y_s = p_\infty p^{-1} \exp(-\mu_c L / RT_s)$ .

For a relatively slow time-dependent processes ( $\omega t_g \ll 1$ ), the results of investigating the stability of combustion produced using by the models Belyaev-Zel'dovich and Merzhanov-Dubovitskii or Denison-Baum, [6–8, 10] are almost equivalent with the accuracy of the order  $\omega^2 t_g^2$ .

Thus, when the inequality  $\omega t_g \ll 1$  is valid then the gasification mechanism of propellant and processes in the gas phase are not significant till small quantities of the order  $\omega^2 t_g^2$ . Therefore, the study of stability in the range of frequencies  $\omega_f \ll 1/t_g$  can be done using the simplest models of the gas phase in the combustion chamber of the engine.

In the simplest model of the gas phase in the combustion chamber, only the change of pressure and density [13, 14, 28] is taken into account.

Let  $S_p$  – be the surface area of combustion. Typically, the characteristic time (maximum) of unsteady processes is such that the burning surface during this period varies slightly. Therefore we can assume that the  $S_p \approx \text{const}$ . The mass flow velocity of burned propellant is  $\rho_c u S_p$ .

The mass of gas, escaping via the engine nozzle per unit of time is equal to  $A_c p F_{cr}$ , where  $A_c = \text{const}$ , and  $F_{cr}$  is the minimum (critical) cross-section of the nozzle.

The rate of change of gas mass  $\rho V_k$  in the chamber with a volume  $V_k$  is determined by the difference between the gas which comes from the combustion and the amount of substances exiting through the nozzle:

$$\frac{d(\rho V_k)}{dt} = \rho_c u S_p - A_c p F_{cr}, \quad (14)$$

$$A_c = \frac{\Gamma(\gamma)}{\sqrt{R_g T_k}}, \quad \Gamma(\gamma) = \sqrt{\gamma \left( \frac{2}{\gamma+1} \right)^{\frac{\gamma+1}{\gamma-1}}},$$

where are:  $R_g$  – gas constant;  $\gamma$  – adiabatic index;  $T_k$  – temperature in the engine chamber.

In absence of solid particles (metals, their oxides, etc.), the density of the gas can be determined from the equation of state of ideal gas  $\rho = p / R_g T_k$ .

Under unsteady conditions in the combustion chamber, the changes in the density and pressure of the gas are significantly superior to the change in temperature, so that  $T_k \approx \text{const}$  can be taken [28].

Then equation (14) can be written as

$$\frac{V_k}{R_g T_k} \frac{dp}{dt} = \rho_c u S_p - A_c p F_{cr}. \quad (15)$$

The stationary pressure  $p^0$  in the combustion chamber according to burning rate  $u = u_b(T_0) \cdot (p/p_0)^v$ , ( $p_0$  – is the initial pressure) is determined from the condition  $dp/dt = 0$ :

$$p^0 = \frac{\rho_c u^0 S_p}{A_c F_{cr}} = p_0 \left( \frac{\rho_c S_p u_b}{A_c F_{cr}} \right)^{\frac{1}{1-v}}.$$

In dimensionless form, equation (15) contains only one the devise constant  $\chi$  [13, 14, 28]:

$$\chi \frac{d\eta}{d\tau} = B - \eta, \quad (16)$$

$$\chi = \frac{(u^0)^2 V_k}{\kappa_c R_g T_k A_c F_{cr}},$$

with is the ratio  $t_g/t_c \approx t_k/t_c$ , with

$$t_g = \frac{1}{V_k} R_g T_k A_c F_{cr}, \quad t_c = \frac{\kappa_c}{(u^0)^2}.$$

### Dispersion Equation

From equation (16) for non-stationary component of the pressure follows:

$$\chi \frac{d\delta\eta}{d\tau} = b \cdot e^{\Omega\tau} - \delta\eta.$$

Taking into account the representation of the pressure by equation (12), the following algebraic equation can be obtained [13, 14]:

$$b = (1 + \chi\Omega)\eta_a. \quad (17)$$

For a finding of sustainable combustion, the system of equations (13) and (17) with unknown  $b$  and  $\eta_a$  must have a nontrivial solution. This is possible if its determinant is zero. The vanishing of the determinant gives the dispersion equation for the frequency  $\Omega$ :

$$\left[ (z - g) \left( r + \frac{kg}{\Omega} \right) - g(k - 1) \right] (1 + \chi\Omega) - gv - (z - g)\Delta = 0. \quad (18)$$

If  $\varphi = 0$ , then  $g = 1$  and  $z = (1 + (1 + 4\Omega)^{1/2})/2$ . Then from equation (18) follows equation obtained by Novozhilov [13, 14].

Assume the dependence of the burning rate only on the surface temperature:  $u(T_s)$ . This means that in the experiments found dependences of burning rate on pressure, for example, the form  $u = u_b(T_0) \cdot (p/p_0)^v$ , results from two factors [13, 14]:

- 1) the existence of a relationship  $T_s(p, T_0)$ ;
- 2) the vanishing of the Jacobian, i.e.

$$J = \frac{\partial(u, T_s)}{\partial(p, T_0)} = \frac{\partial u}{\partial p} \frac{\partial T_s}{\partial T_0} - \frac{\partial u}{\partial T_0} \frac{\partial T_s}{\partial p} = 0.$$

The condition that the Jacobian is equal to zero in the dimensionless variables can be written as

$$J' = \frac{\partial(B, \theta_s)}{\partial(\eta, \theta_0^*)} = \frac{\partial B}{\partial \eta} \frac{\partial \theta_s}{\partial \theta_0^*} - \frac{\partial B}{\partial \theta_0^*} \frac{\partial \theta_s}{\partial \eta} = \Delta = vr - \mu k = 0.$$

Note, in practice usual is valid that  $v \sim k \sim 1$ ;  $r \sim \mu \ll 1$ . At the present level of experimental techniques can be found that  $J' \sim 10^{-1} \dots 10^{-2}$ . Such values are comparable to experimental errors [13] and accordingly allows to take equality  $\Delta = 0$ .

Therefore, equation (18) can be written in the form

$$\left[ \left( \frac{z}{g} - 1 \right) \left( r + \frac{kg}{\Omega} \right) - k + 1 \right] (1 + \chi\Omega) - v = 0. \quad (19)$$

The combustion chamber volume in micro-thruster  $V_c \rightarrow 0$  and critical section  $F_{cr} \rightarrow 0$ , but so that the ratio  $V_c/F_{cr} \rightarrow 0$ . Therefore, for such engine parameter is valid that  $\chi \ll 1$ . Investigation of stability at low values of  $\chi$  by analytical and numerical methods, but without the loss of heat from the solid propellant ( $\varphi = 0$ ) is presented in [29-31]. From the results of [29, 30], it implies the possibility of stable operation of the micro-motor both when  $v < 1$  and  $v > 1$ .

Equation (19) relative to the variable  $\Omega$  can have multiple roots. Combustion mode is unstable if at least one of the roots leads to unstable behavior.

If  $r \neq 0$ , then oscillatory properties of burning propellant may occur [13, 14]. On the curve of parameters for which such properties will be observed, the real part of the frequency  $\Omega$  is equal to zero and  $\Omega = i\omega$ , where  $i = (-1)^{1/2}$  – complex imaginary unit and  $\omega$  – real frequency. The perturbations on this curve (neutral) do not grow or decay. Often, such a curve is the boundary of neutral stability.

For building the curve of neutrality demands to express the coefficients  $k, v$  as parametric functions of frequency  $\Omega$ :

$$k = \frac{\operatorname{Im} \left[ \frac{\frac{v}{1 + \chi\Omega} - 1}{z/g - 1} \right]}{\operatorname{Im} \left[ \frac{(z-g)/\Omega - 1}{z/g - 1} \right]}, \quad r = \frac{\operatorname{Im} \left[ \frac{\frac{v}{1 + \chi\Omega} - 1}{(z-g)/\Omega - 1} \right]}{\operatorname{Im} \left[ \frac{z/g - 1}{(z-g)/\Omega - 1} \right]}, \quad v = \frac{\operatorname{Im} \left[ \frac{r(z/g - 1)}{(z-g)/\Omega - 1} \right] + \operatorname{Im} \left[ \frac{1}{(z-g)/\Omega - 1} \right]}{\operatorname{Im} \left[ (1 + \chi\Omega) \left( \frac{z-g}{\Omega} - 1 \right) \right]^{-1}}.$$

Here operation  $\operatorname{Im}$  means taking the imaginary part. One can eliminate here the variable  $\Omega$ , taking any pair of equations and thus build the necessary dependence, for example,  $r(k)$  or  $v(k)$ .

The values  $r, k, v$  calculated according to the given formulas may occur to be negative. The parameters  $r, k$  may be less than zero in two cases [15, 16]:

- 1) the gasification reaction of solid phase is strongly endothermic. Then the reaction heat provides surface temperature  $T_s$  lower than the initial temperature  $T_0$ ;
- 2) the excitation of oscillatory energy and dissociation in the gas flame are so strong that the effective activation energy  $E$  varies considerably with increasing of temperature. Under quadratic law  $E = E_0(1 + T^2/T_d^2)$  proposed in [32], where are:  $E_0$  – conditional activation energy at zero temperature and  $T_d$  – characteristic temperature of dissociation, the theoretical values of the phenomenological coefficients  $r$  and  $k$  can be calculated by the following formulas [15, 16]:

$$r = \frac{E}{E_c} \varpi, \quad k = \frac{E(T_s - T_0)}{2RT_s^2} \varpi, \quad \varpi = \left( \frac{T_s}{T_b} \right)^2 - \left( \frac{T_s}{T_d} \right)^2. \quad (20)$$

For  $\varpi > 0$  the parameter  $k < 0$ , if  $T_s < T_0$  (the first case). The validity of inequality  $T_d < T_b$  leads to negative  $r$  and  $k$ , if  $T_s > T_0$  (the second case). Both cases are exotic for physics of combustion, but it is interesting from theoretical point of view. It was shown by the analysis using a detailed simulation of combustion [15, 16], that for such cases exist sustainable solutions.

Below we restrict ourselves to the values  $r > 0, k > 0, v > 0$ , because there are currently no experimental data indicating the presence of phenomenological coefficients with a negative sign.

State of combustion is determined by three parameters  $k, r$  or  $v$ . Graphically it can be displayed in a space of three coordinate axes, each axis belongs to one of the variables  $k, r$  or  $v$ . If we consider any pair of these variables, the stability boundary is a line, as shown in Fig. 2. If we consider all three variables, the boundary appears as a surface.

We emphasize here the following. Stationary (stable) burning propellant assumes the suppression of any fluctuations in temperature or pressure in a system “combustion chamber – propellant”. Linear analysis of fluctuations of small amplitude applied in the article may indicate the limit set of parameters on which this condition breaks.

In the space of parameters describing the system, the configuration of stability boundary is complex. But even building it in a multi-dimensional space of parameters, we can not predict with certainty the behaviour of the system at some distance from the boundary. Within the stability region, combustion is stable, but outside of it, this may be extinction, uncontrolled flare-up or burning with finite amplitude fluctuations.

This can be detected during the application of non-linear analysis. It should be noted that apart from the boundary of stability due to feedback between the fluctuations and stable state of the system, itself stable state of the system may be disturbed by the mechanism of the thermal imbalance in the combustion zone.

### $\Lambda$ -Instability and $\omega_0$ -Instability

Let's perform the approximate calculation of the unsustainable combustion.

In equation (19)  $\chi = 0$  is set. Then the new equation

$$\left(\frac{z}{g} - 1\right) \left(r + \frac{gk}{\Omega}\right) - k + 1 - v = 0$$

after simple transformations reduces to the form:

$$\Omega^2 + \frac{g^2 \Lambda}{r^2} \Omega + \omega_0^2 = 0, \quad (21)$$

Here two parameters:

$$\Lambda = \frac{r}{g} [2k - (2g - 1)(v + k - 1)] - (v + k - 1)^2, \quad \omega_0^2 = \frac{kg^2 [k - (2g - 1)(v + k - 1)]}{r^2}$$

are introduced.

Such dispersion equations of the second degree indicate the presence of second order non-linear differential equation for the non-stationary temperature)  $\theta(\tau)$  of gasification surface and the burning rate  $B(\tau)$  [15, 16, 32, 33].

From here there is the possibility of analysis of unsteady combustion modes, using interpretation of the theory of dynamical systems [34]. Thus, in equation (21) the complex  $g^2 \Lambda / r^2$  can be interpreted as the "viscosity",  $\omega_0^2$  – as a returning force.

According to theory of dynamical systems, if  $\omega_0^2 > 0$ , then combustion is unstable when the inequality  $\Lambda < 0$  is valid (i.e., dynamical systems [34] with "negative viscosity", hence the name " $\Lambda$ -instability"). This inequality can be written as

$$r < \frac{g(v + k - 1)^2}{2k - (2g - 1)(v + k - 1)}.$$

The boundary of instability is found from the equation  $\Lambda = 0$ , it is given by the quadratic equation with respect to the complex  $v + k - 1$ :

$$g(v + k - 1)^2 + r(2g - 1)(v + k - 1) - 2rk = 0.$$

The solution of this equation gives the boundary of instability. Two roots of this equation are given by the expressions:

$$v_{1,2} = 1 - k + \frac{-r(2g - 1) \mp \sqrt{r^2(2g - 1)^2 + 8rkg}}{2g}. \quad (22)$$

The root  $v_1$  corresponds to the negative sign before the radical, the root  $v_2$  – to the positive sign.

The values from the interval  $v_1 < v < v_2$  correspond to stability condition.

But the dispersion equation (21) is obtained as a result of transformations to get rid of radicals, so the equation (21) may give "parasitic" solutions. Such a solution is the root  $v_1$ .

Let us consider a special case.

The boundary of instability as a function  $v(k)$ , which is built with the values of the parameters  $\varphi = 1$  ( $g = 1.618$ ),  $r = 0.1$  and  $r = 0.15$  is shown in Fig. 2.

The upper and the lower parts of the curves in Fig. 2 are built by the formulas (22).

The "parasitic" solution is shown by lower dashed curves  $FD$  in Fig. 2.

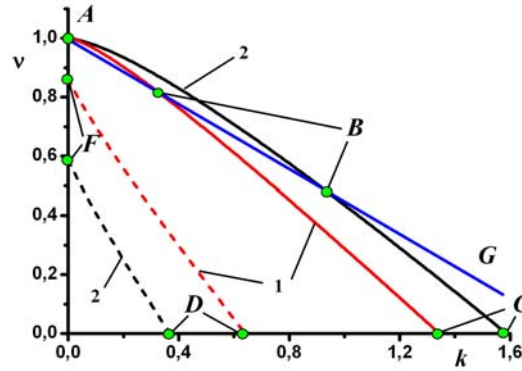


FIG. 2. AN EXAMPLE OF CALCULATION OF BOUNDARIES OF THE STABLE COMBUSTION REGION. THE GRAPHS OF CURVES  $FD - v_1(K, G)$  AND  $ABC - v_2(K, G)$ . THE VALUES OF PARAMETERS:  $\chi = 0$ ,  $\varphi = 1$ ; CURVE 1 -  $r = 0.1$ ; CURVE 2 -  $r = 0.3$ .

To construct a complete picture of the considered physical phenomenon, we take into account that the instability may occur as a result of the acquisition of a negative sign of the natural frequency  $\omega_0^2$  (so called  $\omega_0^2$ -instability).

Therefore, to complete the analysis, the region bounded by the two curves  $v_1(k, g)$  and  $v_2(k, g)$ , must be supplemented by another condition of stability loss ( $\omega_0^2 < 0$ , for considered case  $\varphi = 1$ ),

$$v > 1 - k \frac{2(g-1)}{2g-1} = 1 - 0.55k.$$

In Fig. 2, this inequality corresponds to the area above the straight line  $AG$ . As a result, the region of stable operation of the micro-motor at low frequencies covers an area which lies partly below the line  $AB$  and partly - below the curve  $BC$ . Moreover, the loss of stability above the curve  $BC$  happens with the oscillations in the rate of combustion, but above the straight line  $AB$  oscillations are absent.

It is possible to come to these results in a different way: let the frequency  $\Omega$  to be a real number. Near the stability limit is valid  $\Omega \ll 1$ . Using in equation (9) Taylor series expansion of the parameter  $z$  in powers of  $\Omega$ :

$$z \approx g + \frac{\Omega}{\sqrt{1+4\varphi}} - \frac{\Omega^2}{(1+4\varphi)^{3/2}} = g + \frac{\Omega}{2g-1} - \frac{\Omega^2}{(2g-1)^3},$$

from equation (19) follows:

$$v = 1 - k \frac{2(g-1)}{2g-1}. \quad (23)$$

It coincides with the previous equation, when in it the sign of inequality is changed to equality.

Thus, the only boundary of instability without oscillations corresponds to equality  $\omega_0^2 = 0$ . This conclusion is confirmed by the numerical solution of the equation (19), with  $\chi \neq 0$ .

Area of  $\Lambda$ -instability goes to the limit value if reducing the heat loss from the combustion zone, but does not disappear, while ensuring perfect thermal insulation of the combustion zone ( $\varphi = 0$ ,  $g = 1$ ).

Let's consider some results of numerical analysis of the equation (19) of determining the conditions of  $\Lambda$ -instability (the origin of this term see below) taking the frequency  $\Omega = i\omega$ .

For illustration we take the following values  $\chi = 0.01$ ;  $r = 0.2$ ;  $\varphi = 1$ . The results are presented in Fig. 3.

In the range of frequency  $\omega$  from 0 to  $\omega_{\max} = 6.3$ , there is a neutral curve  $BC$ . Segment  $AB$  is a part of a straight line  $AG$  with the equation  $v = 1 - 0.55k$ , (special case of equation (23)). For frequencies  $\omega > \omega_{\max}$  is the parameter  $v < 0$ .

While with the increase of the heat loss from the combustion zone (if  $\varphi$  increases), the area of occurrence of  $\Lambda$ -instability reduces but the area of  $\omega_0$ -instability increases (Fig. 4). But general the region of stable burning is reduced.

In the range of  $0 < k < 0.4$  (curve 1 in Fig. 4), there are no oscillatory solutions.

Part 2 of the curve 2 in Fig. 4 ( $0 < k < 0.77$ ), which is the boundary of  $\omega_0^2$ -instability, is built by the formula (22)  $v = 1 - 0.72k$ .

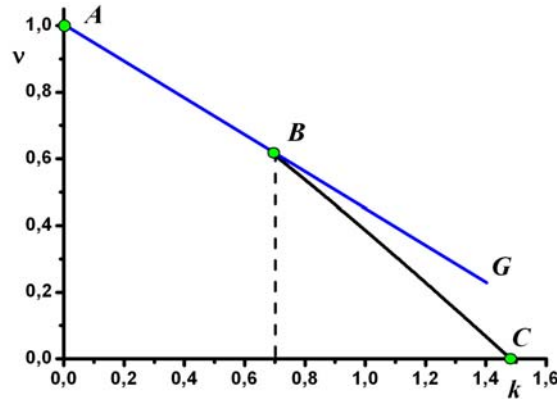


FIG. 3. THE BOUNDARY OF STABILITY AT  $\text{PPII } r = 0.2; \varphi = 1$  AND  $\chi = 0.01$ . THE DOTTED LINE PRESENTS THE BORDER OF EXISTENCE OF TWO TYPES OF INSTABILITY.

When comparing the curves in Fig. 2 and Fig. 4, build with  $r = 0.1$ , their notable difference can not be detected.

Here already  $\chi\omega_{\max} \approx 0.14$  can not be considered much less than unity.

Increase  $\varphi$  from 1 to 3 leads to an increase  $\omega_{\max}$  from 14.2 to 15.2. It is also found that with good accuracy  $\omega_{\max} \sim 1/r$ .

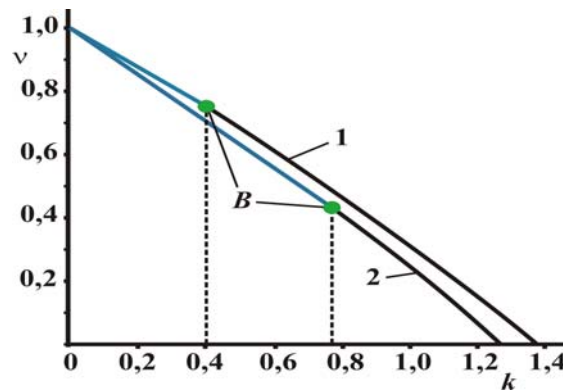


FIG. 4. CHANGING OF THE BOUNDARIES OF THE STABLE COMBUSTION REGION FOR THE PARAMETERS  $r = 0.1; \chi = 0.01$  AND DEPENDING ON THE PARAMETER  $\varphi$ : 1 -  $\varphi = 1$ ; 2 -  $\varphi = 3$ .

Increase of heat loss narrows the field of sustainability, but only up to certain limits. For each value of  $r$ , there exists such  $\varphi = \varphi_*$ , above which the boundary of the stability region is set to line  $v = 1 - \text{const} \cdot k$ . For  $\varphi > \varphi_*$  the imaginary part of the root  $\Omega$  is equal to zero and there is no oscillatory instability. For example, when  $r = 0.1$  and  $0.2$ , respectively  $\varphi_* \approx 4$  and  $12$ .

Comparison of the results obtained by the formula (22) for  $v = v_2$  and numerical solution of the equation (19) shows the good accuracy of this analytical expression, except for a small vicinity near  $v = 0$ .

$\omega_0$ -Instability and Condition for the Existence of Combustion

This kind of instability in contrast to the above discussed  $\Lambda$ -instability develops with increasing heat losses from the combustion zone in the gas phase.

From the dispersion equation for  $\chi = 0$ , it follows that if  $\omega_0^2 < 0$ , then combustion is always unstable (i.e. for any sign of  $\Lambda$ ) and oscillatory solutions for perturbations are absent.

The requirement for the stability  $\omega_0^2 > 0$ , or  $(2g - 1) = (1 + 4\varphi)^{1/2} \leq k/(v + k - 1)$ , leads to the existence of critical value of  $\varphi_{cr}$ . His excess will cause  $\omega_0$ -instability, and that such no instability appears it is necessary

$$\varphi < \varphi_{cr} = \frac{1}{4} \left[ \frac{k^2}{(v + k - 1)^2} - 1 \right]. \tag{24}$$

In practice, it is required to create a stable engine running on propellant with desired properties.

Therefore, the condition (24) is better to express in the form of restrictions on the heat transfer coefficient  $\alpha$  and the radius of engine  $R_c$ :

$$\frac{\alpha}{R_c} < \frac{c_c(m^0)^2}{8\rho_c\kappa_c} \left[ \frac{k^2}{(\nu+k-1)^2} - 1 \right], \quad m^0 = \rho_c u^0. \quad (25)$$

Condition given in (25) to determine the stability region, makes sense if the other condition of existence of stationary combustion of gas in narrow tubes [35] is met.

Assume the chemical reaction with a single effective activation energy  $E$ . Gas thermal capacity possess a constant pressure  $c_p$ , density  $\rho$  and coefficient of thermal diffusivity  $\kappa$ . The flame in gas has the adiabatic temperature  $T_{b,ad}$ .

Heat losses result in lower combustion temperatures below this, adiabatic. Since the burning rate is highly dependent on the combustion temperature, its reduction leads, as shown by the analysis [35] to the breakdown of combustion. Using the results of [35], the condition for the existence of stationary combustion in the combustion chamber is:

$$\frac{\alpha}{R_c} < \frac{1}{4e} \frac{c_p(m^0)^2}{\rho\kappa} \frac{RT_{b,ad}^2}{E(T_{b,ad} - T_s)}, \quad e \approx 2.72. \quad (26)$$

Assuming  $T_d \gg T_{b,ad}$ , from (20) we obtain [16, 36]:

$$k = \frac{E(T_s - T_0)}{2RT_{b,ad}^2}.$$

Now, the inequality (26) takes the form

$$\frac{\alpha}{R_c} < \frac{1}{8e} \frac{c_p(m^0)^2}{\rho\kappa} \frac{T_s - T_0}{k(T_{b,ad} - T_s)}, \quad (27)$$

or in the form of a limit on the value of the parameter  $k$ :

$$k < \frac{1}{8e} \frac{c_p(m^0)^2 R_c}{\alpha\rho\kappa} \frac{T_s - T_0}{T_{b,ad} - T_s}. \quad (28)$$

According to inequality (28), the region of sustainable work of the micro-thruster in Fig. 4 can be further split by vertical lines. As a result, the stability region narrowed even more.

Comparing the result (27) with the condition (25), we see that  $\omega_0$ -instability can occur if

$$\frac{1}{e} \frac{c_p\rho_c\kappa_c}{c_c\rho\kappa} \frac{T_s - T_0}{T_{b,ad} - T_s} > k \left[ \frac{k^2}{(\nu+k-1)^2} - 1 \right].$$

In the rocket combustion chamber  $(T_s - T_0)/(T_{b,ad} - T_s) \sim 0.1$ ;  $c_p/c_c \sim 1$ ;  $\rho_c/\rho \sim 10^3$ ;  $\kappa_c/\kappa \sim 0.01$ . Therefore, as in the left-hand side, as in the right part, there is a number at order of unity. Therefore, the above inequality can be satisfied if  $\nu + k \approx 1$ .

## Conclusion

In a rocket micro-thrusters when the parameter  $\nu < 1$ , different kinds of manifestations of unstable combustion can be met:  $\Lambda$ -instability with a characteristic amplitude decay of burning rate and  $\omega_0$ -instability, which is characterised by sustained oscillations of burning rate. The first one is weakened by increasing of the parameters  $r$  and  $\varphi$ , the second one – amplified.

Their presence, particularly  $\omega_0$ -instability poses a number of technical difficulties in creating of micro-thrusters.

In the case of  $\Lambda$ -instability, the growth of perturbations occurs in an oscillatory manner, combustion can reach the self-oscillating mode.

Extinction might not occur and the engine continues to run.

For a  $\omega_0$ -instability, the growth of disturbances occur without fluctuations, and at high heat loss from the combustion zone, it will lead to extinction.

New equations for the boundaries of the region of stable combustion in the combustion chambers of ultra-small rocket engines are derived.

The change in the sign of the parameter  $\varphi$  can be formally interpreted as a case of having preheating of the combustion zone. When heating, the combustion in the engine can become more sustainable.

Such an interpretation of the parameter  $\varphi$  is possible (and useful in the sense of generality of formulation of the problem), although it cannot fully reflect the heating of propellant from the outside.

One option could be a heat flow from a gas flame zone along the walls charge-containing cells. A prerequisite for this is to have a high thermal diffusivity of the wall material, much larger than the thermal diffusivity of the propellant itself.

Another variant of amplification the propellant heating may be use of conductive elements (e.g. metal wires) extending through the propellant toward the combustion front. Contacting one end with a gas flame, such elements also contribute to the rapid transfer of heat deep into the fuel.

For the design of ultra-small micro-thrusters for spacecraft of interest are the propellants, in which the parameters  $\nu$  and  $k$  are much smaller than unity.

The reason for this is that there are restrictions on the parameter  $k$  at low initial temperatures, as well as the achievement the limiting border  $\nu + k < 1$  of the instability region with an increase in heat loss from the combustion zone.

From the limit of stability conditions  $\nu + k < 1$  follow the restrictions  $k < 1$  и  $\nu < 1$ .

These inequalities will be more correct, considering the decrease in the specific heat of solids ( $c_s$ ) with a very low initial temperature  $T_0$  (Debye-Einstein equation).

The presented method of the analysis and the results can be applied to the study of stable combustion in hybrid rocket micro-motor [37-39]. In this case, the main feature of the hybrid combustion engines – the strong dependence of the combustion rate of the solid propellant of the blowing by gases, is not an important factor. Gasification of solid propellant is determined by universally temperature  $T_s$ , its quantity primarily depends on the ratio between the flow of heat from the gas phase to the surface of the gasification and the heat flux in the solid phase.

## REFERENCE

- [1] Sandau R., Roeser H.-P., and Valenzuela A., 2008. *Small Satellites for Earth Observation*, Springer.
- [2] Tristancho Joshua, and Gutierrez Jordi, 2012. *Implementation of a femto-satellite and a mini-launcher*, Universitat Politècnica de Catalunya: 3. Retrieved 12 December 2012.
- [3] Kurabayashi H., Sato A., Yamashita K., Nakayama H., Hori K., Honda M., and Hasegawa K., "Ultrasonic measurements of burning rates in full-size rocket motors", *Progress in Propulsion Physics*, Issue 2, 2011, pp. 135-148.
- [4] Myrzakulov R., Kozybakov M. J., and Sabdenov K. O., "The extinction of the burning rocket propellants and explosives at alternating pressure", *Bulletin of the Tomsk Polytechnic University* (in Russia), Vol. 309, No. 5, 2006, pp. 96-102.
- [5] Myrzakulov R., Kozybakov M. J., and Sabdenov K. O., "Modeling of acoustic instability in the chamber of the rocket engine with solid fuel", *Bulletin of the Tomsk Polytechnic University* (in Russia), Vol. 309, No. 6, 2006, pp. 134-138.
- [6] Sabdenov K. O., and Min'kov L. L., "Distinctive features of combustion of a propellant at a Lewis number other than unity in the gas phase", *J. of Engineering Physics and Thermophysics*, Vol. 74, No. 6, 2001, pp. 1437-1453.

- [7] Sabdenov K. O., "Modes of combustion of solid rocket propellant, breaking up the gas on the mechanism of pyrolysis", *Bulletin of the Tomsk Polytechnic University* (in Russian), Vol. 309, No. 3, 2006, pp. 120-125.
- [8] Novozhilov B. V., "The influence of inertness gas phase on the stability combustion of the volatiles condensed systems", *Khimicheskaja fizika* (in USSR), Vol. 7, No. 3, 1988, pp. 388-396.
- [9] Kaganova Z. I., "The influence of Lewis number on to magnitude of acoustic conductivity of the burning condensed matter", *Khimicheskaja fizika* (in USSR), Vol. 12, No. 6, 1993, pp. 866-873.
- [10] Vilyunov V. N., and Sabdenov K. O., "To phenomenological theory of unsteady burning", *Chemical Physics Reports*, Vol. 11, No. 3, 1992, pp. 415-423.
- [11] Francois Vuillot, "Vortex-shedding phenomena in solid rocket motors", *J. of Propulsion and Power*, Vol. 11, No. 4, 1995, pp. 626-639.
- [12] Boyer G., Casalis G., and Estivalèzes J.-L., "Stability analysis and numerical simulation of simplified solid rocket motors", *Physics of Fluids*, Vol. 25, Issue 8, <http://dx.doi.org/10.1063/1.4818552>.
- [13] Novozhilov B. V. 1973. *Unsteady Combustion of Solid Rocket Propellants* (in Russian), Nauka, Moscow, Translation AFSC FTD-MD-24-317-74.
- [14] Zel'dovich Ya. B., Leipunskii O. I., and Librovich V. B. 1975. *Theory of Unsteady Combustion of Solid Propellants* (in Russian), Nauka, Moscow, USSR.
- [15] Sabdenov K. O. 2007. *Theory of Unsteady Combustion of Solid Rocket Propellants* (in Russian), Tomsk Polytechnic University, Tomsk, Russia.
- [16] Sabdenov K. O. 2013. *Nonstability combustion of solid rocket propellants* (in Russian), Academic Publishing GmbH & Co. KG, Saarbrücken, Germany.
- [17] Sabdenov K. O., Dueck J., and Maira E., "Limits of steady burning propellants in the phenomenological theory using effective initial temperature", *J. of Thermal Science and Technology*, Vol. 10, No. 1, 2015, pp. 1-10.
- [18] Zarko V. E., and Kiskin A. B., "Numerical Modeling of Nonsteady Powder Combustion Under the Action of a Light Flux", *Combustion, Explosion, and Shock Waves*, Vol. 16, Issue 6, 1980, pp. 650-654.
- [19] Zarko V. E., Simonenko V. N., and Kiskin A. B., "Radiation-Driven, Transient Burning: Experimental Results", *Nonsteady Burning and Combustion Stability of Solid Propellants*. De Luca, L., Price, E.W., and Summerfield, M. (Eds.), *Progress in Astronautics and Aeronautics*, Washington: AIAA, Vol. 140, 1987, pp. 363-398.
- [20] Bennett C. O., and Myers J. E. 1962. *Momentum, Heat and Mass Transfer*, Mc Graw-Hill Book Co., New York, London, Toronto.
- [21] Denison M. R., and Baum E. A., "A simplified model of unstable burning in solid propellants", *ARS Journal*, Vol. 31, 1961, pp. 1112-1122.
- [22] Williams F. A. 1964. *Combustion Theory*, Addison-Wesley Publishing Company, Reading, Massachusetts. Palo Alto, London.
- [23] Luigi De Luca., "A critical review of solid rocket propellant transient flame model", *Pure & Appl. Chem.*, Vol. 62, No. 5, 1990, pp. 825-838.
- [24] Gusachenko L. K., and Zarko V. E., "Analysis of unsteady solid-propellant combustion models (review)", *Combustion, Explosion, and Shock Waves*, Vol. 44, Issue 1, 2008, pp. 31-42.
- [25] Gusachenko L. K., and Zarko V. E., "Combustion models for energetic materials with completely gaseous reaction product", *Combustion, Explosion, and Shock Waves*, Vol. 41, Issue 1, 2005, pp. 20-34.
- [26] Beckstead M. W., "Recent progress in modeling solid propellant combustion", *Combustion, Explosion, and Shock Waves*, Vol. 42, Issue 6, 2006, pp. 623-641.
- [27] Merganov A. G., and Duboviskii F. I., "On the theory of steady-state combustion of powder", *Dokl. Akad. Nauk SSSR*, Vol. 129, 1959, pp. 153-156.
- [28] Barrere M., Jaumotte A., De Veubeke B.F., and Van Den Kerckhove. 1960. *Rocket Propulsion*, Elsevier Publishing Company.

- [29] Gusachenko L. K., Miloshevich H., Rychkov A. D., and Shokin Ju. I., "Modeling of the solid-propellant rocket microthruster" (in Russian), *Computing technologies* (in Russian), Vol. 13, No. 1, 2008, pp. 42-47.
- [30] Gusachenko L. K., Rychkov A. D., and Kiskin A. B., "Analysis of the possibility of steady-state operation of a small-size solid-propellant thruster", *Combustion, Explosion, and Shock Waves*, Vol. 45, No. 5, 2009, pp. 579-587.
- [31] Alexander B. Kiskin, Vladimir N. Simonenko, Lev K. Gusachenko, Oleg G. Glotov, and Vladimir Zarko, "Experimental study of microthruster heat loss", *Int. J. of Energetic Materials and Chemical Propulsion*, Vol. 8, No. 4 (2009), pp. 329-344.
- [32] Sabdenov K. O., "Unsteady combustion in terms of the theory dynamics systems", *Khimicheskaya fizika* (in Russian), Vol. 12, No. 3, 1993, pp. 419-424.
- [33] Sabdenov K. O., "On the new approach in theoretical research of non-stationary processes in burning of solid fuel", in book: 1996. *Theory of Combustion of Powder and Explosives*, Nova Science Publication Incorporated, pp. 203-213.
- [34] Nicolis G., and Prigogine I. 1977. *Self-organization in nonequilibrium systems*, John Wiley & Sons, New York.
- [35] Zel'dovich Ya., B., Librovich V. B., Barenblatt G. I., and Makhviladze G. M. 1985. *Mathematical Theory of Combustion and Explosion*, Plenum, New York.
- [36] Gostintsev Yu. A., "Relationship between a phenomenological model of the unsteady-state combustion of a powder and a model of a granular-diffusion flame", *Combustion, Explosion, and Shock Waves*, Vol. 7, No. 6, 1973, pp. 759-764.
- [37] Marxman, G. A., Wooldridge, C. E., and Muzzy, R. J., "Fundamentals of Hybrid Boundary Layer Combustion", *Progress in Astronautics and Aeronautics*, Vol. 15, 1964, pp. 485-521.
- [38] Takakazu Morita, Saburo Yuasa, Koki Kitagawa, Toru Shimada, and Shigeru Yamaguchi, "Low-Frequency Feed-System-Coupled Combustion Instability in Hybrid Rocket Motors", *J. of Thermal Science and Technology*, Vol. 8, No. 2, 2013, pp. 380-394.
- [39] Takakazu Morita, Saburo Yuasa, Shigeru Yamaguchi, and Toru Shimada, "Solid-Fuel Regression Rate for Standard-Flow Hybrid Rocket Motors", *J. of Thermal Science and Technology*, Vol. 7, No. 2, 2012, pp. 387-398.